NON-ERGODIC PROBABILISTIC SEISMIC HAZARD METHODOLOGY USING PHYSICS-BASED GROUND MOTION PREDICTION: THE CASE OF L'AQUILA, ITALY

JEDIDIAH JOEL AGUIRRE[1,2],
BRUNO RUBINO[1], MAURIZIO VASSALLO[3],
GIUSEPPE DI GIULIO[3]
AND FRANCESCO VISINI[4]

[1] *Università Degli Studi Dell'Aquila*
67100 L'Aquila, Italy

[2] *University of the Philippines*
4031 Los Baños, Laguna, Philippines

[3] *Istituto Nazionale di Geofisica e Vulcanologia – Sezione dell'Aquila*
67100 L'Aquila, Italy

[4] *Istituto Nazionale di Geofisica e Vulcanologia – Sezione di Pisa*
56125 Pisa, Italy

(received: 4 January 2020; revised: 9 February 2020;
accepted: 15 March 2020; published online: 1 April 2020)

Abstract: A non-ergodic probabilistic seismic hazard analysis (PSHA) utilizing the physics-based ground motion prediction was proposed in this study to minimize the increasing uncertainties in the use of empirical equations. The City of L'Aquila in Italy was used for illustrative purposes due to the availability of data and the historical seismicity of the site. A total of 28 seismic sources were identified in this study located within a 100 km radius from the city. Fault properties such as geometry and location were obtained from the literature, while the fault occurrence rates were obtained using the FiSH Code. A modified time-weakening friction law was proposed to model the seismic energy released by an earthquake. Uncertainties in different rupture scenarios were characterized through the Guttenberg-Richter Relations and the Characteristic Brownian Time Passage. Uncertainties in distances were characterized through probability mass functions, which were used to calculate the ground motion exceedance probabilities. The 1D elastodynamic equation coupled with the Hooke's law was used to predict the peak ground acceleration (PGA), a measure of the ground shaking level. A hazard curve, which is a plot of PGA and its

recurrence, was constructed and compared with the results of the study of Valentini, *et al.*, *AGU 100: Advancing Earth and Space Science* (2019). The method proposed in this study predicts a higher hazard rates for PGAs less than 0.70 g, which implies that the ground motion was overestimated for very far sources. In contrast, lower hazard curves were observed for PGAs greater than 0.70g which can be attributed to fewer seismic sources considered in this study.

Keywords: non-ergodic probabilistic seismic hazard analysis, physics-based ground motion prediction, modified time-weakening friction law, peak ground acceleration, hazard curve, City of L'Aquila

DOI: https://doi.org/10.34808/tq2020/24.2/a

1. Introduction

Upon the failure of rocks in a causative fault, an earthquake is produced due to the sudden release of energy built on the Earth's crust through seismic waves [1, 2]. As a result, severe earthquakes worldwide have claimed thousands of lives and billions of euros in damages.

On April 6^{th}, 2009 the City of L'Aquila was devastated by an M_w 6.3 earthquake claiming 300 deaths, around 1500 injured, and approximately € 25 billion in damages [3]. The hypocentral depth is about 8.8 to 9 km with a normal style of faulting with a dip of around 43 degrees. The population nearby the epicenter is around 100,000 making the city very seismically vulnerable [3, 4]. This earthquake is deemed to have had the highest death toll and the highest economic loss in the EU. Figure 1 shows the rubbles of some structures in L'Aquila that collapsed during the earthquake in April 2009.

Earthquakes do not kill, but it is the *secondary or seismic hazards* that they trigger [5, 1]. According to Kramer [1], these hazards include ground shaking, structural hazards, liquefaction, landslides, retaining structural failures, lifeline hazards, tsunamis and seiches. For the purpose of discussion, this study will be focused on the ground shaking hazard only, while the other above mentioned seismic hazards will not be covered by it the scope.

The occurrence of earthquakes cannot be fully predicted as to when and where they can occur, but the secondary hazards can be mitigated through proper coordination of seismologists, engineers, social scientists, and policy-making bodies in an area. Hence, there is a need to estimate the underlying *seismic hazard* in terms of ground shaking levels on site required for engineers to be considered in their design and retrofit structures which can collapse during an earthquake.

1.1. Seismic Hazard Analysis

The Seismic Hazard Analysis (SHA) is a method of estimating the feasible ground shaking levels on a site [1]. At the present time, there are two existing ways of estimating ground shaking levels: either deterministic or probabilistic. The *Deterministic Seismic Hazard Analysis* (DSHA) aims to determine exactly the maximum controlling earthquake coming from a certain seismic source that can affect the site on a worst-case scenario basis. On the other hand, the *Probabilistic Seismic Hazard Analysis* (PSHA) is a methodology that estimates the ground

Figure 1. Structural Damage during the Mw 6.3 Abruzzo Earthquake in 2009
Source: https://www.britannica.com/event/LAquila-earthquake-of-2009

shaking hazard in a given place assuming the chances of exceeding a certain level of ground shaking that occurred in the past within a specified period interval of validity.

To further understand these two methods, the outcomes offered by these methods should be considered:

Deterministic

"The peak ground acceleration (PGA) on the site is 0.65g resulting from an earthquake of a magnitude of 6.3 on the Paganica Fault at a distance of 12km from the site"

Probabilistic

"The PGA on the site is 0.45 g with a 10% probability of being exceeded in a 50-year period"

Both these methods use the same information such as past earthquakes, fault geometries, geology, etc. to be discussed later in this paper, however, the PSHA incorporates uncertainties in such data since the occurrence of an earthquake is random by nature. The PSHA can be viewed as a series of deterministic approaches with consideration of uncertainties. The expected output in the PSHA is a *hazard curve*, which describes the hazard level with respect to the ground shaking level on a site [1].

1.1.1. Deterministic Approach

Kramer [1] summarized the DSHA into four steps as shown in Figure 2.

Step 1. In DSHA, all types of seismic sources within a certain distance which can greatly affect a site must be considered. These include point sources (such as

volcanoes), fault lines, or fault planes. These kinds of sources will be discussed in a later part of this paper.

Step 2. The shortest distance from the seismic source to the site, also known as the *source-to-site distance*, is calculated.

Step 3. Using some ground motion prediction equations (GMPE) which relate the distance and magnitude of the earthquake to a ground motion parameter, say the PGA, the existing seismic hazard can be determined "exactly". Hence, the controlling earthquake that will produce the strongest shaking effect will be selected.

Step 4. Lastly, the values of different ground shaking parameters are reported for the site with the corresponding source-to-site distance and magnitude of the earthquake.

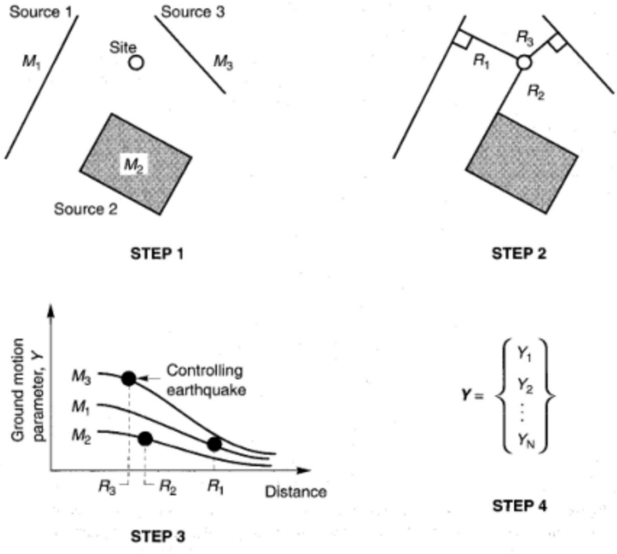

Figure 2. Steps in DSHA
Source: Kramer, 1996 [1]

Based on this framework, the contributor of the overall seismic hazard on a site will be one controlling earthquake only. It is worth noting that other data such as fault geometries, paleoseismology, site properties (the type of soil on the site) are also needed to fully describe the seismic hazard on a site [1, 5].

The problem with the deterministic approach is that the information keeps changing from time to time, hence, it is not proper to say that the seismic hazard is "determined" exactly, but what happens is that the seismic hazard changes from time to time.

1.1.2. Probabilistic Approach

The PSHA will be discussed later in a separate Section. A glimpse of the PSHA is shown here for illustrative purposes and to compare it with the deterministic approach.

Hutchings and Viegas [6] summarized the PSHA dividing it into four steps as shown in Figure 3.

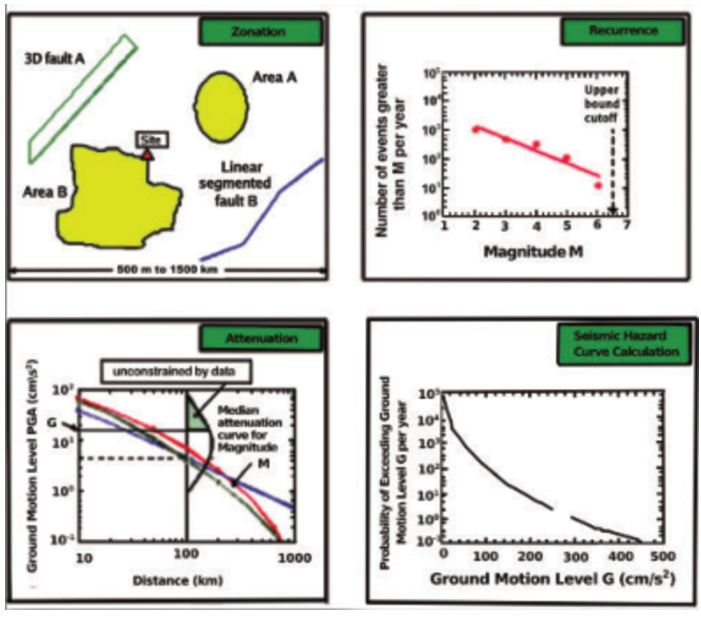

Figure 3. Steps in PSHA
Source: Hutchings and Viegas, 2012 [6]

Step 1 (Zonation). Similarly to the DSHA, all seismic sources that are found at a certain distance which may contribute to the seismic hazard are considered. However, the uncertainties in the source-to-site distances for all seismic sources are formulated through the *probability density functions (PDF).*

Step 2 (Recurrence). Earthquake occurrence in all sources is modeled by a recurrence law. The frequency of earthquakes as a function of the earthquake size (or magnitude) is established, and the recurrence parameters are calculated to be used later in hazard calculations.

Step 3 (Attenuation). GMPEs are used just like in the DSHA, but with consideration given to uncertainties. Due to the development of the PSHA Methodology, the ground motion parameter can be predicted by the existing physical laws on rupture dynamics [7] with uncertainties being taken into account considering a sufficient number of the ground motion predictions [8].

Step 4 (Seismic Hazard Curve Calculation). A hazard rate is calculated in terms of the probability of exceedance or hazard rates, as a function of the ground motion parameter calculated in Step 3.

Based on the probabilistic approach, all kinds of possible earthquake occurrences coming from all possible seismic sources are incorporated into the seismic hazard on a site. As mentioned above, the PSHA is just a series of deterministic approaches with a defined probability of exceedance [9].

The PSHA has a concept of a *return period*, just like strong winds or flooding [10] which is good, as information keeps on changing from time to time. Therefore, it is much better to conduct a PSHA than a DSHA. Many engineers are shifting to the probabilistic approach and tend to abandon the deterministic approach.

1.1.3. Risk Engineering Decisions

The major difference between the two methods is based on what type of decisions the policy-making body must make [9]. Table 1 shows the how McGuire presents the approach to be taken by the engineer and risk mitigation agencies depending on the decision to be made. According to the building code, it is recommended that a structure must withstand a reference peak ground acceleration (PGA) which corresponds to a reference probability of exceedance of 10

Table 1. The predominant approach for several engineering decisions
Source: McGuire, 2001 [9]

DECISION	QUANTITATIVE ASPECTS OF DECISION	PREDOMINANT APPROACH
Seismic design	Highly quantitative	Probabilistic
Retrofit design	Highly quantitative	Probabilistic
Insurance/Reinsurance	Highly quantitative	Probabilistic
Design of redundant industrial systems	Quantitative or Qualitative	Both
Training and plans for emergency purposes	Mostly qualitative	Deterministic
Plans for post-earthquake recovery	Mostly qualitative	Deterministic
Plans for long-term recovery, local	Mostly qualitative	Deterministic
Plans for long-term recovery, regional	Mostly quantitative	Probabilistic

Both methods are applicable for the design of complex structures such as industrial power plants depending on the seismic environment of the site. If the site has many surrounding faults, then, it is desirable to choose the PSHA. If lifelines are to be installed on a site where an active fault is crossed, then the DSHA can be employed instead [9]. This is because the site itself is subjected to the fault

movement and a maximum credible earthquake must be determined to design the lifelines seismically.

Planning for recovery from earthquake losses, whether immediately or in a long term, is a very tedious process where multiple earthquake scenarios cannot be considered, hence, it will be more effective, if only a single scenario earthquake is to be considered for risk mitigation practices and emergency plans. However, for a regional long-term recovery, it is advisable to use the probabilistic approach considering many seismic sources that are present in an entire region, or a country [9].

1.2. Evolution of PSHA Methodology

According to McGuire [11], two different efforts, working independently, ushered a new era of a probabilistic approach whose works combined in 1966. Carl Allin Cornell from the Standford University produced his PhD Dissertation in 1964 entitled *Stochastic Processes in Civil Engineering*, ocused on factors affecting the engineering decisions through probability distributions. Then, Universidad Nacional Autonoma de Mexico (UNAM) conducted several studies on earthquake ground motions and their dependence on the magnitude and distance, and frequencies of ground motions and earthquake occurrences for the engineering design of structures, which were pioneered by the then PhD student Luis Esteva, Prof. Emilio Rosenblueth, and their colleagues.

On 1966, the "probabilistic seismic hazard" was derived from among the relationships of earthquake magnitudes and their respective occurrence rates, earthquake locations, and the resulting ground motions on the site. It was Cornell, who once taught at UNAM, who talked to Esteva and convinced him and his colleagues at UNAM to formalize the concept of the probabilistic approach.

1.2.1. **First Formulation**

Cornell [10] published a paper which became the first PSHA formulation. Assuming a Poisson process of the occurrence of earthquakes, he formulated the probability that zero earthquakes having a minimum Modified Mercalli Intensity (MMI) level would be exceeded for a certain time period considering a minimum magnitude of interest m_0:

$$F_{I_{max}}(i) = \exp\left[-\nu C G \exp\left(\frac{-\beta_i}{c_2}\right)\right], \quad i \geq i' \tag{1}$$

where $F_{I_{max}}$ is the probability of occurrence that an annual maximum intensity I_{max} will occur (usually for $t = 1$ year), ν is the rate of occurrence of a fault, C, G and c_2 are constants related to the ground motion parameters depending on the magnitude of the earthquake and the geometry of the fault, $\beta = b\ln 10$ with b being the Guttenburg-Richter (G-R) slope from the statistical regression of earthquakes, and i' is some lower limit of the MMI Intensity. In his paper, faults can be a point, a line, or a plane. He also pointed out that in the case


Figure 4. Pioneers of the PSHA Methodology. Cornell C. Allin (1938 – 2007), and Esteva Luis (1935 –).
Source: McGuire, 2007 [11]

of many seismic sources, the probability of exceedance was a sum of individual contributions of all faults.

1.2.2. Second Formulation

In 1970, the PSHA was generalized using the concept of the total probability theorem [11]:

$$P(Y>y) \approx \sum_{i=1}^{N} \nu_i \int\int P[Y>y|M,R]\, f(m,r) dm\, dr] \tag{2}$$

where Y and y are ground motion parameters, ν is the occurrence rate of each seismic source i, $P[Y>y|M,R]$ is the conditional probability that Y will exceed a certain value of y given a magnitude M and the *source-to-site* distance R, and $f(m,r)$ is the PDF of magnitude m and distance r. Future research regarding the formulation (2) is the treatment of uncertainties which is not included in (1) which is incorporated in the conditional probability. Usually, this probability takes after normal distribution, which assumes that the ground motion parameter Y is lognormally distributed, and the standard deviation in the Z-transform is composed of aleatory (due to the randomness of the ground motion) and epistemic (due to the lack of data and knowledge) uncertainties [12, 13]. Next, the contribution to the overall seismic hazard is not assessed until the *disaggregation* [14] or *deaggregation* is formulated by McGuire in 1995 [15].

1.2.3. Third Formulation

In 1985, (2) was reformulated by McGuire [15] by introducing uncertainties in the number of standard deviations used in the Ground Motion Prediction Equations (GMPEs):

$$\lambda(Y>y) = \sum_{i=1}^{N} = \nu_i \int\int P[Y>y|M,R,\varepsilon]\, f_M(m) f_R f_\varepsilon(\varepsilon) dm\, dr\, d\varepsilon \tag{3}$$

where $\lambda(Y > y)$ is the hazard rate corresponding to exceedance of the ground motion parameter y, $P[Y > y|M,R,\varepsilon]$ is the Heaviside step function:

$$P[Y > y|M,R,\varepsilon] = H[\ln Y(M,R,\varepsilon) - \ln y] \tag{4}$$

which is zero, if $\ln Y(M,R,\varepsilon)$ is less than $\ln y$ or a given magnitude-distance-standard deviation triple (M,R,ε), and one otherwise; $f_M(m)$ is the PDF of magnitude m, $f_R(r)$ is the PDF of the source-to-site distance, and $f_\varepsilon(\varepsilon)$ is the PDF of the number of standard deviations ε which is normally distributed. The difference in the PDF expressed in (2) assumes in (3) that $f(m,r)$ can be expressed as a product of PDFs of the magnitude and distance, and so the ground motion dependence on magnitude and distance is incorporated into GMPEs which are based on the regression of ground motions over a certain region [1, 14]:

$$\ln y = f(M,R,\theta) + \varepsilon\,\sigma_{\ln y} \tag{5}$$

where θ is the parameter related to the style of faulting or the kinematic of the fault source and/or soil type, and $\sigma_{\ln y}$ is the standard deviation of the natural logarithm of the ground motion parameter y.

1.2.4. **Non-Ergodic PSHA**

In 1999, Anderson and Brune [12] introduced the concept of the *Non-Ergodic PSHA*, which abandons the ergodic assumption of PSHA in the use of GMPEs. The ergodic assumption implies that the ground motion parameters in space are treated in the PSHA as the uncertainty over time at a single point. Regions without a strong ground motion database use GMPEs developed for some other regions, and some engineers tend to abuse them without knowing their applicability in those regions. Hence, uncertainties tend to mount, thus affecting the seismic hazard level. They mentioned that the ergodic assumption tended to overestimate the ground motion parameter Y due to increased uncertainties in the standard deviation in (5) especially for longer return periods of earthquakes.

In their paper, Anderson and Brune [12] have mentioned that the ergodic assumption means that the aleatory uncertainty is present in the PSHA, particularly in the GMPEs. Hence, the objective of their study is to eliminate or minimize the aleatory uncertainties in the analysis, and epistemic uncertainties will remain. The seismic hazard will not be overestimated with the availability of more data and knowledge about the earthquake processes in a certain site.

Landwehr et al. [13] made a non-ergodic GMPE, through a Varying Coefficients Model (VCM) applicable in California. They allowed the coefficients of the GMPE to vary spatially to incorporate effects of source, site, and path variations in the equation. Thus, the epistemic uncertainties are suppressed per site, while the aleatory uncertainty is modeled for the whole of California. As a result, the GMPE produces a reduction of 40% in the aleatory uncertainty which can significantly affect the seismic hazard. Also, it was observed that the epistemic uncertainty was smaller on sites where events or stations were close, and large where there was little data.

Another work on the Non-Ergodic perspective is the study of Kotha, Bindi and Cotton [16] which improved the GMPEs in Europe and in the Middle East towards a Non-Ergodic PSHA. Using the strong ground motion data sets from the Reference Database for the Seismic Ground-Motion in Europe (RESOURCE), they established region-specific for Europe and Middle East, and site-specific GMPEs for Italy and Turkey. The results of their shift from the ergodic to non-ergodic PSHA reveal a change of 25% in the hazard values in region-specific, while larger changes as much as 50% in site-specific GMPEs.

It is shown in these works that the seismic hazard can be lowered significantly with the improvement in the ground motion prediction schemes by minimizing the aleatory uncertainty. Also, if there is an advance in knowledge of faulting and the available data, the epistemic uncertainties can be eliminated [12, 15].

1.2.5. Non-Ergodic PSHA by Physics-Based Ground Motion Prediction

While some researchers such as Landwehr et al. [13] tried to minimize the aleatory uncertainties in the GMPE, others tried to use a physical model rather than a regression model since more data is available to explain the physics behind earthquake occurrences from the failure of rocks in a seismic source. The Southern California Earthquake Center (SCEC) recommended that a physics-based approach of the ground motion prediction was more suitable in minimizing the aleatory uncertainties than using regression-based GMPEs, since the earthquake occurrence was far more complex than what statistics could offer, which was later endorsed by the National Research Council on 2003 in the US, as mentioned by Hutchings and Viegas [6].

The rupture of faults and ground displacements are governed by the Elastodynamic Equation with the proper equations related to material properties of the fault such as the Hooke's Law [17]. Such a model will be thoroughly discussed in Section 2 of this paper.

This approach started when Hutchings et al [18] used the deterministic approach of solving the 3D elastodynamic equation with rupture dynamics using empirical Green Functions, which is a representation function of the ground displacement. Computing all the scenarios for all faults in an area, and with their corresponding earthquake recurrence properties, hazard rates can be assessed in the same way as before as given in (2). In this approach, the probability term is obtained by creating a library of synthetic ground motions by employing uncertainties in fault parameters such as Asperities (strongest fault zone), Rise Time, Rupture Roughness, Rupture Velocity, Healing Velocity, Stress Drop, Hypocenter depth, and Energy released during an earthquake, allowing them to simulate different rupture scenarios for earthquakes.

Hutchings and Viegas [6] suggested a new way of conducting the PSHA, which was also employed in the work of Hutchings et al. [18] in the simulation of the 1999 Athens Earthquake with a moment magnitude of 6.0. Figure 5 illustrates how to perform the Physics-Based PSHA.

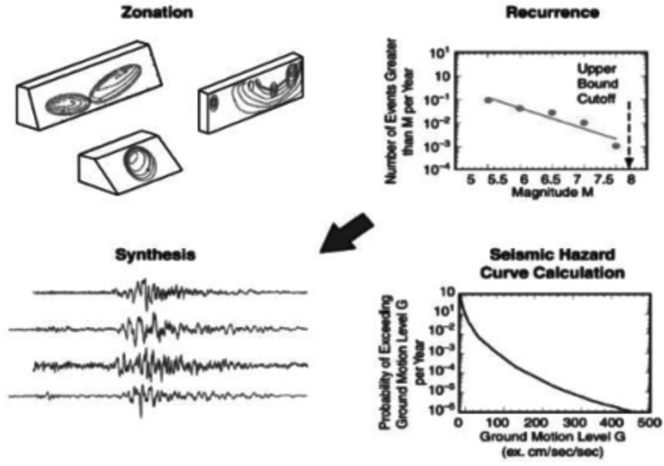

Figure 5. Steps in Physics-Based PSHA
Source: Hutchings and Viegas, 2012 [6]

Step 1 (Zonation). Fault sources are identified for earthquake rupture scenarios. Fault geometries are characterized for simulation of earthquakes. Uncertainties in the distance are not modeled any longer, but the distances are determined for wave propagation purposes.

Step 2 (Recurrence). Just like the conventional PSHA in Figure 3, magnitude occurrences are modeled to determine the recurrence parameters to predict a seismic hazard.

Step 3 (Synthesis). This is the difference with the conventional PSHA where the wave propagation from the fault rupture is simulated to create synthetic seismograms instead of the usual GMPEs. The fault rupture parameters such as fracture energy, stress drop, and rupture velocity to predict the ground motion are calculated.

Step 4 (Seismic Hazard Curve Calculations). This is similar to the conventional PSHA, where the predicted ground motion is paired up with the recurrence parameters that are linked to the magnitude occurrence, allowing the hazard analyst to construct the hazard curve.

Recent approaches by Tarbali et al. [19] and Tarbali et al. [20] make use of the software Cybershake for New Zealand which uses finite-fault rupture models by solving the 3D elastodynamic equation through a finite element method, and computing the hazard rate given by:

$$\lambda_{\mathfrak{I}}(\mathfrak{I}) = \sum_{n=1}^{N_{rup}} P_{\mathfrak{I} \vee Rup}(\mathfrak{I} \vee rup_n)\, \lambda_{Rup}(rup_n) \tag{6}$$

where $\lambda_{Rup}(ru\ p_n)$ is the hazard rate of a certain rupture scenario, and $P_{\mathfrak{I}\vee Rup}(\mathfrak{I}\vee ru\, p_n)$ is the probability of $\mathfrak{I} > \mathfrak{I}$ given $ru\, p_n$. This formulation does not need the uncertainty in the magnitude occurrence, but only the hazard rate obtained from the recurrence of earthquakes, such as the Guttenberg-Richter Law or Characteristic Earthquake models to be discussed in Section 4 of this paper. This formula is based on the probability of exceedance formulations of Field, Jordan, and Cornell [21] which abandons the integration of the seismic hazard rate from (2) with respect to the distance, magnitude, and sometimes the number of standard deviations when using (3).

1.3. Application to L'Aquila, Italy

For engineering applications such as the seismic design and retrofit of structures, it is of utmost importance to know the effects of the earthquake occurrence by estimating the seismic hazard in an area. As mentioned in the review of the seismic hazard zonation of Italy and other European countries in building codes for the seismic design, the reference peak ground acceleration (PGA) must conform to the 10% probability of being exceeded in 50 years of the design life of most structures [22].

According to Monaco et al. [3], the city of L'Aquila sustained a PGA of $0.65\boldsymbol{g}$ both for horizontal and vertical components. Wald et al. [23] formulated a relationship between the Modified Mercalli Intensity (MMI) Scale and PGA, and this PGA of $0.65\boldsymbol{g}$ may bring severe to violent ground shaking to the area which may bring moderate to heavy damage in an area. As shown in Figure 1, L'Aquila was devastated severely by this earthquake in 2009 and the city still has to recuperate from this as the city center is still under reconstruction.

The PSHA can estimate the underlying hazard in an area such as L'Aquila so that future earthquakes can be withstood by the structures to be constructed in the future, and the existing structures can be retrofitted. As per the previous PSHA in Central Italy by Valentini et al. [24], the PGA of L'Aquila corresponding to the 10% and 2% probability of exceedance in 50 years ranges between $0.225\boldsymbol{g}$ to $0.275\boldsymbol{g}$ and $0.60\boldsymbol{g}$ to $0.70\boldsymbol{g}$, respectively. This agrees with the PGA mentioned by Monaco et al. [3], making $0.65\boldsymbol{g}$ having a probability of exceedance of 2% in 50 years, or a return period of 2475 years. Their work is an improvement of another PSHA for the entire Italy of 2017 by Valentini, Visini, and Pace by considering the sequence of earthquakes during the 2016 Central Italy Earthquake the epicenter of which was located at Amatrice.

Hence, for the PSHA in L'Aquila, a non-ergodic assumption was employed for this paper since these two papers made use of the GMPEs from Italy and abroad, thus exhibiting the ergodic assumption. In general, this study aims to develop a PSHA Methodology by employing the non-ergodic assumption by solving the 1D elastodynamic equation to predict the PGA in L'Aquila. Specifically, this study aims to:

1. delineate all the seismic sources within 100 km from L'Aquila from the literature that can significantly contribute to the overall seismic hazard;

2. characterize all the seismic sources identified in this study in terms of their geometry, slip rates, style of faulting, activity rates, and location for earthquake rupture scenarios;
3. calculate distances to determine wave propagation lengths;
4. predict the PGA in all possible magnitude-distance pairs in all seismic sources by solving the 1D elastodynamic equation using staggered-grid finite differences;
5. calculate the hazard rates using the formulation of the seismic hazard (6); and
6. obtain the PGA values with a 10% and 2% probability of being exceeded in 50 years.

The assumptions of this study were as follows:

1. The PGA was assumed to occur at the bedrock level since this ground motion parameter could be modified by the type of soil (i.e. local amplification) which is beyond the scope of this paper;
2. The active fault sources described in these two papers were used extensively in this study by way of exchanging correspondence with Francesco Visini from INGV Pisa, one of the authors of both papers;
3. The active faults considered in this study were those located within a 100 km radius from the city of L'Aquila which could significantly contribute to the overall seismic hazard;
4. Seismic moment rates, mean the recurrence time, and some activity rates were obtained also from Francesco Visini;
5. The fault lines and coordinates were viewed using ArcGIS Pro. Also, the calculation of distances and the division of fault planes into equal areas were performed using ArcGIS Pro;
6. The minimum magnitude of occurrence considered in this study was 5.5 while the maximum was the M_{max} for each fault except for characteristic earthquake models where the minimum and maximum considered were $M_{max}\pm$ one standard deviation;
7. The distributed sources were not considered since the objective of this paper was to demonstrate the use of the Physics-based Ground Motion Prediction as smaller magnitudes were not considered in this study;
8. The Logic Tree Models to account for the epistemic uncertainty were not employed here since the fault parameters were available and GMPEs were not used, which was the advantage of studying L'Aquila as a site of interest;
9. For more conservative results, epicentral distances were obtained instead of hypocentral distances, assuming that the faults were found on the surface and not at a certain depth;
10. The body forces in the 1D elastodynamic equation were not considered;

11. A homogeneous medium was considered for the wave propagation from the source to the site;
12. The point-source approximation was employed as an implication of solving the 1D Elastodynamic Equation since only the PGA was important in the analysis of the ground motion and not the entire response as a function of time and space; and,
13. Hazard calculations were based on Tarbali et al. [19] and Tarbali et al. [20] being rupture-based scenarios, which for this study was the magnitude occurrence in the fault source. The probability of exceedances was computed based on the frequencies of the predicted PGA as a function of the distance given a magnitude of occurrence.

2. Engineering Seismology

In this Section some principles and theories will be discussed to describe the mechanism of the earthquake occurrence. Therefore, the basic notions of seismology relevant to engineering applications will be explained.

2.1. Seismic Waves and Earthquakes

Seismology is the study of earthquakes and movements of seismic waves in Earth's internal structure. When a geologic fault ruptures, an earthquake occurs and elastic strain energy is released through seismic waves which may affect ten to hundreds of kilometers. Seismic waves can be classified into two main types, namely *body waves* and surface waves [1].

Body waves are waves which can travel in the Earth's interior. The two main types of body waves are *p-waves* and *s-waves*. P-waves cause compression and rarefaction in the material along their axis when they pass through it. S-waves cause shearing in the material as they pass through it. While P-waves move parallel to the direction of travel, S-waves move perpendicular to the direction of travel. S-waves can be divided into two component waves, namely SH (pure horizontal motion) and SV (pure vertical motion) waves. Rocks are stiffest in compression, therefore, P-waves travel faster than S-waves, which reach the site faster [1]. The distinction between P-waves and S-waves for illustration is shown in Figure 6

Surface waves are formed when body waves interact with the uppermost layer of the earth. They travel along the surface of the earth, hence the name. There are two types of surface waves, namely *Rayleigh waves* and *Love waves*. Rayleigh waves are created when an SV wave interacts with a P-wave, while Love waves are created when an SH wave interacts with a soft layer of the Earth's surficial layer [1]. Figure 7 shows a comparison between Rayleigh and Love waves.

2.2. Faults

According to the Theory of Plate Tectonics, the surface of the Earth, which is composed of large, dense blocks floating over the viscous mantle which are

constantly moving with respect to each other [1]. This motion of plates causes deformation along boundaries, which produces earthquakes. This movement can be explained by *convection* in the mantle, which imposes shear stresses at the bottom of the plates. Due to these movements, new geologic structures are formed which are called *faults* or *geologic faults* in the form of cracks or discontinuities in the crust.

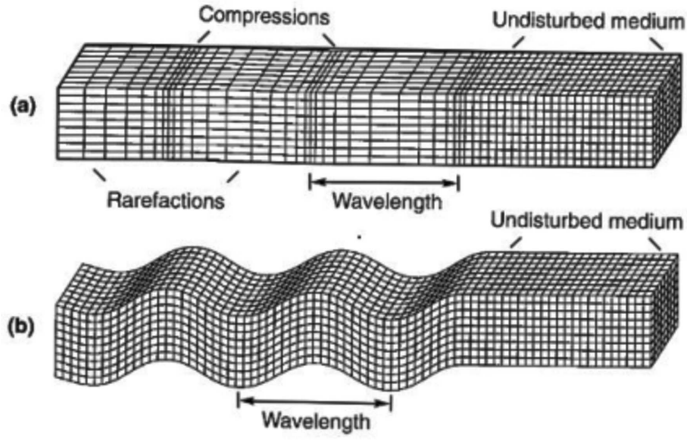

Figure 6. Material deformation caused by (a) P-wave (b) S-wave.
Source: Kramer, 1996 [1]

Faults can have a length ranging from several meters up to hundreds or thousands of kilometers, as in the case of the San Andreas Fault in the US. The presence of faults does not imply that an earthquake will occur in the future. For the purposes of a seismic hazard analysis, a fault must be active, which shows evidence of the fault activity in the late Quaternary or has evidence of the potential to be reactivated in the future [25]. The fault activity is characterized by recent slip displacements or slip rates in the past [1, 25].

2.2.1. Seismic source models

Generally, seismic sources can be modeled as a point, line, plane, or volume [26, 10, 27]. Usually, faults are area sources, which can be modeled as rectangular sources with length (L) along the ground surface or located at a certain depth (d_1) and width (W) which plunges beneath the earth surface. Refer to Figure 8 for visualization of a planar fault (or seismogenic box) as illustrated by Valentini, Visini, and Pace [25]. If a fault is too short in length and is too far from a site, it can be modeled as a point source. If the fault is near but it is short, it can be modeled as a line [1].

2.2.2. Fault Geometry

A fault can be described by the directions of its movement, namely the *strike* and the *dip*. The strike of a fault is the line which forms with the fault plane intersecting the horizontal plane. The azimuth of the strike (S) is the angle

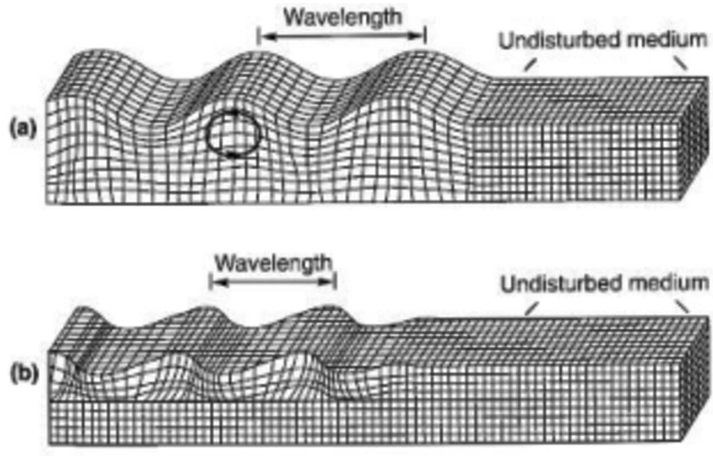

Figure 7. Material deformation caused by (a) Rayleigh wave (b) Love wave.
Source: Kramer, 1996 [1]

of this line relative to the North, usually measured from 0 to 360 degrees. The dip angle (θ) is the angle of the fault plane with the horizontal perpendicular to the strike. The geometric notation of faults is shown in Figure 8 [25] and Figure 9 [1].

Active faults are characterized by their sense of slip, or style of faulting [1]. Faults can be classified into *strike-slip* or *dip-slip faults*. If the dip angle of the fault is 90 degrees, then it is strike-slip. Otherwise, it is dip-slip. Furthermore, dip-slip faults are classified as *normal* or *reverse*. Normal faulting occurs when a hanging wall moves downward relative to the footwall. On the other hand, reverse faulting occurs when the hanging wall moves upward relative to the footwall [1]. In Italy, the majority of faults have this kind of style of faulting [25, 24].

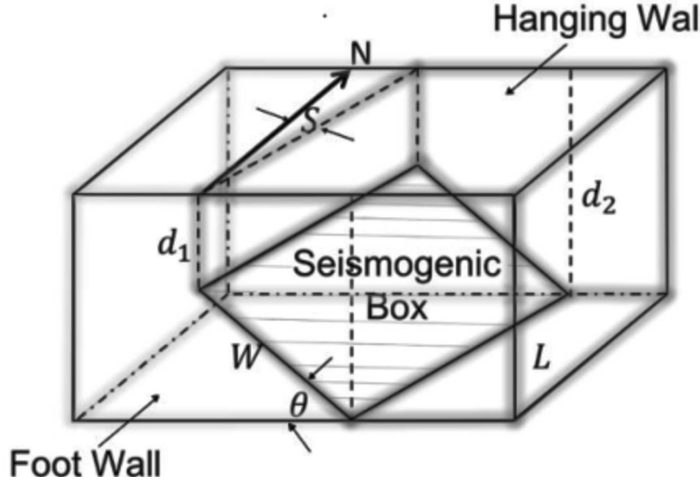

Figure 8. Geometric properties of a fault
Source: Valentini, Visini, and Pace, 2017 [25]

2.2.3. Geometric Notation of Earthquakes

In relation to the faults for which the seismic waves originate, the location of earthquakes is reported in terms of their distances from a seismic monitoring station. Figure 10 shows the different distances of an earthquake that can be described. The *epicentral distance* is the distance of the observer to the point on the ground surface projected above from the source of the tremor, which is called the epicenter. The source of the quake is called the *focus* or the *hypocenter* located along the fault plane. The distance of the observer to the focus is called the *hypocentral distance* [1].

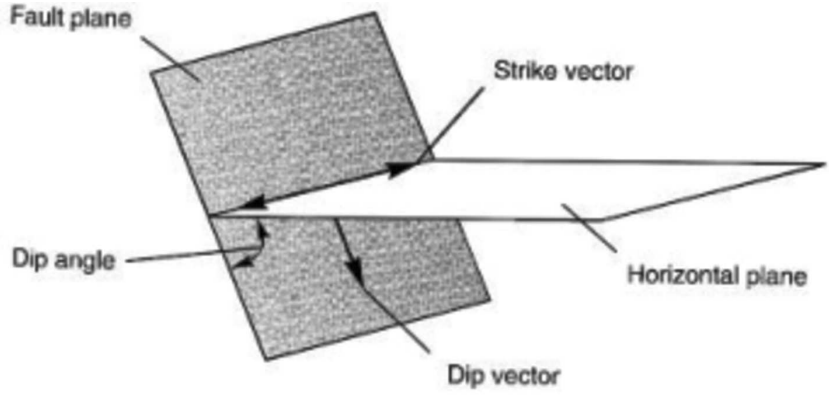

Figure 9. Geometric notation for fault orientation
Source: Kramer, 1996 [1]

2.3. Size of Earthquakes

The size of an earthquake refers to how small or big the impact of an earthquake is. This is important in any SHA as this parameter gives the audience what kind of earthquake to anticipate.

Intensity refers to the qualitative description of the an earthquake which differs from one place to another. This is subjective depending on the extent of the damage an earthquake does at a certain place. The *Modified Mercalli Intensity* (MMI) Scale is used to quantify the damage caused by an earthquake [1]. Cornell [10] pioneered the PSHA using the MMI Scale as the earthquake size, but changes have been made as intensity is qualitative only.

Magnitude is the size of an earthquake based on the amount of energy it has released. There are four main types of magnitude scales used: local (Richter), body-wave, surface-wave, and moment magnitude [1, 2, 28]. The first three scales mentioned above are obsolete nowadays for advanced countries, but these scales are still used, especially for developing countries. This is because these magnitude scales exhibit the *saturation effect* [28, 2, 1], or the inability of the scale to measure magnitudes beyond a certain value.

Nowadays, the moment magnitude scale is used to represent the size of an earthquake, especially in conducting a PSHA. This scale is based on the *seismic moment* of an earthquake when a geologic fault ruptures [29, 30]. The seismic moment M_0 (in dyne-cm) is given by:

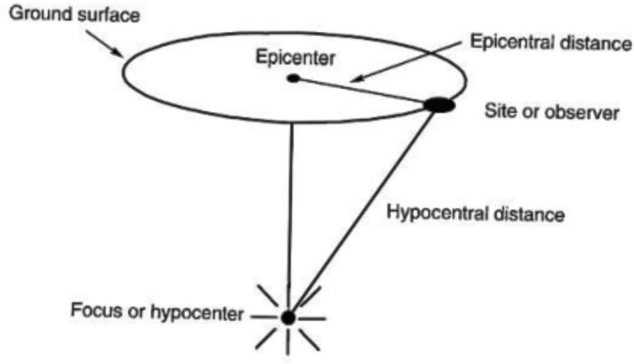

Figure 10. Geometric Notation of Earthquakes
Source: Kramer, 1996 [1]

$$M_0 = \mu AD \tag{7}$$

where μ is the shear modulus of rigidity of the rock equal to $3.3 \times 10^{10} \mathrm{N/m^2}$, A is the ruptured area of the fault (in square meters) and D is the average slip rate in the long run (in cm/yr). One may refer to Figure 8 to calculate the rupture area of the fault given the dip angle and the seismogenic thickness (or depth) of the fault. The moment magnitude M_w of an earthquake is given by [30]:

$$M_w = \frac{2}{3} \log M_0 - 10.7 \tag{8}$$

If the seismic moment is expressed in Newton-meters (N-m), the moment magnitude is given by [29].

$$M_w = \frac{2}{3} (\log M_0 - 9.1) \tag{9}$$

Since the moment magnitude scale is based on the seismic moment, it is a very good measurement of the size of an earthquake [1, 28, 2]. Therefore, the moment magnitude scale is typically the magnitude scale used in conducting a PSHA.

Other relations are correlated by Causse, Dalguer, and Mai [31] to relate the seismic moment (in N-m) to the dynamic stress drop ($\triangle\sigma_d$) and the fracture energy (G) during earthquakes are given by:

$$\begin{aligned} \log \triangle\sigma_d &= 0.21 \log M_0 - 3.0 \\ \log G &= 0.60 \log M_0 - 10.6 \end{aligned} \tag{10}$$

The stress drop is the decrease in shear stresses in rocks after a fault ruptures, while the fracture energy is the energy required to initiate fracture in rocks [32].

Given these relationships between the seismic moment, the moment magnitude, the dynamic stress drop and the fracture energy, an earthquake for the seismic hazard analysis can be simulated.

2.4. Elastic Rebound Theory

As plates move toward each other, elastic strain energy builds up along the edges of the two plates in motion. This energy continues to build up until such time that the shear strength of rocks is exceeded, and thus rupture occurs (and subsequently, the earthquake occurs) and the energy is released. The nature of failure of rocks depends on the type of material of the rock. If the rock is brittle and strong, it is expected to have a sudden release of energy which can be transformed into some heat and some shear waves. If the rock is ductile and weak, only small energy is released and therefore faults move slowly and will not cause a massive earthquake [1]. This process of building up the elastic strain energy and releasing the energy to the rock next to the fault is called the *Elastic Rebound Theory*. Figure 11 shows the two possible failure modes of rocks along the fault line.

Not all earthquakes reported by a seismic monitoring station result from a sudden release of strain energy in rocks. These earthquakes can be classified as *foreshocks, main shocks*, or *aftershocks*. The elastic rebound theory can explain the difference between these three shocks. The energy stored and the strength distributed along the fault are not the same, meaning that certain portions of rocks are relatively weaker. In cases where a weaker portion ruptures, a foreshock will occur. These kinds of earthquakes will occur until the strongest part of the fault, also known as *asperity*, ruptures, and this will trigger the occurrence of the main shock. Then, after some time, some remaining stronger portions of the fault will have their shear strengths exceeded upon a continuous movement of the crust, and this will trigger the occurrence of aftershocks [1].

As mentioned by Kramer [1], the elastic rebound theory states that the occurrence of earthquakes will de-stress the fault until new elastic energy builds up again. This implies that all the earthquakes attributed to a ruptured fault are not random and dependent on each other. The knowledge of this concept is very important in the PSHA particularly in modeling the occurrence of earthquakes.

2.5. Seismograms

The ground motion on a certain site during an earthquake excitation is measured by instruments called *seismographs* or *accelerographs* and the recordings are plotted on *seismograms* or *accelerograms*, or which shows the variation of displacement, velocity, or acceleration as a function of time [1]. Figure 12 shows an example of a typical seismogram.

Seismograms are used in creating *response spectra* by taking the Fourier Transform of the displacement, velocity, or acceleration to produce a plot of maximum response values of ground motion parameters (displacement, velocity, or acceleration) of structures and soils as a function of *natural period*, a property

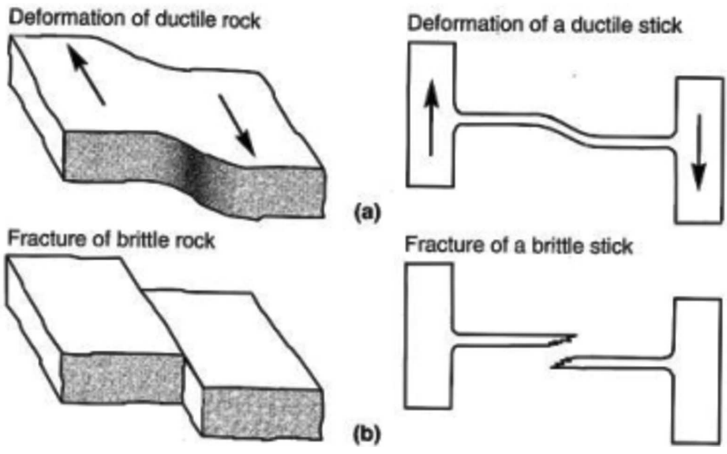

Figure 11. Failure modes of rocks along the fault: (a) ductile (b) brittle
Source: Kramer, 1996 [1]

of a structure or soil which is the time that it takes for the structure or soil to complete an oscillation [1]. This is a very important application of seismograms for engineering purposes.

Seismograms are also used to characterize an earthquake in terms of its peak ground acceleration (PGA), peak ground velocity (PGV), or peak ground displacement (PGD). As mentioned before, PGA is important for building code applications [22, 1].

For seismic hazard applications, a seismogram can be created synthetically by performing a numerical simulation of the earthquake mechanism if the style of faulting, the magnitude, and the rock properties are known [18, 6, 33].

2.6. Ground Motion Prediction Equations

It is indeed a vital part for any seismic hazard analysis to model the behavior of seismic waves as they travel from one place to another. Predictive relations that relate the ground motion to the magnitude, distance and other parameters are called *Ground Motion Prediction Equations (GMPE)* or *Attenuation Relationships* [2, 10, 14, 1, 27]. Usually, a GMPE takes the form of the expression shown in (5).

2.6.1. Statistical Approach

According to Kramer [1], the function must reflect the mechanics of the ground motion as exactly as possible, hence, the available strong ground motion data in the form of time histories is used to correlate the ground motion parameters and the magnitude and distance of the occurrence, considering the soil type and the style of faulting. Usually, GMPEs are expressed in terms of the natural logarithm of the ground motion parameter since the logarithms of the ground motion parameter are normally distributed, as shown in (5). Equation (11) elaborates the expressions of a GMPE used in the study of Landwehr, et al. [13]:

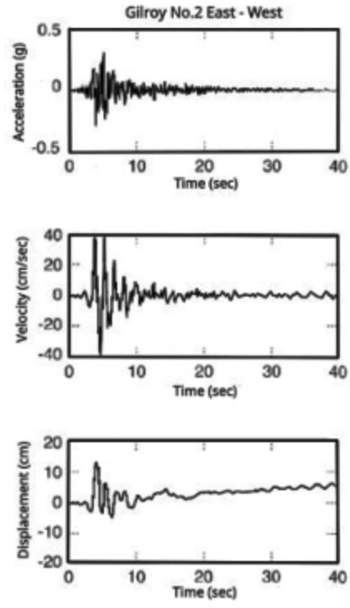

Figure 12. An accelerogram obtained from Gilroy Site, with velocity and displacement time histories integrated using the Trapezoidal Rule.
Source: Kramer, 1996 [1]

$$y = \beta_0 + \beta_1 M + \beta_2 M^2 + (\beta_3 + \beta_4 M) \ln \sqrt{R_{JB}^2 + h^2} + \\ + \beta_5 R_{JB} + \beta_6 \ln V_{S30} + \beta_7 F_R + \beta_8 F_{NM} + \epsilon \tag{11}$$

where $y = y(M, R_{JB}, V_{S30}, F)$ is the ground motion parameter of interest, β_i are the coefficients to be determined, M is the magnitude, R_{JB} is the nearest distance from the source to the site projected vertically upward, V_{S30} is the shear wave velocity in the uppermost 30 m height of soil on the site, F takes account of the style of faulting (reverse or normal fault), h is a constant and ϵ s a residual term. These coefficients are to be determined given a strong ground motion data set.

Since the equation is a result of regression, an error term also known as the *uncertainty* in the ground motion parameter is always present, usually expressed as a standard deviation of the natural logarithm of the ground motion parameter. This uncertainty makes the use of GMPEs to be an ergodic approach, which assumes that data measurements that are spatially varying are the same as sampling as a function of time at a single point in space [12]. For a PSHA to have fewer uncertainties, the new focus of studies is currently a non-ergodic assumption which deals with improvement of GMPEs.

According to Anderson and Brune [12] and Landwehr et al. [13], this uncertainty in the GMPEs can be broken down into two main components: the aleatory uncertainty (or variability), which represents the randomness in the ground motion and is inherent to the ground motion; and the epistemic

uncertainty, which accounts for the lack of knowledge in the process of the earthquake occurrence and the lack of data.

Landwehr et al. [13] tried to minimize the aleatory variability in their studies by considering the repeatability of measurements to account for the epistemic uncertainties in the path, source, and site of interest, making these uncertainties distributed into multiple points across California. These resulted in a decrease in the aleatory variability by 40% and a decrease in the epistemic uncertainty in areas with more data, but an increase in areas with scarce data.

Kotha, Bindi, and Cotton [16] shifted their PSHA from an ergodic assumption to a regional and site specific PSHA, minimizing the overall hazard as much as 25% in a regional PSHA and as high as 50% change in a site specific environment.

2.6.2. **Physics-Based Approach**

The problem in the ergodic assumption in the PSHA is the treatment of both the aleatory and epistemic uncertainties. Using this approach, a correlation between the ground motion and the specific source, path is lost which results in building the uncertainties [18, 6]. In this regard, there is a need for more data regarding historical earthquakes to be more certain of an earthquake process. Thus, employing an actual physical model with physical parameters of the fault can be used to characterize the actual ground motion itself, while keeping the original characteristics of the seismic source that produced that earthquake. The aim of the physics-based approach is to produce a library of ground motions which are site-specific and source-specific, which is also done in a normal DSHA or PSHA by classifying the site and seismic sources for the GMPE to be utilized. In this way, too much uncertainty in the ground motion can be avoided to be incorporated into the seismic hazard. Incorporating this deterministic approach into a probabilistic framework not only justifies using a model of an actual earthquake, but it also gives meaning to the inherent randomness of an actual process.

The wave propagation from a seismic source is governed by the *Elastodynamic Equation* which is given by [17]:

$$\rho \ddot{u}_i = f_i + \tau_{ij,j} \tag{12}$$

where ρ (assumed constant) is the volumetric mass density of the deforming body, $\boldsymbol{u} = (u_1, u_2, u_3) \in \mathbb{R}^3$ is the displacement vector, $\boldsymbol{f} = (f_1, f_2, f_3) \in \mathbb{R}^3$ is the body force vector, and $\tau_{ij,j} \in \mathbb{R}^3$ is the Cauchy Stress tensor, with j subscript indicating a spatial derivative with respect to coordinate j, and the dot represents the time derivative. The result of solving the elastodynamic equation is a synthetic seismogram, which can be used to predict the ground motion [34, 17, 33].

Equation (11) is a partial differential equation in time and space, which requires another relationship from the properties of the material to solve it, provided that the initial and boundary conditions are satisfied. This equation will be derived in the next Section.

2.7. Derivation of Elastodynamic Equation

The derivation from Aki and Richards [17] will be discussed here. There are two ways to fully express kinematics and kinetics in a continuum. The *Lagrangian coordinates* are used to study a particle of interest with the known starting position at a given time frame, and the *Eulerian coordinates* are used to study any particle moving along in any time and space. For seismology applications, it is better to describe the motion of particles in Lagrangian coordinates since seismograms are site-specific and are studied at a given location and time.

In this paper, the Cartesian Coordinate system will be used, and the tensors are also Cartesian. Let $\boldsymbol{u}=\boldsymbol{u}(\boldsymbol{x},t)$ be the displacement as a function of position $\boldsymbol{x}\in\mathbb{R}^3$ and time $t\in[0,T]$, where T is the duration of an earthquake. Let this position be taken at a certain reference time $t=0$. Denote the *particle velocity* as $\dot{\boldsymbol{u}}=\partial\boldsymbol{u}/\partial t$ and the *particle acceleration* as $\ddot{\boldsymbol{u}}=\partial^2\boldsymbol{u}/\partial^2 t$. Hence, the regularity required for $\boldsymbol{u}$ is C^2 in time. It must be assumed also for now that $\boldsymbol{u}$ is C^1 in space.

If a particle with initial position x traveled to a point with new position $\boldsymbol{x}+\boldsymbol{u}$, then $\boldsymbol{u}\equiv\boldsymbol{u}(\boldsymbol{x})$ is the displacement field. Let $\delta\mathbf{x}$ be a deformation introduced on a portion of a medium the position of which is $\boldsymbol{x}$ such that the particle position is initially at $\boldsymbol{x}+\delta\boldsymbol{x}$. Then, the new position of the particle becomes $\boldsymbol{x}+\delta\boldsymbol{x}+\boldsymbol{u}(\boldsymbol{x}+\delta\boldsymbol{x})$. Any deformation is responsible for changing the relative position of the endpoints of line-element $\delta\boldsymbol{x}$. If the change is $\delta\boldsymbol{u}$, then the new vector line-element corresponds to $\delta\boldsymbol{x}+\delta\boldsymbol{u}$ which is equivalent to:

$$\delta\boldsymbol{x}+\delta\boldsymbol{u}=\boldsymbol{x}+\delta\boldsymbol{x}+\boldsymbol{u}(\boldsymbol{x}+\delta\boldsymbol{x})-(\boldsymbol{x}+\boldsymbol{u}(\boldsymbol{x})) \tag{13}$$

For $|\delta\mathbf{x}|$ very small $\mathbf{u}(\mathbf{x}+\delta\mathbf{x})$ can be approximated by the first order Taylor Series expansion as

$$\boldsymbol{u}(\boldsymbol{x}+\delta\boldsymbol{x})\approx\boldsymbol{u}(\boldsymbol{x})+(\delta\boldsymbol{x}\cdot\nabla)\,\boldsymbol{u}(\boldsymbol{x})+O\left(|\delta\boldsymbol{x}|^2\right) \tag{14}$$

By inspection, it follows that

$$\delta\boldsymbol{u}=(\delta\boldsymbol{x}\cdot\nabla)\,\boldsymbol{u}\qquad\text{or}\qquad\delta u_i=\frac{\partial u_i}{\partial x_i}\delta x_j \tag{15}$$

First, let the spatial derivative be denoted by $u_{i,j}=\partial u_i/\partial x_i$ and let the Kronecker symbol $\delta_{i,j}$ and the alternating tensor with components ε_{ijk} be denoted as:

$$\delta_{ij}=\begin{cases}1 & if\quad i=j\\ 0 & if\quad i\neq j\end{cases}\qquad\varepsilon_{ijk}=\begin{cases}1 & if\quad (i,j,k)=(1,2,3),(2,3,1),(3,1,2)\\ 0 & if\quad i=j=k\\ -1 & otherwise\end{cases} \tag{16}$$

Also, the important properties of these notations are

$$a_i=\delta_{ij}a_j\qquad\text{and}\qquad\varepsilon_{ijk}a_jb_k=(\boldsymbol{a}\times\boldsymbol{b})_i \tag{17}$$

and these are also associated with the following properties:

$$\varepsilon_{ijk}\varepsilon_{ilm} = \delta_{jl}\delta_{km} - \delta_{jm}\delta_{kl} \qquad \text{and} \qquad \varepsilon_{ijk}\varepsilon_{lmn} = \begin{vmatrix} \delta_{il} & \delta_{jl} & \delta_{kl} \\ \delta_{im} & \delta_{jm} & \delta_{km} \\ \delta_{in} & \delta_{jn} & \delta_{kn} \end{vmatrix} \tag{18}$$

Since a part of the motion is caused only by an infinitesimal rigid-body rotation about $\boldsymbol{x}$, it is not a prerequisite to solve for all the nine independent components of the tensor $u_{i,j}$. Using the properties from (16)- (18) and the identity $(u_{i,j} - u_{j,i})\delta x_j = \varepsilon_{ijk}\varepsilon_{jlm}u_{m,l}\delta x_k$, (15) can be rewritten as

$$\delta u_i = \frac{1}{2}\left(u_{i,j} + u_{j,i}\right)\delta x_j + \frac{1}{2}\left(\text{curl } \boldsymbol{u} \times \delta\mathbf{x}\right)_i \tag{19}$$

with the rigid-body rotation equal to curl $\boldsymbol{u}$, and the last term of (19) can be viewed as rigid-body rotation if and only if $|u_{i,j}| \ll 1$. Then, define the strain tensor with the components

$$e_{ij} = \frac{1}{2}\left(u_{i,j} + u_{j,i}\right) \tag{20}$$

the effect of true deformation on any line-element δx_j, making the change to the relative position to its endpoints by $e_{ij}\delta x_j$. Since the rigid-body motion does not impose deformation, hence, the new length is given by:

$$\begin{aligned} |\delta\boldsymbol{x} + \delta\boldsymbol{u}| &\approx \sqrt{\delta\boldsymbol{x}\cdot\delta\boldsymbol{x} + 2\delta\boldsymbol{u}\cdot\delta\boldsymbol{x}} && \text{(neglecting } \ \delta\boldsymbol{u}\cdot\delta\boldsymbol{u}) \\ &= \sqrt{\delta x_i \cdot \delta x_i + 2e_{ij}\delta x_i \delta x_j} && \text{(using (19) and since (curl } \boldsymbol{u}\times\delta\boldsymbol{x})\cdot\delta\mathbf{x} = 0) \\ &\approx |\delta\boldsymbol{x}|\left(1 + e_{ij}\gamma_i\gamma_j\right) && \text{(binomial approx. to first order, if } |e_{ij}| \ll 1) \end{aligned}$$

where $\boldsymbol{\gamma}$ is the unit vector $\delta\boldsymbol{x}/|\delta\boldsymbol{x}|$. Hence, the extension imposed by deformation $\delta\boldsymbol{u}$ is directed towards $\boldsymbol{\gamma}$ is equal to $e_{ij}\gamma_i\gamma_j$. This result will be used later for the material property to solve (12).

Now, the internal forces acting on the particles of the continuum must be identified, and for that purpose the concepts of *traction* and *stress tensor* will be used. These forces are called surface or *contact forces*. Traction is the vector of force per unit area acting on an internal surface S with normal $\boldsymbol{n} \in \mathbb{R}^3$ on the continuum as shown in Figure 13a. This force denoted by $\delta\boldsymbol{F} \in \mathbb{R}^3$ can act as an angle with respect to $\boldsymbol{n}$, such that these two vectors are not parallel. This is possible for solids, for which shear stresses can act. For a given point on S, traction $\boldsymbol{T} \in \mathbb{R}^3$ is defined as the infinitesimal force $\delta\boldsymbol{F}$ acts along the infinitesimal surface δS, and taking the limit $\delta\boldsymbol{F}/\delta S$ as $\delta S \to 0$. This traction acts as if the material is being pulled to the normal points, and so the traction is $\boldsymbol{T} = \boldsymbol{T}(\boldsymbol{n})$.

Next, the forces existing among the particles and other forces resulting from some physical phenomenon outside the medium must be taken into account. These are called body forces such as gravitational and magnetic forces, which can be denoted by $\boldsymbol{f}(\boldsymbol{x}, \boldsymbol{t}) \in \mathbb{R}^3$ to indicate the body forces per unit volume at an initial

position $\boldsymbol{x}$ and a certain initial time frame. Usually, it is preferable to have body forces to be applied impulsively (or a very large force applied at a very short time) to a specific particle $\boldsymbol{x}=\boldsymbol{\xi}$ and $t=t_0$. This force, component-wise, is proportional to the Dirac Delta Function $\delta(\boldsymbol{x}-\boldsymbol{\xi})$ in space, the Dirac Delta Function $\delta(t-t_0)$ in time, and the Kronecker Delta function $\delta(t-t_0)$, which indicates directionality that $f_i=0$ fot $i\neq n$. Then, combining these assumptions, the body force is given by:

$$f_i(\boldsymbol{x},t)=A\delta(\boldsymbol{x}-\boldsymbol{\xi})\delta(t-t_0)\delta_{in} \tag{21}$$

where $A\in\mathbb{R}$ is the strength of the impulse. To analyze the dimension, f_i, $\delta(\boldsymbol{x}-\boldsymbol{\xi})$, and $\delta(t-t_0)$ have the dimensions of force per unit volume, 1/unit volume and 1/unit time, hence, A has a dimension of force x time which is the same for an impulse.

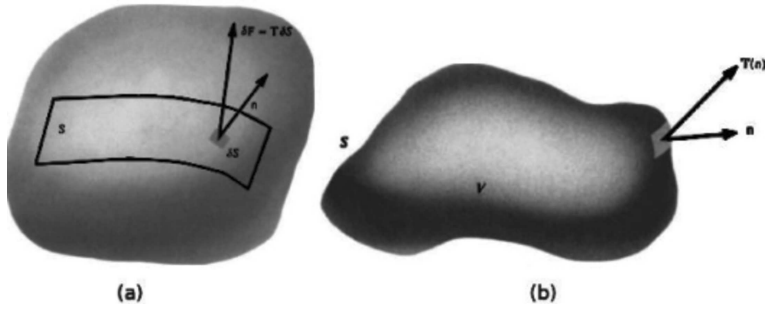

Figure 13. (a) Traction acting on internal surface S
(b) volume material V of the continuum with surface S
Source: Aki and Richards, 2002 [17]

Consider volume V of the material with surface S in Figure 13b. By Newton's Second Law of Motion, the change in momentum in the entire volume V is the sum of the body forces and the traction. Mathematically, this is given by:

$$\frac{\partial}{\partial t}\int\limits_V \rho\frac{\partial \boldsymbol{u}}{\partial t}dV=\int\limits_V \boldsymbol{f}dV+\int\limits_S \boldsymbol{T}(\boldsymbol{n})dS \tag{22}$$

with V and S moving along with the particles. Since V does not depend on time, the time derivative can be put inside the integral making (22) equivalent to:

$$\int\limits_V \rho\frac{\partial^2 \boldsymbol{u}}{\partial t^2}dV=\int\limits_V \boldsymbol{f}dV+\int\limits_S \boldsymbol{T}(\boldsymbol{n})dS \tag{23}$$

Now, consider a small tetrahedron (as shown in Figure 14) with three of its faces lying along the coordinate axes with outward normals $\hat{x}_j$ $(j=1,2,3)$, while the fourth face has a normal $\boldsymbol{n}$. To arrive at (11) the first step is to find a good expression for the traction. To accomplish this, consider a particle P within the medium located in the origin with distance $\epsilon\to 0$ from the corners of the tetrahedron. Also, assume that $\partial^2\boldsymbol{u}/\partial t^2$, $\boldsymbol{f}$, $\boldsymbol{T}$ are C^1 functions. Then, it follows

that $|V| \sim \epsilon^3$ and $|S| = |\partial V| \sim \epsilon^2$. The expressions in the volume integrals can be bounded by their maximum values as shown:

$$\int_V \rho \frac{\partial^2 \boldsymbol{u}}{\partial t^2} dV \leq \rho \left| \frac{\partial^2 \boldsymbol{u}}{\partial t^2} \right| |V| \qquad \int_V \boldsymbol{f} dV \leq |\boldsymbol{f}||V| \tag{24}$$

It can be observed from (23) that all the terms have the same units of forces, with the traction terms composed of the traction multiplied by the area. Combining the terms in (24) in the left-hand side and dividing everything with the measure of S, one can obtain:

$$\frac{|V|}{|S|} \left[\rho \left| \frac{\partial^2 \boldsymbol{u}}{\partial t^2} \right| - |\boldsymbol{f}| \right] = \frac{\left| \int_S \boldsymbol{T} dS \right|}{|S|} \tag{25}$$

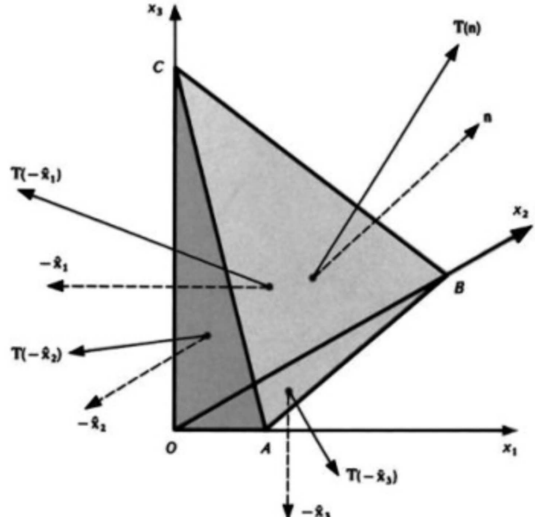

Figure 14. Infinitesimal tetrahedron given the faces and their respective normal outward vectors.
Source: Aki and Richards, 2002 [17]

Since $|V|$ has the measure ϵ^3 and $|S|$ has the measure ϵ^2, it follows that $|V|/|S| \sim \epsilon \to 0$ and thus, the left-hand side of (25) approaches zero, forcing the right-hand side also to approach zero as $\epsilon \to 0$ and thus one obtains:

$$\frac{\left| \int_S \boldsymbol{T} dS \right|}{|S|} \to 0 \tag{26}$$

The second step is to consider that V is an infinitesimal cylinder with height ϵ and radius ϵ, whose bases are centered at $\boldsymbol{x}$, as shown in Figure 15. It is desirable to

show that $\boldsymbol{T}(-\boldsymbol{n}) = -\boldsymbol{T}(\boldsymbol{n})$. Then, the integral term in (22) involving the traction for the cylinder in Figure 15 is given by:

$$\int_S \boldsymbol{T} dS = \int_{B_1} \boldsymbol{T}(\boldsymbol{n}(\mathbf{x}))\, dS + \int_{B_2} \boldsymbol{T}(-\boldsymbol{n}(\boldsymbol{x}))\, dS + \int_{B_3} \boldsymbol{T}\left(\boldsymbol{n}_{B_3}(\boldsymbol{x})\right) dS \tag{27}$$

By the mean value theorem for integrals, for some $\boldsymbol{x}_{B1}, \boldsymbol{x}_{B2}, \boldsymbol{x}_{B3} \in V$ and $\boldsymbol{T}(\boldsymbol{n})$ continuous on V, one has:

$$\int_S \boldsymbol{T} dS = |B_1| \left| \boldsymbol{T}\left(\boldsymbol{n}(\boldsymbol{x}_{B_1})\right) \right| + |B_2| \left| \boldsymbol{T}\left(-\boldsymbol{n}(\boldsymbol{x}_{B_2})\right) \right| + |B_3| \left| \boldsymbol{T}\left(\boldsymbol{n}(\boldsymbol{x}_{B_3})\right) \right| \tag{28}$$

It follows from the cylinder in Figure 15 that $|V| = \pi\epsilon^4$ and $|\mathrm{S}| = 2^3 + 2\pi\epsilon^2 \approx 2\pi\epsilon^2$ and due to (26), dividing (28) by $|S|$ yields:

$$\frac{1}{|S|} \int_S \boldsymbol{T} dS = \frac{|B_1|}{|S|} \left| \boldsymbol{T}\left(\boldsymbol{n}(\boldsymbol{x}_{B_1})\right) \right| + \frac{|B_2|}{|S|} \left| \boldsymbol{T}\left(-\boldsymbol{n}(\boldsymbol{x}_{B_2})\right) \right| + \frac{|B_3|}{|S|} \left| \boldsymbol{T}\left(\boldsymbol{n}(\boldsymbol{x}_{B_3})\right) \right| \tag{29}$$

and setting $\epsilon \to 0$, $\boldsymbol{x}_{B_1}, \boldsymbol{x}_{B_2}, \boldsymbol{x}_{B_3} \to \boldsymbol{x}$ and the cylinder will be squeezed to $\boldsymbol{x}_{B_1}, \boldsymbol{x}_{B_2}, \boldsymbol{x}_{B_3}$ which results in:

$$0 = \frac{1}{2} \boldsymbol{T}(\boldsymbol{n}(\boldsymbol{x})) + \frac{1}{2} \boldsymbol{T}(-\boldsymbol{n}(\boldsymbol{x})) \tag{30}$$

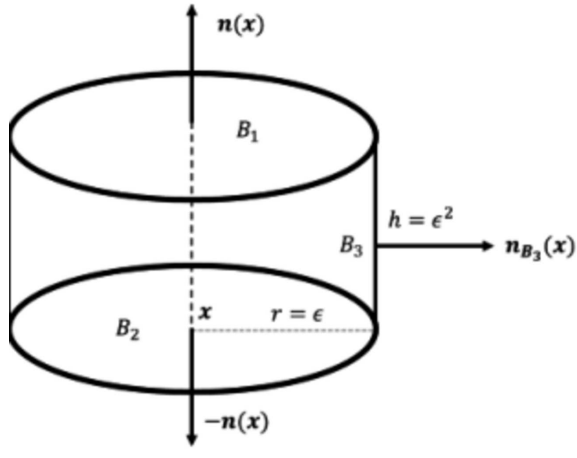

Figure 15. An infinitesimal cylinder centered at $\mathbf{x}$ with normal $\boldsymbol{n}(\boldsymbol{x})$ and $-\boldsymbol{n}(\boldsymbol{x})$ along surfaces B_1 and B_2, normal $\boldsymbol{n}_{B_3}(\boldsymbol{x})$ along surface B_3.

with the third term becomes $\epsilon\, \boldsymbol{T}\left(\boldsymbol{n}_{B_3}(\boldsymbol{x})\right) \to 0$ as $\epsilon \to 0$. And thus, it is shown that:

$$\boldsymbol{T}(-\boldsymbol{n}) = -\boldsymbol{T}(\boldsymbol{n}) \tag{31}$$

The third step is to go back to Figure 14. As a consequence of (26), it is implied that:

$$\frac{\boldsymbol{T}(\boldsymbol{n})|ABC| + \boldsymbol{T}(-\hat{\boldsymbol{x}}_1)|OBC| + \boldsymbol{T}(-\hat{\boldsymbol{x}}_2)|OCA| + \boldsymbol{T}(-\hat{\boldsymbol{x}}_1)|OAB|}{|ABC| + |OBC| + |OCA| + |OAB|} \to 0 \tag{32}$$

as $\epsilon \to 0$. Moreover, one can show that the components of the normal vector $\boldsymbol{n}$ are given by $(n_1, n_2, n_3) = (|OBC|, |OCA|, |OAB|)/|ABC|$. To show this, the Gauss Divergence theorem can be used. Assuming that for $n_i > 0$, we have:

$$0 = \int_V div\ \hat{\boldsymbol{x}}_{\boldsymbol{j}} dV = \int_{ABC} \hat{\boldsymbol{x}}_{\boldsymbol{j}} \cdot \boldsymbol{n}\, dS - \sum_{i=1}^{3} \int_{B_1} \hat{\boldsymbol{x}}_{\boldsymbol{i}} \cdot \hat{\boldsymbol{x}}_{\boldsymbol{j}}\, dS = n_j |ABC| - |B_i|$$

where B_i are areas $(|OBC|, |OCA|, |OAB|)$. Hence, from (32) and (31), one can obtain

$$\mathbf{T}(\mathbf{n}) = \mathbf{T}(\hat{\mathbf{x}_\mathbf{j}})\, n_j \tag{33}$$

Defining the stress tensor with components $\tau_{kl} = T_l(\hat{x}_k)$ so that τ_{kl} is the lth component of the contact stress acting on the plane normal to the kth axis with the above material acting upon another material below. Hence, using this definition one has:

$$T_i = \tau_{ji} n_j \tag{34}$$

Using Figure 14 and the result from (34), the equation of motion of a general particle can be studied. Using the Gauss Divergence Theorem, (34) yields,

$$\int_S T_i dS = \int_S \tau_{ji} n_j dS = \int_V \tau_{ji,j} dV \tag{35}$$

and the volume of the material can be generalized such that from (23), one has

$$\int_V \left(\rho \frac{\partial^2 u_i}{\partial t^2} - f_i - \tau_{ji,i} \right) dV = 0 \qquad \blacksquare \tag{36}$$

which is our desired result. The integral in (36) is zero for any choice of volume V with the assumption that the acceleration, body forces, traction are continuous functions on V.

For simplicity in solving, only one-dimensional elastodynamic equation was considered in this study since the fault models used in this study are simple fault models and the PSHA employed in this study considers the classical approach of obtaining distances of discretized seismic sources, which is similar to using GMPEs that require a single distance. Hence, (12) can be simplified for a 1D case and is given by

$$\rho \frac{\partial^2 u}{\partial t^2} = f + \frac{\partial \tau}{\partial x} \tag{37}$$

According to Shearer [32], the body force does not dominate in regions of the earth that are far away from the source, and for the purpose of solving (37), the body force was not considered in this study and the homogenous equation was used:

$$\rho \frac{\partial^2 u}{\partial t^2} = \frac{\partial \tau}{\partial x} \tag{38}$$

It can be noticed that there are two variables of interest here: the displacement and the traction. This equation alone cannot be solved even if there are enough

boundary conditions, hence, a *constitutive* relation coming from the property of the medium must be used to solve (37). This property of material involves the relationship between the stress and the strain in a perfectly elastic medium, which is called the *Hooke's Law*[1], and is given for one-dimensional case by:

$$\tau = \mu e_{ii} = \frac{\mu}{2}\left(u_{i,i} + u_{i,i}\right) = \mu \frac{\partial u}{\partial x} \tag{39}$$

where e_{ii} is the strain tensor for one dimension from (20) and μ s a Lamè constant also known as the shear modulus of rigidity. To avoid expressions of a second-order term in (37), the velocity response can be used instead by introducing $\nu = \partial u/\partial t$ and taking the time derivative in (38), which yields into a system of two PDEs given by:

$$\begin{cases} \rho \frac{\partial \nu}{\partial t} = \frac{\partial \tau}{\partial x} \\ \\ \frac{\partial \tau}{\partial t} = \mu \frac{\partial \nu}{\partial x} \end{cases} \tag{40}$$

and this system of PDEs form a second-order linear PDE which will be discussed further in the next Section.

3. Wave Equation

In this Section, the elastodynamic equation will be treated mathematically by studying partial differential equations, the well-posedness of the problem, and numerical solution of the elastodynamic equation.

3.1. Partial Differential Equations

A partial differential equation (PDE) is a type of equation involving an unknown function of two or more variables [35]. In this Section, all concepts regarding PDEs will be focused on one-dimension only.

3.1.1. **Preliminaries**

Definition 1. The PDE that can be expressed as

$$F\Big(D^k(\boldsymbol{x}), D^{k-1}u(\boldsymbol{x}), ..., D\,u(\boldsymbol{x}), u(\boldsymbol{x}), \boldsymbol{x}\Big) = 0 \qquad (\boldsymbol{x} \in V) \tag{41}$$

is called a k-*th* order PDE, where $F: \mathbb{R}^{n^k} \times \mathbb{R}^{n^{k-1}} \times ... \mathbb{R}^n \times \mathbb{R} \times V \to \mathbb{R}$ is given, while the function $u: V \to \mathbb{R}$ is the unknown variable and U is a vector space with x a vector of some dimension d.

1. For 3-D, Hooke's Law is expressed as $\tau_{ij} = c_{ijpq} e_{pq}$ with c_{ijpq} is a fourth-degree tensor with symmetries $c_{ijpq} = c_{ijpq}$ and $c_{ijpq} = c_{ijpq}$ due to $\tau_{ij} = \tau_{ij}$ and $e_{pq} = e_{pq}$ respectively. See Aki and Richards [17]

The notation $D^k u$ means that the function is differentiated k times with respect to two or more variables, depending on the dimension of U . In the usual partial derivative notation,

$$D^k u = \frac{\partial^k u}{\partial x_1^{\alpha_1} \partial x_2^{\alpha_2} ... \partial x_d^{\alpha_d}} = u_{\underbrace{x_1 x_1 ... x_1}_{\alpha_1 \text{times}} \underbrace{x_2 ... x_2}_{\alpha_2 \text{times}} ... x_d ... x_d}$$

where $\sum_i \alpha_i = k$ and x_i are components of $\boldsymbol{x} = (x_1, ..., x_d)$.
The PDE (41) is solved if all the possible functions are obtained and found to satisfy (41) given a number of additional boundary conditions along the boundary ∂V. The solution means a simple, straightforward expression that satisfies (41), or showing the existence of solutions and their properties.

Definition 2. The PDE in (41) is said to be of a linear type if it can be expressed as

$$\sum_{|\alpha| \le k} a_\alpha(x) D^\alpha u = f(x)$$

for given functions $a_\alpha (|\alpha| \le k)$, f. Also, this PDE is said to be homogeneous if $f \equiv 0$. The PDE in (41) is said to be of a *semi-linear* type, the principal part only, the one with the highest order, is linear, and the other expressions of partial derivatives of lower order are nonlinear. The PDE is *quasilinear* if the function multiplied to the principal part is nonlinear, but the highest derivative term remains linear. If none of these three classify as a PDE, then it is *nonlinear*.

Definition 3. The PDE in the form of

$$\boldsymbol{F}\Big(D^k \boldsymbol{u}(\boldsymbol{x}), D^{k-1} \boldsymbol{u}(\boldsymbol{x}), ..., D\, \boldsymbol{u}(\boldsymbol{x}), \boldsymbol{u}(\boldsymbol{x}), \boldsymbol{x}\Big) = 0 \qquad (\boldsymbol{x} \in U) \tag{42}$$

is called a *k-th order system of PDEs*, where $\boldsymbol{F}: \mathbb{R}^{n^k} \times \mathbb{R}^{n^{k-1}} \times ... \mathbb{R}^n \times \mathbb{R} \times U \to \mathbb{R}^m$ given and $\boldsymbol{u}: U \to \mathbb{R}^m, \boldsymbol{u} = (u_1, ..., u_m)$ are unknowns.
The number of unknowns here is m, hence, there are m number of scalar PDEs. In cases of more unknowns than the number of equations, a set of several relations are required to solve the PDEs which are called *constitutive laws* [36].

Definition 4. A problem with a PDE model is said to be *locally well-posed* if the PDE satisfies the following [35–37]:

I The existence of a solution.

II The uniqueness of the solution.

III The solution depends continuously on the given data.

If a problem is said to satisfy Definition 4, then the problem has a solution which is very good for modeling applications such as the Ground Motion Prediction. If the problem does not satisfy all these three conditions, then the problem is called *ill-posed* and this calls for remodeling it.

There are two types of data that ensures the uniqueness of the solution of (41) or (42), and these are *initial conditions* and *boundary conditions* [36]. The

initial conditions are data usually needed for time-dependent problems which gives the value of the unknown function and/or derivative values at an initial time, say $t=0$, and is given by:

$$\nu(x,0)=g(x) \qquad \dot{\nu}(x,0)=h(x)$$

On the other hand, the boundary conditions are data that is available regarding the functional values and/or derivative values at some points along the boundary of the domain, usually at the endpoints of a line domain of length L_p, or corners of a plane, etc.

Definition 5. Given a PDE either in (41) or (42). The boundary condition is said to be of the *Dirichlet type*, if the functional values along the boundary are given in the problem, such as

$$\nu(0,t)=f_1(t) \qquad \nu\left(L_p,t\right)=f_2(t)$$

The boundary condition is said to be of the *Neumann* type, if the values of the derivative of the unknown function along the boundary are given, such as

$$\nu_x(0,t)=f_1(t) \qquad \nu_x\left(L_p,t\right)=f_2(t)$$

It is possible for the two types of boundary conditions to be used depending on the type of the data present, this is a *mixed type*, and is given by

$$\nu(0,t)=f_1(t) \qquad \nu_x\left(L_p,t\right)=f_2(t)$$

There is another type of a boundary condition called the *Robin* condition, but it is never used for an elastodynamic equation. For time-dependent problems, it is required for the PDE to have initial and boundary conditions to be classified as a well-posed. This kind of a problem is called an *initial-boundary value problem* [37].

3.1.2. **Second Order Partial Differential Equations**

The discussion of this Subsection is obtained from Zachmanoglou and Thoe [37] for the classification of second order PDEs. Let $x,y\in V$, where $V\subset \mathbb{R}$ is open. The unknown function is $u: V\times V\to \mathbb{R}$. The general form of linear second order, one-dimensional PDE in two independent variables is given by:

$$au_{xx}+2bu_{xy}+cu_{yy}+du_x+eu_y+fu+g=0 \tag{43}$$

where a,b,c,d,e,f and g are functions of both x and y. For the purpose of considering the Elastodynamic Equation with the Hooke's Law, let the functions a,b, and c be constants (or can be of class C^2 in general). It is desirable to discuss (43) in the domain $V\subset \mathbb{R}^2$ the *discriminant*

$$\Delta=b^2-ac \tag{44}$$

to classify (43) according to its sign in V. The principal part of (43) are those terms involving the second derivatives, and we wish to simplify these terms by introducing a new set of coordinates ξ and η, both are functions of $x,y\in V$. Given the initial data (x_0,y_0), there is a neighborhood $U\subset V$ of (x_0,y_0) for which (44)

can be transformed using new coordinates, and this equation is called a *canonical form* in U. Let ξ and η be expressed as the following:

$$\xi = \xi(x,y) \qquad \eta = \eta(x,y) \tag{45}$$

Let these functions be of class C^2 and have smooth non-singular transformations, and the Jacobian is not zero,

$$J \equiv \frac{\partial(\xi,\eta)}{\partial(x,y)} \equiv \xi_x\eta_y - \xi_y\eta_x \neq 0 \tag{46}$$

In a neighborhood of any point (x_0,y_0), in V where (46) is satisfied, x and t can also be expressed as functions of ξ and η (inverse):

$$x = x(\xi,\eta) \qquad y = y(\xi,\eta) \tag{47}$$

Using the chain rule, one can obtain

$$u_x = u_\xi\xi_x + u_\eta\eta_x \qquad u_y = u_\xi\xi_y + u_\eta\eta_y \tag{48}$$

and

$$\begin{aligned} u_{xx} &= u_{\xi\xi}\xi_x^2 + 2u_{\xi\eta}\xi_x\eta_x + u_{\eta\eta}\eta_x^2 + \ldots \\ u_{xx} &= u_{\xi\xi}\xi_x\xi_y + u_{\xi\eta}\xi_x\eta_y + u_{\xi\eta}\xi_y\eta_x + u_{\eta\eta}\eta_x\eta_y + \ldots \\ u_{yy} &= u_{\xi\xi}\xi_y^2 + 2u_{\xi\eta}\xi_y\eta_y + u_{\eta\eta}\eta_y^2 + \ldots \end{aligned} \tag{49}$$

Lower derivatives from (43) are expressed in the ellipses in (49) since only expressions of the principal parts matter for this discussion. Substituting (47) – (49) to (43) yields:

$$Au_{\xi\xi} + Bu_{\xi\eta} + Cu_{\eta\eta} + \ldots = 0 \tag{50}$$

where

$$\begin{aligned} A &= a\xi_x^2 + 2b\xi_x\eta_x + c\eta_x^2 + \ldots \\ B &= a\xi_x\xi_y + b\xi_x\eta_y + b\xi_y\eta_x + c\eta_x\eta_y + \ldots \\ C &= a\xi_y^2 + 2b\xi_y\eta_y + c\eta_y^2 + \ldots \end{aligned} \tag{51}$$

It can be observed that forming the expression

$$B^2 - AC = \left(b^2 - ac\right)\left(\xi_x\eta_y - \xi_y\eta_x\right)^2 \tag{52}$$

where $\Delta' = \Delta J^2$ is the modified discriminant in the variables ξ and η. If this transformation of coordinates is smooth and non-singular, then the sign of the discriminant in (44) does not change. Hence, a theorem is proven as a consequence of this.

Theorem 1. Under a smooth nonsingular transformation of coordinates, the sign of the discriminant (44) in the PDE in (43) with two independent variables does not change.

Hence, the discriminant of (43) is an inherent property which is independent of any coordinate system to be used. The value of this discriminant can be positive, zero, or negative, which renders three types of a second order linear PDE.

Definition 6. Let from (44) be the discriminant for (43). Then, if:

a $\Delta > 0$ at at the point (x_0, y_0), then (43) is a *hyperbolic* PDE at (x_0, y_0)

b $\Delta = 0$ at at the point (x_0, y_0), then (43) is a *parabolic* PDE at (x_0, y_0)

c $\Delta < 0$ at at the point (x_0, y_0), then (43) is a *elliptic* PDE at (x_0, y_0)

3.2. Elastodynamic Equation with Hooke's Law

Now, in light of the discussion in Subsection 3.1, the system of linear PDEs which is given by (40) from Section 2:

$$\begin{cases} \rho \frac{\partial \nu}{\partial t} = \frac{\partial \tau}{\partial x} \\ \\ \frac{\partial \tau}{\partial t} = \mu \frac{\partial \nu}{\partial x} \end{cases} \tag{40}$$

will be discussed here in this Subsection. It is worth noting that the density ρ and the shear modulus μ are assumed to be constants, $x \in \left[0, L_p\right], t \in [0, T]$, and both $|\nu| \leq \nu_{max}$, $\tau \leq \tau_{max}$ are bounded, with L_p being the length of the wave propagation, or the distance of the source to the site, and T being the duration of the seismogram. By adding the time derivative in the first equation to the space derivative in the second equation from (39), one can obtain

$$\frac{\partial^2 \nu}{\partial t^2} = \beta^2 \frac{\partial^2 \nu}{\partial x^2} \tag{53}$$

which is a homogenous, linear second order PDE also known as the *elastic wave* equation with $\beta = \sqrt{\mu/\rho}$ also known as the S-wave velocity [17, 32]. This is also the propagation speed of an S-wave across the material of the earth, which causes the shearing action. Since this is only in one-dimension, this only involves the SH component of an S-wave which is enough for the purpose of finding the PGA on a given site.

To show that (40) is hyperbolic, the value of the discriminant can be obtained with $A = 1$, $B = 0$ and $C = -\beta^2$ using (44):

$$\Delta = 0^2 - (1)\left(-\beta^2\right) = \beta^2 > 0$$

Wave equations in the form of $u_{tt} - c^2 u_{xx} = 0$ are hyperbolic equations which can be used as models for describing the vibration of a string (in 1D), a membrane (in 2D), or an elastic solid (in 3D) [35, 36], and acoustic waves on a pipe [37, 32]. Another way to show that (40)is hyperbolic is by writing it in a compact form:

$$\boldsymbol{w}_t + \boldsymbol{A}(x,t)\boldsymbol{w}_x = \boldsymbol{0} \tag{54}$$

where

$$\boldsymbol{w} = \begin{pmatrix} v \\ \tau \end{pmatrix} \qquad \boldsymbol{A} = \begin{pmatrix} 0 & -1/\rho \\ -\mu & 0 \end{pmatrix}$$

Definition 7 [36, 37]. If matrix $\boldsymbol{A}$ in the system in (54) has real and distinct eigenvalues, then(54) is said to be a hyperbolic system in a domain, say $\left(0, L_p\right) \times (0, T)$ for this problem.

The characteristic equation of matrix $\boldsymbol{A}$ is $\lambda^2 - \mu/\rho = 0$ with roots $\lambda = \pm\sqrt{\mu/\rho} = \pm\beta$ which are the eigenvalues that are real and distinct. Hence, (40) is of a

hyperbolic type. According to Li and Chen [38], (54) is well-posed given the appropriate initial and boundary conditions, if matrix $\boldsymbol{A}$ has real eigenvalues and each eigenvalue has a corresponding eigenvector.

3.2.1. **Initial and Boundary Conditions**

Since (39) was used in predicting the ground motion, the initial and boundary conditions on velocity and stress were required to solve the problem. The following data is assumed for velocity:

$$\nu(0,t)=0 \qquad \nu(x,)=0 \tag{55}$$

which is appropriate since the velocity at $x=L_p$ is required which represents the seismogram needed for the ground motion prediction. The interpretation of zero velocity at the boundary means that the boundary is rigid, but the stress in not zero. On the other hand, it is assumed that initially, the fault is at rest and so the system is in equilibrium [33].

For the initial condition, the traction must be zero since the rocks outside the fault are in equilibrium at time $t=0$ [33]. For the boundary condition, the *time-weakening friction law* [7] was adapted which assumes that in a point source, the stress variation is due to the stress drop during an earthquake and is governed by the friction in the fault. For this study, this friction model was modified considering the time to permit the propagation of cracks during rupture. The resulting boundary condition is given by

$$\tau(0,t)=\begin{cases} \frac{1}{2}(\tau_0+\tau_1)+\frac{t}{2t_r}(\tau_0-\tau_1), & 0\le t_r\le t \\ \left[\tau_0-(\tau_0-\tau_1)\frac{t-t_r}{t_1}\right], & t_r<t\le t_1 \\ \tau_1, & t>t_1 \end{cases} \tag{56}$$

where τ_0 and τ_1 are the static and dynamic stresses in the fault, t_r is the rupture time (or the rise time) which is the total time of propagation of cracks in the fault zone of length L approximately equal to $0.5L/\nu_r$ for bilateral rupture [39] and $\nu_r=0.9\beta$ is the rupture velocity which is an assumed value [32], t_1 is the time that it takes to decrease the shear stress from τ_0 to τ_1. The value of t_r can be viewed also as the time it takes for the stress to rise from a certain value of stress, say $1/2(\tau_0+\tau_1)$ to τ_0, which assumes that the point source is stressed initially before the fault moves and releases the energy during the earthquake. This model assumes that under no earthquake occurrences, the shear stress acting in the fault is the dynamic shear stress. The profile of stress at all values of time $t\ge 0$ is shown in Figure 16.

According to Bizzarri [7], the shaded area in Figure 16 is the fracture energy G while the change from static stress to dynamic stress is what is referred to as the stress drop $\Delta\sigma$ [32], which can be estimated by the formulation obtained from (10) by Causse, Dalguer, and Mai [31]. To apply the modified friction law for this study, τ_1 is assumed to be zero which implies that the fault will be completely relieved of

the shear stress upon the release of seismic waves. Therefore, the modified friction law for the boundary condition at the source implies that upon rupture of the fault, there is an increase in stress at that point from $\tau_0/2$ to $\tau_0 = \Delta\sigma_d$ (stress drop) with duration of t_r, then decreasing the linearly from τ_0 to zero, and no residual stresses will be left in the fault.

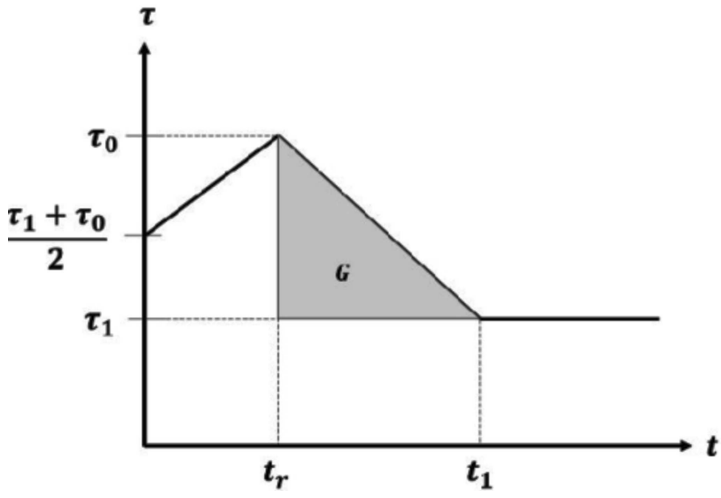

Figure 16. Modified time-weakening friction law

3.3. Numerical Solution to Partial Differential Equations

There are many ways to solve PDEs and each of them has its own pros and cons. Analytical (explicit) solutions can be obtained by representation formulas, transform methods, or separation of variables. Numerical solutions can be utilized such as the finite difference method, the finite element method, or meshless methods, which offer approximations to the exact solutions depending on the complexity of the PDE for which viable exact solutions cannot be obtained. is is only the finite difference method will be discussed in this paper, while other types of finding a solution are not within the scope of this study.

3.3.1. Finite Difference Approximations to Elastodynamic Equation and Hooke's Law

In the finite difference method, the function and its derivatives are approximated using the Taylor expansion. The Taylor expansion for $\nu(x+h)$ for a small increment h is given by:

$$\nu(x+h) = \nu(x) + h\,\nu'(x) + \frac{h^2}{2}\nu''(x) + \frac{h^3}{6}\nu'''(x) + O(h^3) \tag{57}$$

Similarly, $\nu(x+h)$ is obtained in the same fashion:

$$\nu(x-h) = \nu(x) - h\,\nu'(x) + \frac{h^2}{2}\nu''(x) - \frac{h^3}{6}\nu'''(x) + O(h^3) \tag{58}$$

Using (58) and (59), the derivates of the function can be approximated. For the elastodynamic equation and the Hooke's Law, it is the first derivatives only that appear, and hence, these are the only derivatives considered in this study. The first derivative can be expressed using *forward differencing, backward differencing*, and *central differencing*. Using forward differencing, the first derivative of $\nu(x)$ can be approximated as:

$$\nu^{'}(x) = \frac{\nu(x+h)-\nu(x)}{2h} + O(h) \tag{59}$$

with a very small step size h. Using backward differencing, the expression for the derivative is given by:

$$\nu^{'}(x) = \frac{\nu(x)-\nu(x-h)}{2h} + O(h) \tag{60}$$

Using the central differencing, the derivative can be approximated as:

$$\nu^{'}(x) = \frac{\nu(x+h)-\nu(x-h)}{2h} + O(h^2) \tag{61}$$

which has a double step size. While the first two expressions of the first derivative are first-order accurate, the last one is a second-order accurate. Virieux [33] used central differencing to approximate the spatial derivative, with the same step size, but on a staggered-grid, which results in a more accurate approximation up to four times smaller than a normal grid. Figure 17 shows how stress and velocity grids are formulated by Virieux [33]. Using the approach used by Virieux, the first derivative is given by:

$$\nu^{'}(x) = \frac{\nu(x+h/2)-\nu(x-h/2)}{h} + O(h^2) \tag{62}$$

For simplicity in differencing in space, $\nu(x+h)$ is denoted by ν_{j+1}, while $\nu(x-h)$ is denoted by ν_{j-1}; for differencing in time, $\nu(t+k)$ is denoted by ν^{i+1} while $\nu(t-k)$ is denoted by ν^{i-1}.

Now, let the problem involving the ground motion prediction be recalled and given by (63):

$$\begin{cases} \rho\frac{\partial \nu}{\partial t} - \frac{\partial \tau}{\partial x} = 0 & \\ & (x,t) \in \left[0, L_p\right] \times [0,T] \\ \frac{\partial \tau}{\partial t} - \mu\frac{\partial \nu}{\partial x} = 0 & \\ \nu(x,0) = 0 \qquad \tau(x,0) = 0 & x \in \left[0, L_p\right] \\ \nu(0,t) = 0 \qquad \tau(0,t) = f(t) & t \in [0,T] \end{cases} \tag{63}$$

where $f(t)$ is given by (56).

Let the grid spacing Δx be chosen arbitrarily and let it be set equal to L_p/J, where J is the number of grid points, and the time step Δt be any very small number for a moment (this will be discussed later in Subsection 3.3.2). Let the

interior of the computation domain $\left[\boldsymbol{0}, \boldsymbol{L_p}\right] \times [\boldsymbol{0}, \boldsymbol{T}] \in \left(\boldsymbol{x_j}, \boldsymbol{t^i}\right)$ be discretized in the following manner:

$$\begin{aligned} x_j &= x_{j-1} + j\Delta x \qquad 1 \le j \le J \\ t^i &= t^{i-1} + i\Delta t \qquad 1 \le i \le 1 \end{aligned} \tag{64}$$

Using (61) and (62), (63) can be approximated as [33, 40, 32]:

$$\begin{cases} \nu_j^{i+1/2} = \nu_j^{i-1/2} + \frac{\Delta t}{\Delta x} \frac{\tau_{j+1/2}^i - \tau_{j-1/2}^i}{\rho} & 1 \le i \le I,\ 1 \le j \le J \\ \tau_{j+1/2}^{i+1} = \tau_{j+1/2}^i + \mu \frac{\Delta t}{\Delta x} \left[\nu_{j+1}^{i+1/2} - \nu_j^{i+1/2}\right] & (x,t) \in \left(0, L_p\right) \in (0,T) \end{cases} \tag{65}$$

where the subscripts indicate differencing in space and the superscripts indicate differencing in time. In this approach, velocities and stresses are stored in different points, with a step offset of half in space and time. It is implicit to the numerical scheme in (65) that the initial conditions required for this problem are obtained at $t = -\Delta t/2$ and at $t = \Delta t/2$. Similarly, the boundary conditions are obtained at $x = -\Delta x/2, \Delta x/2$. The central differencing in time is similar with (61), while that in space is shown in (62), hence, the staggered grid approach. The velocity and the pressure are still obtained from the same grid points, but the values required from the approximation are half-steps to the left and to the right, and up and down of the grid point, just like a five-point stencil. As mentioned by Shearer [32], the error in the approximation is four time smaller since the sampling is halved. For the pressure at the boundary, it is assumed that it is the same in the vicinity of the fault rupture point within the half of the grid spacing to the left and right, and zero outside the vicinity of the point.

3.3.2. Consistency, Stability, and Convergence of Finite Difference Approximations

For the purpose of discussion of the properties of the numerical scheme in (65), some definitions from Li and Chen [38] were used here to ensure a unique solution for given initial and boundary data.

Definition 8. The *truncation errors* of the scheme in (65) are defined as

$$TE_1(x,t) = \frac{\nu(x,t+\Delta t/2) - \nu(x,t-\Delta t/2)}{\Delta t} - \frac{1}{\rho} \frac{\tau(x+\Delta x/2,t) - \tau(x-\Delta x/2,t)}{\Delta x}$$

$$TE_2(x,t) = \frac{\tau(x,y+\Delta t/2) - \tau(x,t-\Delta t/2,)}{\Delta t} - \mu \frac{\nu(x+\Delta x/2,t) - \nu(x-\Delta x/2,t)}{\Delta x} \tag{66}$$

Definition 9. The scheme in (65) is said to be consistent with the differential equations in (40), if the truncation errors in (66) approach zero as $\Delta x,\ \Delta t \to 0$ for any $(x,t) \in \left(\Delta x/2, L_p\right) \times (\Delta t/2, T)$.

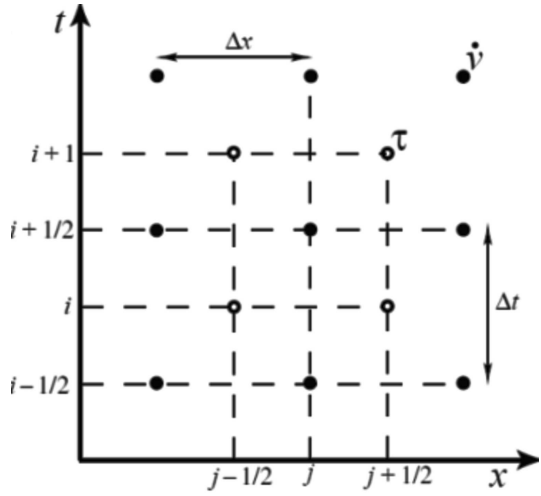

Figure 17. A staggered grid in which velocities and stresses are stored at different points. *Source: Shearer, 2009 [32]*

Definition 10. The scheme in (65) is said to be *stable* under the norm $||\cdot||$ for a time-dependent PDE if there exists a constant M such that

$$\left||u^i|\right| \leq M\left||u_i^0|\right| \qquad \forall i \;\; \Delta t, \leq T \tag{67}$$

where M is independent of $\Delta x, \Delta t$ and the initial condition u^0.

Definition 11. Let the exact and numerical solutions to (40) and (65) be denoted by $U_{PDE}(x,t)$ and $u_{FD}(x_j,t^i)$. The scheme in (67) is said to convergent if

$$|u_{PDE} - u_{FD}| \to 0 \qquad \Delta x, \Delta t \to 0 \tag{68}$$

Theorem 2 (Lax-Richtmyer). For the scheme formulated in (65) to be a well-posed linear time-dependent problem, (65) must be both consistent and stable for the convergence of the solution.

Clearly, using the above definition, (65) is consistent with (40) as Δx, $\Delta t \to 0$, for any $(x,t) \in \left(0, L_p\right) \in (0,T)$. To prove that (65) is stable, the von Neumann Stability analysis will be invoked, which is used for the linear constant coefficient problem [38]. If the formulation in (65) is both consistent and stable, then Theorem 2 can be invoked to claim that (40) has a unique solution numerically which depends on the given initial and boundary data.

To use the von Neumann Stability Analysis [40], the solution to (65) is assumed to be in the form of exponential functions just like what is done in separation of variables, and then obtaining a Fourier Series for the superposition of solutions. Assume that ν and τ in the form

$$\begin{aligned} \nu_j^n &= A \exp(-i\omega n\, \Delta t + ikj\, \Delta x) \\ \tau_j^n &= B \exp(-i\omega n\, \Delta t + ikj\, \Delta x) \end{aligned} \tag{69}$$

where ν_j^n, τ_j^n are velocity and traction at $x = x_j$ and $t = t^n$ (to avoid confusion with the use of index i and imaginary unit $i = \sqrt{-1}$, n is used for showing stability), A, B are constants (or amplitude of the wave), ω, k are the wave numbers of the solution. Substituting (68) to the velocity and traction terms in the right-hand sides of the equations, one obtains:

$$\begin{aligned}
\nu_{j+1}^{n+1/2} - \nu_j^{n+1/2} &= \\
&= \mathrm{A}\exp\left(-i\omega(n+1/2)\Delta t + ik(j+1)\Delta x\right) - A\exp\left(-i\omega(n+1/2)\Delta t + ikj\Delta x\right) \\
&= \mathrm{A}\exp\left(-i\omega(n+1/2)(\Delta t) + ikj\,\Delta x/2\right)\left[\exp\left(ik\,\Delta x/2\right) - \exp\left(-ik\Delta x/2\right)\right] \\
&= \nu_{j+1/2}^{n+1/2}\left[2\,i\sin\tfrac{k\Delta x}{2}\right] \\
\tau_{j+1/2}^{n} - \tau_{j-1/2}^{n} &= \\
&= \mathrm{B}\exp\left(-i\omega n\,\Delta t + ik(j+1/2)\,\Delta x\right) - B\exp\left(-i\omega n\,\Delta t + ik(j-1/2)\,\Delta x\right) \\
&= \mathrm{B}\exp\left(-i\omega n\,\Delta t + ik(j+1/2)\,\Delta x\right)\left[\exp\left(ik\,\Delta x/2\right) - \exp\left(-ik\Delta x/2\right)\right] \\
&= \tau_j^n\left[2\,i\sin\tfrac{k\Delta x}{2}\right]
\end{aligned} \tag{70}$$

Substituting the final expressions of the velocity and traction terms in (65), the scheme becomes

$$\begin{aligned}
\nu_j^{n+1/2} &= \nu_j^{n-1/2} + \frac{1}{\rho}\frac{\Delta t}{\Delta x}\tau_j^n\left[2\,i\sin\frac{k\Delta x}{2}\right] \\
\tau_{j+1/2}^{n+1} &= \tau_{j+1/2}^{n} + \mu\frac{\Delta t}{\Delta x}\nu_{j+\frac{1}{2}}^{n+\frac{1}{2}}\left[2\,i\sin\frac{k\Delta x}{2}\right]
\end{aligned} \tag{71}$$

Adjusting the second equation of (71) to be in the same grid point as that of the first equation, one obtains:

$$\tau_j^{n+1/2} = \tau_j^{n+1/2} + \mu\frac{\Delta t}{\Delta x}\nu_j^n\left[2i\sin\frac{k\Delta x}{2}\right] \tag{72}$$

Let $\Delta = \Delta t/\Delta x$ and $\hat{S}\sin(k\Delta x/2)$. The scheme in (71) with (69) can be rewritten as

$$\begin{cases}
\nu_j^{n+1/2} = \nu_j^{n-1/2} + \frac{2i}{\rho}\hat{S}\Delta\tau_j^n \\
\qquad \nu_j^n = \nu_j^n \\
\tau_j^{n+1/2} = \tau_j^{n-1/2} + 2i\mu\hat{S}\Delta\nu_j^n \\
\qquad \tau_j^n = \tau_j^n
\end{cases} \tag{73}$$

which can be expressed in a matrix form

$$\boldsymbol{U_j^{n+1/2}} = \boldsymbol{G}\,\boldsymbol{U_j^n} \tag{74}$$

where

$$\boldsymbol{U_j^{n+1/2}} = \begin{bmatrix} \nu_j^{n+1/2} \\ \nu_j^n \\ \tau_j^{n+1/2} \\ \tau_j^n \end{bmatrix} \quad \boldsymbol{G} \begin{bmatrix} 0 & 1 & \frac{2i}{\rho\hat{S}\Delta} & 0 \\ 1 & 0 & 0 & 0 \\ 2i\mu\hat{S}\Delta & 0 & 0 & 1 \\ 0 & 0 & 1 & 0 \end{bmatrix} \quad \boldsymbol{U_j^n} = \begin{bmatrix} \nu_j^n \\ \nu_j^{n-1/2} \\ \tau_j^n \\ \tau_j^{n+1/2} \end{bmatrix}$$

The matrix G is called the *amplification factor*, which does not depend on time since it is obtained from the constant coefficients of the terms of the linear PDE [40]. Hence, one can write (74) into

$$\boldsymbol{U_j^{n+1/2}} = \boldsymbol{G^{m+1}}\,\boldsymbol{U_j^0} \tag{75}$$

since $\boldsymbol{G}$ does not depend on time and $\left\|\boldsymbol{U_j^n}\right\| \leq \left\|\boldsymbol{U_j^0}\right\|$ from (69), and since

$$\left\|\boldsymbol{U_j^{n+1/2}}\right\| = \left\|\boldsymbol{G^{m+1}}\,\boldsymbol{U_j^n}\right\| \leq \|\,\boldsymbol{G}\,\|^{m+1}\left\|\boldsymbol{U_j^0}\right\|$$

the numerical solution will be bounded if and only if

$$\|\,\boldsymbol{G}\,\| \leq 1 \tag{76}$$

where $\|\cdot\|$ is a matrix norm. It is sufficient for the condition in (75) for the stability of the numerical scheme in (65). It is required for the maximum of the eigenvalues of $\boldsymbol{G}$ to have the modulus less than or equal to unity to satisfy the von Neumann stability.

The characteristic equation for matrix $\boldsymbol{G}$ in (74) is

$$1 - 2\lambda^2 + 4\Delta^2\hat{S}^2\frac{\mu}{\rho}\lambda^2 + \lambda^4 = 0 \tag{77}$$

It is then required that the roots of (77) have absolute values smaller than or equal to one. Letting $z = \lambda^2$ and $a = \Delta^2\hat{S}^2\mu/\rho$, the equation in (77) becomes

$$z^2 + (4a - 2)z + 1 = 0$$

the roots of which are

$$z_{1,2} = -2a + 1 \pm 2\sqrt{a^2 - a} \tag{78}$$

If $0 < a \leq 1$, then $|z_{1,2}| \leq 1$ which is the stability condition. Then, it follows that

$$\Delta^2\frac{\mu}{\rho}\hat{S}^2 = \left(\frac{\Delta t}{\Delta x}\right)^2\frac{\mu}{\rho}\sin^2\left(\frac{k\Delta x}{2}\right) \leq 1 \tag{79}$$

Hence, the condition for the time and space increments for the staggered grid is obtained so that the numerical scheme in (65) is stable, and this condition is given by

$$\Delta t \leq \Delta x\left(\frac{\rho}{\mu}\right)^{1/2} = \frac{\Delta x}{\beta} \tag{80}$$

where β is the speed of the S-wave propagation from (53). Hence, the scheme in (65) is *conditionally stable*.

Since (65) is consistent and stable given that (79) is satisfied, then by the Lax-Richtmyer Theorem, the numerical solution to (65) is convergent. The condition in (79) or (80) is called the *Courant-Friedrich-Levy* (CFL) condition [38]. To ensure stability, the time step must be a fraction of the ratio of the grid spacing and the S-wave velocity. This fraction is called the CFL number, which is equal to $\beta\Delta t/\Delta x$.

The required preliminary concepts for the ground motion prediction and how to solve it numerically have been presented so far. The next Section will discuss in detail the PSHA Methodology to estimate the feasible ground shaking level on a site with relaxation of the ergodic assumption of the Classical PSHA.

4. PSHA Methodology

In the previous Sections, the need for the estimation of the seismic hazard was presented at the beginning, then the basic notions of seismology were discussed, and lastly, the solution to the elastodynamic equation was examined for the ground motion prediction. Hence, the probabilistic approach of estimating the seismic hazard level will be presented in this Section. Kramer's [1] outline of PSHA was used to discuss the methodology with the exception of using the Physics-based Ground Motion Prediction to abandon the ergodic assumption in conducting PSHA. Readers who need a review in the fundamental concepts in probability are referred to Appendix A to this paper.

4.1. Delineation of Seismic Sources

All significant seismic sources that can produce strong ground shaking will be considered when conducting a PSHA. For this study, active fault source models were used extensively from Valentini, Visini, and Pace [25] and Valentini et. al. [24] since fault geometry parameters were provided in their papers, and the shapefiles of fault traces were obtained online as per recommendation of Valentini, Visini, and Pace [25] which is available for public use. Figure fig4.1 and Table 3 show the fault traces located within a 100km radius from the city of L'Aquila as well as the master fault associations of these fault traces based on Valentini, Visini, and Pace [25], both of which are mapped using ArcGIS Pro from the shapefile obtained online. Table 2 shows the fault parameters needed for a seismic hazard analysis such as the fault length (in km), the dip angle (in degrees), the seismogenic thickness (ST in km), the minimum and maximum slip rates observed (SR_{min},SR_{max} in mm/year), the observed earthquake event M_{obs} and its standard deviation , and the recent instrumental recording of the year of occurrence.

Table 2 shows that the Fucino fault is the longest with a length of 45.9km, while Velino is the shortest with a length of 11.5km. All the faults have a dip angle less than 90^0, which suggests that all the faults are dip-slip faults. All faults have fault traces located on the surface [25], which implies that the given seismogenic thicknesses in Table 2 is the deepest part of the fault for all sources. For slip rates, Leonessa and Pizzalto-Cinque Miglia have the smallest slip rates of 0.1mm/year,

while Fucino has the biggest slip rate of 1.4mm/year. The slip rate is the annual movement of the fault which imposes shear stresses on the fault causing an elastic build-up of strain energy [1].

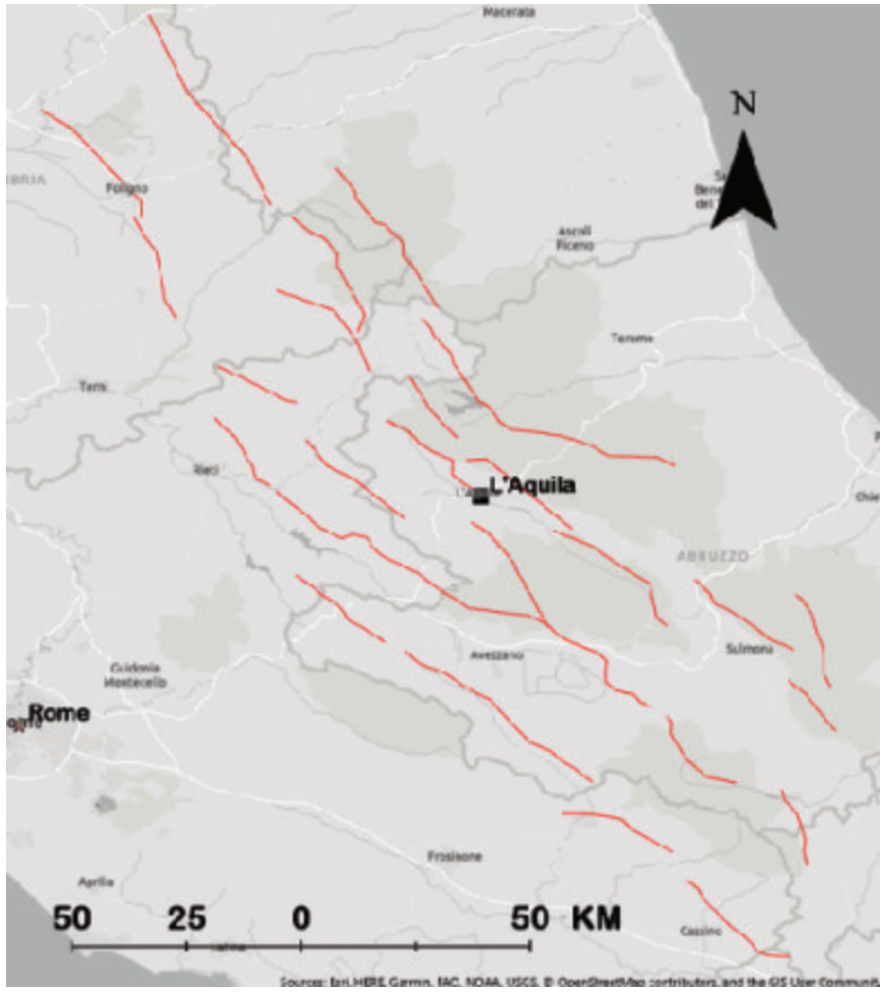

Figure 18. Fault traces located at a radius of 100 km from L'Aquila
Source: Valentini, Visini and Pace, 2017 [25]

Earthquake occurrences were recorded only by several fault sources, which are Colfiorito, Fucino, Mount VettoreMount Bove, Paganica, Pizzoli-Pettino, Rieti, Salto Valley, Sora, Umbrea Valley North and the South segments, and Velino, according to Table 2. Therefore, additional information coming from the paleoseismological records and other literature which can provide the fault activity was required to fully characterize a seismic source.

Historical seismicity and paleoseismological records were extracted from various literature sources to characterize the fault activity from Valentini et

al. [24] and Valentini, Visini, and Pace [25]. For the purpose of showing such information, Table 2 presents the historical, instrumental, and paleoseismological records of past earthquake occurrences in all the faults considered in this study. The data was used by Valentini et al. [24] for estimating the recurrence period of earthquakes by considering the past earthquake occurrences the values of which were used to calculate the seismic moment in each fault.

It follows from Table 2 that all the seismic sources show evidence of fault activity even before the 20^{th} century except for Carsoli, Cassino, Leonessa, Liri, Maiella, Marsicano, Montereale, and Sella di Corno. For these faults that have no earthquake association, additional assumption was used to characterize the fault activity to be discussed later.

4.2. Distance Calculations

After identifying all the potential seismic sources that can significantly contribute to the seismic hazard on a site, the distances of all possible earthquake scenarios must be obtained. These distances were used as lengths of wave propagations for the ground motion prediction.

In this study, ArcGIS Pro was used to discretize all the active fault sources into 100 equal areas and the Calculate Geometry Functions of the software were used to obtain coordinates of the centroid in the latitude and longitude coordinates. The distances from each centroid were obtained with the coordinates of L'Aquila at 42.3498° N, 13.3995° E. Next, the distances obtained were subdivided into 10 equally spaced bins. Then, a histogram showing the number of distances that fall into a certain bin was made for each seismic source, the probability mass functions of which are presented in Appendix B to this paper.

5. Magnitude-Frequency Distributions

The next thing to come after the calculations of source-to-site distances is the modeling of the uncertainty in the size of earthquakes. Before doing this, usually the maximum magnitude that a fault can produce must be computed first along with the uncertainty to produce the PDF of the magnitude. Then, the associated activity rates per fault with the corresponding probable magnitudes of occurrence must be computed for seismic hazard computations in (6). This Section will discuss in detail all the steps that are needed to model the size uncertainty and compute the activity rates.

5.1. Maximum Magnitude Determination

There are five methods used by Valentini, Visini, and Pace [25] and Valentini et al. [24], based on the FiSH Code, a MATLAB Code made by Pace, Visini, and Peruzza [41], to determine the maximum magnitude to be considered in each active fault source model. The following summarizes each method and the steps needed to obtain the maximum size:

Method 1: The average annual displacement was taken with the minimum and maximum slip rates given in Table 2. Then, this displacement and area A

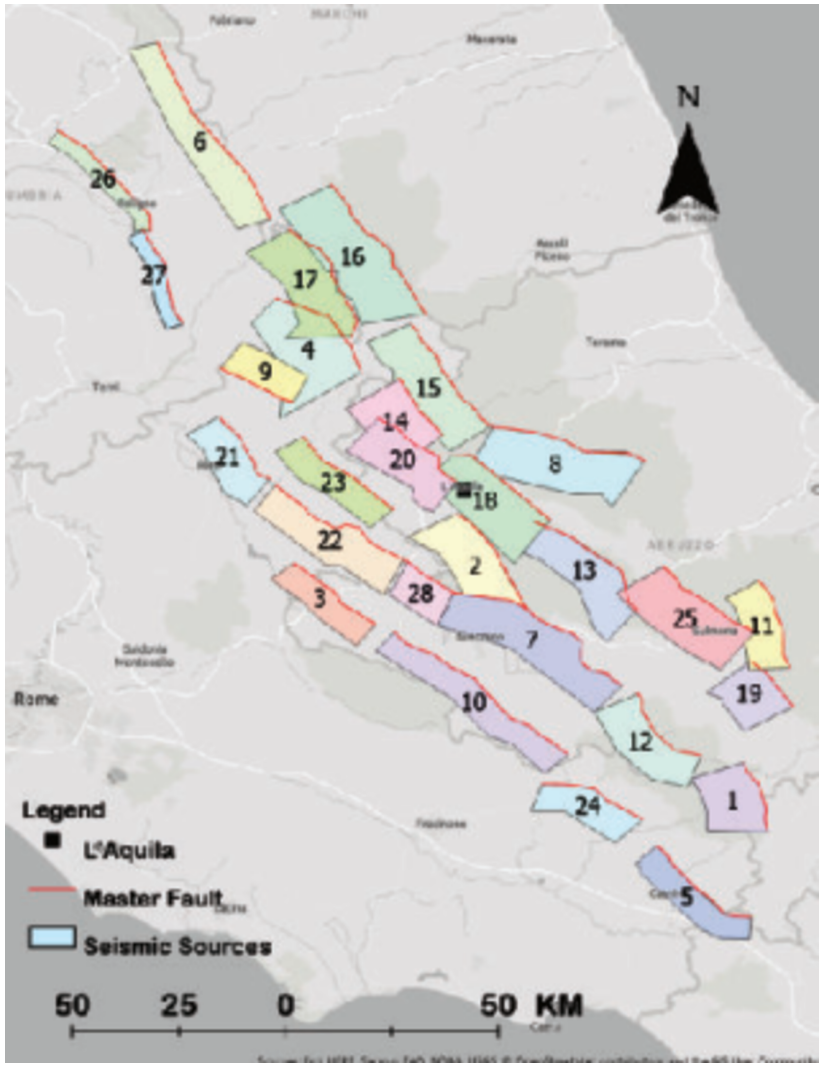

Figure 19. Active fault sources with corresponding master fault traces [25]

(which can be computed from the seismogenic thickness, dip angle, and length as per Subsection 2.3) were used to compute the seismic moment based on the formula in (7), and converting the seismic moment in units of N-m. Then, the moment magnitude is calculated using (36).

Method 2: Given the rupture length L and area A, the maximum earthquake size can be computed using the relationships formulated by Wells and Coppersmith [42] using the global earthquake occurrence data. These are given by:

$$M_w = 5.08 + 1.16L, \quad \sigma_{M_w} = 0.28, \tag{81}$$

$$M_w = 4.07 + 0.98A, \quad \sigma_{M_w} = 0.28. \tag{82}$$

Table 2. Fault parameter needed for PSHA [25]

ID	NAME	Length (km)	Dip (°)	ST (km)	SRmin	SRmax	Mobs	sdMobs	Last eq time
1	Barrea	17.4	50	13	0.2	0.6	-	-	1984
2	Campo Felice-Ovindoli	26.5	50	13	0.7	1.2	-	-	-
3	Carsoli	20.5	50	11	0.35	0.6	-	-	-
4	Cascia-Cittareale	24.2	50	13.5	0.3	0.9	-	-	-
5	Cassino	24.6	60	11	0.25	0.5	-	-	-
6	Colfiorito	45.9	37	8.5	0.25	0.75	6.2	0.33	1997
7	Fucino	38	50	13	0.4	1.4	7.1	0.09	1915
8	Gran Sasso	28.7	50	15	0.6	1	-	-	-
9	Leonessa	14.9	55	12	0.1	0.7	-	-	-
10	Liri	42.5	50	11	0.3	1.26	-	-	-
11	Maiella	21.4	55	15	0.7	1.6	-	-	-
12	Marsicano	20	50	13	0.5	0.7	-	-	-
13	Middle Aternum Valley	29.1	50	14	0.3	0.4	-	-	-
14	Montereale	15.5	50	14	0.3	0.9	-	-	-
15	Mount Gorzano	30	45	12	0.7	1.1	-	-	-
16	Mount Vettore-Mount Bove	34	47	11	0.35	1.05	6.5	0.1	2016
17	Nottoria-Preci	29	50	12	0.3	0.9	6.9	0.11	-
18	Paganica	23.7	50	14	0.45	0.71	6.5	0.34	2009
19	Pizzalto-Cinque Miglia	18	50	15	0.1	0.6	-	-	-
20	Pizzoli-Pettino	21.5	50	14	0.3	0.9	6.7	0.17	1703
21	Rieti	17.6	50	10	0.3	0.5	6.3	0.34	1899
22	Salto Valley	28.4	50	11	0.5	0.7	-	-	668
23	Sella di Corno	28.4	60	13	0.35	0.7	-	-	-
24	Sora	20.4	50	11	0.15	0.45	6.3	0.2	1655
25	Sulmona	22.6	50	15	0.5	0.7	-	-	-
26	Umbra Valley N	28.6	50	4.5	0.4	1.2	6.4	0.1	1832
27	Umbra Valley S	24	50	4.5	0.4	1.2	-	-	1878
28	Velino	11.5	50	12.5	0.7	0.9	5.7	0.1	1904

Method 3: Similarly to Method 2 using the length from Table 2 but modifying it with respect to the aspect ratio of the fault dimensions prediction by Peruzza and Pace [43] as mentioned by Pace, Visini, and Peruzza [41].

Method 4: Lastly, the maximum observed magnitude of occurrence using Table 2 and 3.

Table 3. Historical, Instrumental, Paleoseismological Occurrences in each fault[25, 24]

		Historical				Instrumental		Paleoseismo.
ID	**NAME**	Date	Io	Mw	sDMw	Date	Mw	Age
1	Barrea					07/05/1984	5.9	
2	Campo Felice-Ovindoli							+890/+1300 3830/3375 7560-4980
3	Carsoli							
4	Cascia-Cittareale	06/11/1599 16/11/1916	IX VIII	6.1 5.5	0.2 0.1			
5	Cassino							
6	Colfiorito	30/04/1279	IX	6.2	0.2	26/09/1997	6.0	
7	Fucino	13/01/1915	XI	7.0	0.1			+426/+782 3500-3300 5944-5618
8	Gran Sasso							3381/+1000 6573/5475
9	Leonessa							
10	Liri							
11	Maiella							
12	Marsicano							
13	Middle Aternum Valley							200/100 BCE 6381/3511
14	Montereale							
15	Mount Gorzano	07/10/1639 28/04/1646	X-XI IX	6.2 5.9	0.2 0.4			8320/+1000 8245/8365
16	Mount Vettore-Mount Bove					30/10/2016	6.5	+250/+450 −2200/−1800 −3700/−2800 −6000/−4000
17	Nottoria-Preci	01/12/1328 14/01/1703 27/06/1719 12/05/1730 22/08/1859 23/02/1879	X XI VIII IX VIII-IX VIII	6.5 6.9 5.6 6.0 5.7 5.6	0.3 0.1 0.3 0.1 0.3 0.3	19/09/1979	5.8	+1400/+1800 -500/-50
18	Paganica	27/11/1461	X	6.5	0.5	06/04/2009	6.3	+890/+1150 -760/+670 -2900/-760
19	Pizzalto-Cinque Miglia							-800/+1030 5685/4890

Table 4. Table 3 continued [25, 24]
Note: +/- indicates the year in CE/BCE, years are presented from the latest to earliest earthquake occurrence, each row representing the start and end years of possible earthquake activity

		Historical				**Instrumental**		**Paleoseismo.**
ID	**NAME**	Date	Io	Mw	sDMw	Date	Mw	Age
20	Pizzoli-Pettino	02/02/1703	X	6.7	0.1			1400/1800
21	Rieti	01/12/1298	IX-X	6.3	0.5			
22	Salto Valley	09/09/1349	IX	6.3	0.1			
23	Sella di Corno							
24	Sora	24/07/1654	X-XI	6.3	0.1			
25	Sulmona							+80/+240 4500 8450/6315 after 9000
26	Umbra Valley N	13/01/1832 12/02/1854	X VIII	6.4 5.6	0.1 0.3			
27	Umbra Valley S	05/06/1767 15/09/1878	VII-VIII VIII	5.5 5.5	0.4 0.2			
28	Velino	24/02/1904	IX	5.7	0.1			-1400/1000

The FisH code then will take the *average* of all the four values of M_{max} in methods 1-3, and the PDFs of each magnitude value centered at the predicted M_{max} which follows the normal distribution are summed up, and the new PDF is fitted to a normal curve centered at the average of the four values with a new standard deviation sDM_{max}. The criteria to select M_{max} are as follows [24]: a) if $M_{obs}+sDM_{obs}$ is lower than $M_{max}-sDM_{max}$, then use M_{max}. b) if $M_{obs}-sDM_{obs}$ is larger than $M_{max}+sDM_{max}$, then the fault geometries and historical seismicity are reviewed. c) if $M_{obs}+sDM_{obs}$ is within the range of $M_{max}\pm sDM_{max}$, then M_{obs} is used with the given sDM_{obs} in Table 2. Take note that this selection is only valid if there is an observed earthquake. Otherwise, M_{max} predicted by the FiSH code will be used.

5.1.1. Earthquake Recurrence

The recurrence of earthquakes in a certain region can be modeled by the *Guttenberg-Richter* (G-R) Relationship [1, 32] and is given by:

$$\log\lambda_m = a - bM, \tag{83}$$

where λ_m is the mean annual rate of exceedance of earthquakes (in earthquakes/yr) of magnitude M, a is the slope of the regression line related to the activity rate of earthquakes, and b is called the *b-value* of a region which is the relative likelihood of large and small earthquakes. This can be interpreted as an increase in the number of large earthquakes compared to small earthquakes with

the decreasing *b-value*. According to McGuire [15], this b-value ranges from 0.7 to 1.1; according to Shearer [32], the value ranges from 0.8 to 1.2; and 0.7 to 1.3 according to Kramer and Scawthorn [2]. In the papers of Valentini et al. [25, 24] the assumed value was 1.0.

This equation was introduced by Guttenberg and Richter in 1944, as mentioned by Kramer [1] and they performed regression analysis for the magnitude size and their annual frequencies in Southern California.

Manipulating (83) and with a change of the base, it can be rewritten into:

$$\lambda_m = v_o \exp(-\beta M), \tag{84}$$

where $v_o = 10^a$ and $\beta = 2.303b$. It can be seen from (84) that the magnitude can go from $-\infty$ to $+\infty$ which is not possible. Then (84) has to be bounded with a minimum value and a maximum value, with a minimum value of 4.0 to 5.0 for engineering purposes [1], and a maximum value which is dictated by the properties of the fault such as geometry, slip rates, etc. Valentini et al. [24] used a *truncated G-R model* (TGR) which utilizes minimum M_o and maximum M_u and is given by:

$$\lambda(m) = \lambda_o \frac{\exp(-\beta m) - \exp(-\beta M_u)}{\exp(-\beta M_o) - \exp(-\beta M_u)}, \tag{85}$$

where $\lambda(m)$ is the mean annual rate of exceedance as a function of magnitude m, λ_o is the smoothed rate of earthquakes at $M_w = 5.5$, and $\beta = 2.303b$. The resulting probability distribution of the truncated G-R can be expressed in terms of the *cumulative distribution function (CDF):*

$$F_M(m) = P[M < m | m > M_o] = \frac{\lambda(M_o) - \lambda(m)}{\lambda(M_o)} = \frac{\exp(-\beta M_o) - \exp(-\beta m)}{\exp(-\beta M_o) - \exp(-\beta M_u)}, \tag{86}$$

and the corresponding PDF is given by:

$$f_M(m) = \frac{d}{dm} F_M(m) = \frac{\beta \exp(-\beta m)}{\exp(-\beta M_o) - \exp(-\beta M_u)}. \tag{87}$$

The TGR model for an earthquake recurrence to characterize the uncertainties in the size of earthquakes if there is insufficient data about the activity of the fault. However, if there is evidence of fault movements, then a *characteristic earthquake model* can be used.

To compute the activity rates using the TGR model, simply substitute the magnitude of consideration to (85) given the value of the parameter λ_o and the result is interpreted as the activity rate of the fault having a magnitude of m or greater.

For this study, a minimum magnitude of 5.5 and maximum magnitude $M_u = M_{max}$ for each fault was used for the TRG Model of Magnitude Distribution,

and a binning scheme of 0.1 was used. As mentioned before in Section 1, the activity rates were obtained from the link in the Supporting Information mentioned by Valentini et al. [24].

6. Characteristic Earthquake Model

The characteristic earthquake model can be used with evidence of a paleoseismic movement of faults, which suggests that in a certain number of years called the *return period* or *mean recurrence time* (T_{mean}), that the fault will produce a similar magnitude (within ± 0.5 from the maximum magnitude) which is called the *characteristic earthquake* [1].

To estimate T_{mean}, Valentini, Visini, and Pace [25] and Valentini et al. [24] used the method of Field et al. [44] which is given by:

$$T_{mean} = \frac{1}{CharRate} = \frac{10^{1.5M_{max}+9.1}}{\mu DLW}, \tag{88}$$

where $CharRate$ is the mean annual rate of occurrence of a characteristic earthquake, M_{max} is the computed mean maximum magnitude in a fault, μ is the shear modulus, D is the average long term displacement, and L and W are the length of the fault segments along the direction of strike and the downdip width of the fault, respectively. This length may not be the total length of the fault, but only a part of the entire fault [32].

Theoretically, the probability distribution of magnitude is uniform for a characteristic earthquake, nonetheless, some literature employs the use of a truncated normal distribution with the value of magnitude within the range $M_{max} \pm sDM_{max}$ with a binning scheme of 0.1 [24, 25]. The equation of a normal curve for the magnitude PDF is given by:

$$f_M(m) = \frac{1}{\sigma M_{max}\sqrt{2\pi}} \exp\left(-\frac{[m - M_{max}]^2}{2sDM_{max}{}^2}\right). \tag{89}$$

To compute the activity rates using the Characteristic Earthquake Model, Valentini, Visini, and Pace [25] and Valentini et al. [24] used the Characteristic Brownian Passage Time (CHPBT) model which is a Gaussian curve according to the PDF [24, 45, 41]:

$$P(t) = \sqrt{\frac{T_{mean}}{2\pi\alpha^2 t^3}} \exp\left[-\frac{(t - T_{mean})^2}{2T_{mean}\alpha^2 t}\right], \tag{90}$$

where T_{mean} is obtained from (88), α is the Coefficient of Variation equal to the ratio of the standard deviation of T_{mean} which can be obtained through slip rates [24, 41], and t is the time (in years) of the last earthquake observed in a fault.

For each of the magnitudes in the interval $[M_{max} - sDM_{max}, M_{max} + sDM_{max}]$, a fictitious recurrence time T_{fict} is computed for a given magnitude, and is given by:

$$T_{fict} = \frac{1}{\lambda_m} = \frac{-\Delta T}{\ln(1-P|elap)}, \tag{91}$$

where λ_m is the activity rate of the fault having a magnitude of m or greater, ΔT is the selected observation period (depending on the design life of a structure typically set for 50 years) and $P|elap$ is the conditional probability that an event occurs during the next ΔT year, given an elapsed time T_{elap} since the last event, is defined as follows:

$$P|elap = P\left(T_{elap} \le T + T_{elap} + \Delta T | T > T_{elap}\right) = \frac{P\left(T_{elap} \le T \le +T_{elap} + \Delta T\right)}{1 - P\left(0 \le T \le T_{elap}\right)}, \tag{92}$$

for which the expressions in the numerator and the denominator of the RHS of (92) can be obtained by numerically integrating (90) with the corresponding bounds $T_{elap} \le T \le +T_{elap} + \Delta T$ and $0 \le T \le T_{elap}$ for the numerator and the denominator, respectively. This probability in (92) is set to the probability considering a Poisson process with parameter $\lambda = 1/T_{fict}$ and $t = \Delta T = 50$ years. Figure 20 illustrates the concept used by the CHBPT model of computing the activity rates of earthquakes.

Hence, the following is employed in this study: a) the TGR model is used for fault sources that have no data regarding the last earthquake occurrence from Table 2; b) in the case that the active fault sources have earthquake associations based on Table 3, the TGR is used; if there is at least one earthquake having a magnitude lower than the magnitude range for the CHBPT, c) otherwise, the CHBPT is used. Both b) and c) are with reference to Valentini et al. [24].

In determining the values of the earthquake parameters related to the magnitude PDF, the results from Valentini, Visini, and Pace [25] and Valentini et al. [24] are used in this study.

Table 5 lists the maximum magnitude M_{max} and its standard deviation *sDMax*, mean recurrence time T_{mean} (in years), the coefficient of variation *COV*, and the time elapsed T_e (in years). For some faults with no observed earthquakes according to Table 3, an assumed value of 717 years was used as per the assumption of Valentini et al. [24] which is the minimum number of years of recording of earthquakes. The values listed in Table 5 were used to calculate the seismic moment M_o by multiplying the seismic moment rate to the mean recurrence time, and this seismic moment can be correlated to the energy released during earthquakes and the dynamic stress drop which describes the total change in stress during earthquakes as mentioned in Section 2.3 of this paper.

It follows from Table 5, that the Velino fault has the lowest maximum magnitude of 6.1, while the Fucino and Liri faults have the highest maximum magnitude of 6.8, which were determined using the four methods mentioned in Subsection 5.1. The values of the standard deviations for each maximum magnitude of each fault were determined from the four methods as well, the

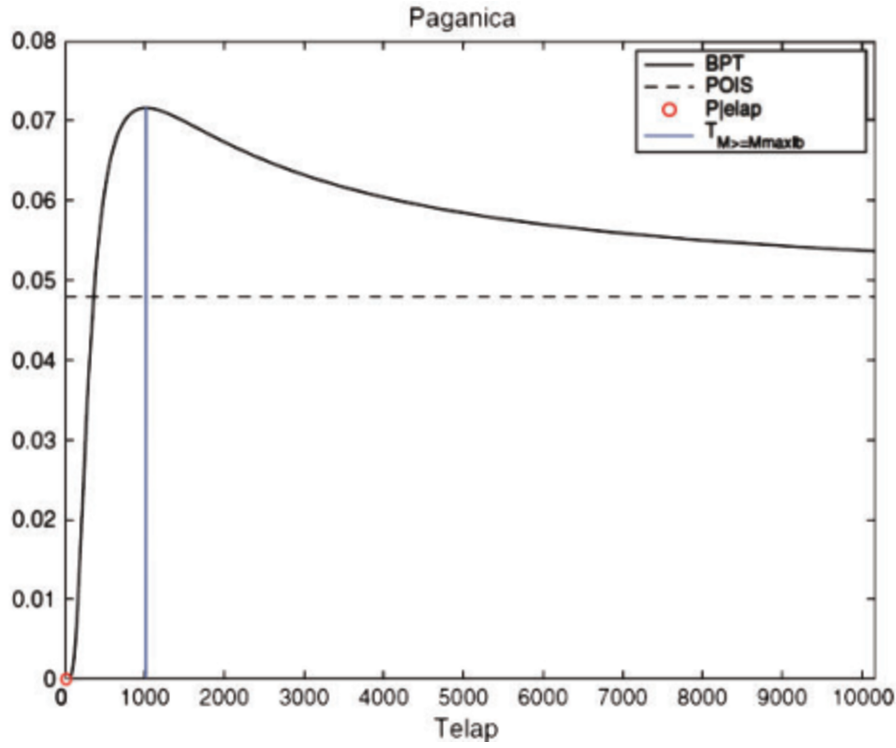

Figure 20. A CHBPT model was employed for the Paganica Fault showing the BPT probability values for each value of $t = T_{elap}$. $P|elap$ in (91) obtained from BPT in (89) is computed for a given T_{elap}, and this probability is equated to the Poisson probability corresponding to 50 years of observation with a parameter equal to $1/T_{fict}$ which is the mean occurrence rate corresponding to a given magnitude and T_{mean} which are related by (87)[41]

values of which were used for the CHBPT models to determine the upper bound of the magnitude range for determining the activity rates.

The mean recurrence time T_{mean} was determined using (87), and other parameters such as CV and seismic moment rates were obtained from the FiSH Code calculations made by Valentini et al. [24]. Some values of the elapsed time were obtained from the study of Valentini et al. [24], and for those seismic sources that were not considered in their study, a value of 717 years was assumed as mentioned by Valentini et al. [24] which is the minimum required number of years of recording for an earthquake catalogue to be complete.

7. Physics-Based Ground Motion Prediction

The PGA can be approximated by simulating a ground motion by solving the Elastodynamic Equation with the Hooke's Law in (40) the approximation of which is given by (63) using the finite difference method in a staggered grid, given the initial and boundary data in Subsection 3.2.1.

The Preliminary Reference Earth Model (PREM) was used in this study for the density and S-wave velocity of rock which assumes a 1-D model of the Earth's seismic velocities [32]. For the computation of normal stresses, a dry density of 2.60 g/cc was used from this model and this assumes depths of several kilometers from the ground surface. The S-wave velocity used was taken from the same model and is equal to 3.2 km/s.

The parameters required for the boundary condition for the traction such as the rupture velocity v_r, the rupture time t_r, the fracture energy G, the dynamic stress drop $\Delta\sigma_d$, and the characteristic time t_1 were calculated in each magnitude of the occurrence per fault, ranging from M_{min} to M_{max}. Seismic moments were computed by multiplying the seismic moment rate to the mean recurrence time. For each magnitude, seismic moments were interpolated from M_{max} using the relation of the moment magnitude and the seismic moment in (8).

The domain for the computational framework is $\left[0, L_p\right] \times [0, T]$, where L_p is the length obtained from the binning in Subsection 4.2 for distances, T for the seismogram duration, which was 10 sec plus the time which it takes for the S-wave to reach the site, which is given by L_p/β, since at the time before L_p/β, there is no ground motion produced for the site to perceive it. For this study, a uniform time step of $\Delta t = 0.005$ sec was used which is a typical time step in a true seismogram. Then, a uniform grid spacing of 20 m was used making the CFL number equal to 0.80 which satisfies the stability and convergence of the numerical scheme. This spacing is chosen with conservatism, for which the actual ground motions data obtained from the Engineering Strong Ground Motion Database [46] was simulated using the numerical scheme. The ground motions used came from the M_w 6.1 L'Aquila and M_w 6.5 Central Italy earthquakes which occurred on April 6, 2009 and October 30, 2016, respectively.

For the PGA calculations, a Matlab Script is provided in Appendix C to this paper. All the important parameters related to the simulation were computed in MS Excel.

All possible lengths L_p from Subsection 4.2 were considered, and the resulting seismograms were transformed into acceleration vs. time by taking the slope of velocity-time plots in each time step, assuming no acceleration at the beginning of the simulation. Then, the peak values of the acceleration for each magnitude-distance pair were obtained for all seismic sources. These PGAs are grouped according to their respective magnitude of the occurrence and the propagation distance, and the corresponding probability of exceedance $P[Y > y|rup_n]$ of a PGA value given its distance and magnitude were computed by taking the total number of distances whose PGA Y was greater than a reference PGA y for hazard calculations ($N[R_{Y>y}]$), divided by the total number of distances in each fault, which is $N_R = 100$. Mathematically, this is given by:

$$P[Y > y|rup] = \frac{N\left[R_{Y>y}\right]}{N_R}. \tag{93}$$

Table 5. Maximum Magnitude and its standard deviation, mean the recurrence time (in years), the coefficient of variation, the time elapsed (in years), and the seismic moment rate (in N-m/yr) [24]. * means that an assumed value of 717 years is used for complete years of recording as per the assumption in their study

id	Name	Mmax	sdMmax	T_{mean} (years)	COV	T_{elap} (yrs)	Seismic Moment Rate (N-m/yr)
1	Barrea	6.3	0.3	1001	1.15	35	3.54E+15
2	Campo Felice Ovindoli	6.6	0.2	851	0.74	702	1.18E+16
3	Carsoli	6.4	0.2	1195	0.74	717*	4.19E+15
4	Cascia Cittareale	6.5	0.2	922	0.85	717*	7.68E+15
5	Cassino	6.5	0.2	2611	0.77	717*	2.71E+15
6	Colfiorito	6.4	0.2	1245	0.85	22	4.40E+15
7	Fucino	6.8	0.3	1791	1.18	104	1.11E+16
8	Gran Sasso	6.7	0.3	1090	1.07	3419	1.30E+16
9	Leonessa	6.2	0.3	959	1.28	717*	2.62E+15
10	Liri	6.8	0.3	2822	1.2	717*	7.07E+15
11	Maiella	6.5	0.2	524	0.79	717*	1.35E+16
12	Marsicano	6.5	0.2	1104	0.71	717*	6.11E+15
13	Middle Aternum Valley	6.6	0.2	2009	0.71	2219	4.98E+15
14	Montereale	6.3	0.3	696	1.15	717*	5.10E+15
15	Mount Gorzano	6.6	0.2	898	0.73	380	1.11E+16
16	Mount Vettore Mount Bove	6.7	0.3	2042	1.15	3	6.92E+15
17	Nottoria Preci	6.6	0.3	1173	0.7	316	6.39E+15
18	Paganica	6.5	0.2	1113	0.73	10	7.54E+15
19	Pizzalto C Miglia	6.5	0.2	1354	1.26	989	3.70E+15
20	Pizzoli-Pettino	6.5	0.2	1001	0.85	316	7.07E+15
21	Rieti	6.3	0.3	1294	1.07	721	2.76E+15
22	Salto Valley	6.5	0.2	1302	0.71	668	5.17E+15
23	Sella di Corno	6.5	0.2	1370	0.77	717*	5.17E+15
24	Sora	6.4	0.2	1939	0.85	365	2.64E+15
25	Sulmona	6.5	0.2	855	0.71	1919	7.96E+15
26	Umbrea Valley N	6.3	0.4	2411	1.47	187	1.47E+15
27	Umbrea Valley S	6.2	0.4	1707	1.47	141	1.47E+15
28	Velino	6.1	0.3	395	1.04	115	4.50E+15

The reference PGAs (in terms of g's) used for this study were as follows: 0.01 to 0.09 (in multiples of 0.01) and 0.10 to some upper limit, which is the maximum predicted PGA for all rupture scenarios.

8. Seismic Hazard Calculations

Hazard calculations were based on Tarbali et al. [19] and Tarbali et al. [20] which are rupture-based scenarios, and for this study it is the magnitude occurrence in the fault source. The probability of exceedances was computed based on the frequencies of the predicted PGA as a function of the distance given the magnitude of the occurrence.

From (6), the hazard rate of exceedance overall rupture scenarios in all seismic sources assuming that the sources are independent of each other and collectively exhaustive, is given by

$$\lambda_{IM}(im) = \sum_{n=1}^{N_{rup}} P[Y > y|rup_n]\, \lambda_{Rup}(rup_n), \tag{94}$$

where $P[Y > y|rup]$ is the probability of exceedance in (93), $\lambda_{Rup}(rup_n)$ is the hazard rate of the given rupture scenario (magnitude of occurrence) which is the probability of occurrence of the magnitude multiplied to the activity rates in a given magnitude.

A series of reference PGA values were used to construct the *hazard curve*, the plot of PGA values vs. the hazard rate or the mean annual rate of exceedance for a given site [1], which is L'Aquila in this study.

9. Modeling of Temporal Uncertainty

The occurrence of earthquakes is assumed to follow the Poisson distribution [1], and is given by

$$P[\lambda, t, n] = \frac{(\lambda_{IM} t)^n e^{-\lambda_{IM} t}}{n!}, \tag{95}$$

where λ_{IM} is the mean annual rate of exceedance of earthquakes (in earthquakes/yr), t is the observation time (in years), and n is the number of earthquakes. This model assumes an average number of earthquakes $\mu = \lambda_{IM} t$ occurring given a certain magnitude of earthquake at any time and obtains the probability of a certain number of occurrences.

It is known that the Poisson distribution has an assumption that the events are rare and random, and since earthquake occurrences are rare, therefore many analysts in the past till the present would assume Poisson arrivals of earthquakes. This model is used to account for the uncertainty in time, since earthquakes may recur at different time intervals. Also, the events must be independent in space, size, and time. Therefore, it is very important that earthquakes are classified as main events and not foreshocks and aftershocks, which is the reason why their occurrences are consistent with the Elastic Rebound Theory.

9.1. Probability of Exceedance

The probability of exceedance (PE) refers to the probability of exceeding zero earthquakes during an observation period given a certain magnitude of interest [10, 1], which is set to 5.5 for this study. Following the assumption of a Poisson process, using (95), the probability of zero earthquakes is $e^{-\lambda_{IM}t}$. Hence, the probability of exceeding zero earthquakes, is the complement of the event of zero earthquakes, and is given by

$$PE = 1 - e^{-\lambda_{IM}t}. \tag{96}$$

9.2. Seismic Hazard Rate and Return Period

Earthquakes are quantified in terms of their hazard rates λ_{IM} or known as the mean annual rate of exceedance [15, 1] as mentioned before. This hazard rate is obtained from equation (6), which is the direct application of the PSHA Methodology. The time of exposure (T) is the observation period mentioned in (95), which is defined as the number of years for which a structure must withstand a certain kind of earthquake and its corresponding ground motion [22].

The return period (RP) is the inverse of the hazard rate with units of years/earthquake, and the design codes express the desired ground motion for the design as a function of the return period [10]. Using (96), the return period, the time of exposure and the probability of exceedance can be related:

$$PE = 1 - e^{-T/RP}. \tag{97}$$

According to the building code, it is recommended that a structure must withstand a reference PGA which corresponds to a reference probability of exceedance of 10% within 50 years of life of a structure such as a building or a house or commercial establishment. However, a lower probability of exceedance is required for dams, bridges, power plants or lifelines [22]. Valentini, Visini, and Pace [25] and Valentini et al. [24] calculated the PGA in two return periods of 475 and 2475 years, with the corresponding probability of exceedance in 10% and 2%, respectively. Hence for this study, the return periods of 475 and 2475 years were also obtained.

10. Application of PSHA: Elastic Design Spectrum

When the structure experiences the ground acceleration at its strongest shaking, this acceleration is termed spectral acceleration (S_d) [1, 2] or pseudo-acceleration [47, 48]. This quantity has units of gals (cm/s^2) or may be expressed in terms of the gravitational acceleration constant g. It is desirable to express the ground shaking it experiences in terms of its spectral acceleration because this is the ground acceleration experienced by a structure depending on its natural period and damping mechanism [14]. Also, spectral acceleration can be used to calculate the base shear in structures [47, 48]. For many seismic hazard analyses, it is much more convenient to express the impact of the ground shaking in terms

of the spectral acceleration as they are used to calculate the design loads on the structure.

In a seismic design of structures, a structure is characterized by its *fundamental natural period T* (measured in seconds), which is the period that it takes for a structure to have a complete oscillation during vibrations [47, 48]. A structure is said to be a *short-period structure* if the period is less than one second, while structures with a period greater than or equal to one second are called *long-period structures.*

The peak ground acceleration (PGA) or peak horizontal acceleration (PHA) is the ground acceleration which corresponds to the spectral acceleration at the zero natural period [1]. When it comes to risk mitigation, it is desirable to report the impact of ground shaking in terms of PGA, since this will be the ground acceleration that will be experienced by people when an earthquake hits a certain region. This quantity may be also expressed in gals or in terms of *g*. Usually, this quantity can be measured by instruments called accelerographs during earthquakes. Kramer [1] said that PGA was the geometric mean of the peak of horizontal components of the ground motion.

In Eurocode 8, a reference PGA a_{gR} is desired to construct the so-called *Elastic Design Spectrum* as shown in Figure 21 [22] to estimate the spectral acceleration for a given natural period of a structure. The PGA is extracted from the hazard curve constructed in the PSHA, with the corresponding desired return period of earthquakes, and this PGA is called the *reference* PGA.

From Figure 21, the elastic response spectrum $S_d(T)$ is defined as

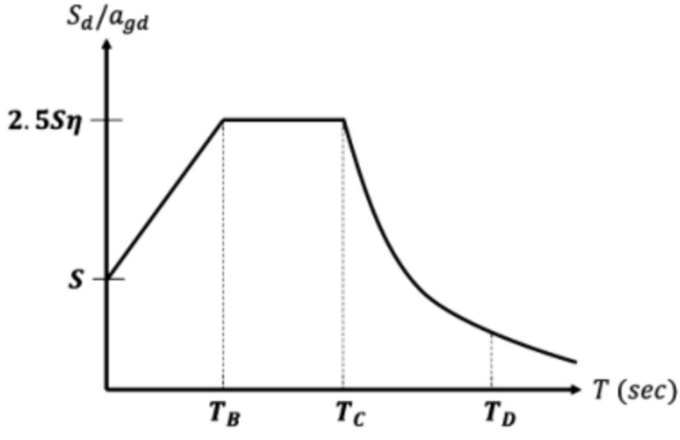

Figure 21. Elastic Design Spectrum for Seismic Design of Structures [22]

where S_d is the design spectral acceleration, $a_{gd} = \gamma a_{gR}$ is the design PGA, a_{gR} is the reference PGA from the hazard curve, γ is typically set to 1.0, S is the soil factor related to the available geotechnical investigations (set to 1.0) for rocks, T is the natural period of the structure, η is a parameter related to damping typically

set to 1.0 for 5% viscous damping of structures, $T_B = 0.15$ sec, $T_C = 0.40$ sec, and $T_D = 2.0$ sec, considering the ground motion is generated by a magnitude of 5.5 and above.

Making an elastic response spectrum for the engineering design of structures is a direct application of the PSHA, and therefore the PSHA must be conducted with care, considering all the factors required for calculating the seismic hazard. The more data is present, the better the estimation of the seismic hazard level on a site.

11. Results and Discussion

11.1. Model Used and Summary of Values for Seismic Sources

Table 6 shows the earthquake recurrence source model used and the range of values of magnitude and activity rates obtained from the attached file in the link provided by Valentini et al. [24] for each of the 28 seismic sources identified in this study. It should be noted that some seismic sources in this study were not obtained from Valentini et al. [24], and so the author used the FiSH code to determine the activity rates of these sources. The fault data of these sources were obtained from the attached file in the link provided by Valentini et al. [25].

A total of 325 scenarios were considered in this study which was determined by counting the magnitude occurrences in all seismic sources. A binning of 0.1 was used to generate the magnitude PDF. As mentioned before in Subsection 5.1.1, the following was employed for choosing a suitable earthquake recurrence model for each fault: a) the TGR model was used for fault sources that had no data regarding the last earthquake occurrence from Table 2; b) the TGR model was used in the case that the active fault sources had earthquake associations based on Table 3, if there was at least one earthquake having a magnitude lower than magnitude range for the CHBPT model; c) otherwise, the CHBPT was used. Based on Table 6, there are 15 seismic sources that were modeled as CHBPT, while the remaining 13 sources were modeled as TGR since most of these sources were not considered by Valentini et al. [24], or the seismic source had no recording of past earthquakes based on Table 3.

For the sources modeled with TGR, the minimum magnitude was set to 5.5, while the maximum magnitude was the value from Table 5 which was obtained using the FiSH Code as per data extracted from Valentini et al. [24]. For sources modeled with CHBPT, the minimum magnitude was set to $M_{max} - sDM_{max}$, while the maximum magnitude was set to $M_{max} + sDM_{max}$. As a result, the maximum magnitude considered in this study, which can be seen in Table 6, was 7.1 from the Fucino fault, followed by the Gran Sasso and Mount Bevore-Mount Bove faults with magnitude 7.0.

The activity rate is the reciprocal of the mean recurrence time of earthquakes and has units of earthquakes per year. If follows from Table 2 that the Maiella fault has the highest range of activity rates, with 2.89 x 10^{-4} to 2.89 x 10^{-3} earthquakes/year, while the Mount Vettore — Mount Bove fault has the

Table 6. The recurrence model used and the magnitude and activity rate ranges from each seismic source [25, 24]
*TGR — Truncated Guttenburg-Richter, CHBPT — Characteristic Brown Passage Time

			Magnitude		Activity Rates (eq/year)	
ID	**Source Name**	**Source Model**	**Min**	**Max**	**Min**	**Max**
1	Barrea	TGR	5.5	6.3	1.03E-04	6.48E-04
2	Campo Felice Ovindoli	CHBPT	6.4	6.8	2.15E-04	3.54E-04
3	Carsoli	TGR	5.5	6.4	1.33E-04	1.06E-03
4	Cascia Cittareale	TGR	5.5	6.5	1.21E-03	1.21E-04
5	Cassino	TGR	5.5	6.5	5.80E-05	5.80E-04
6	Colfiorito	TGR	5.5	6.4	9.27E-05	7.36E-04
7	Fucino	CHBPT	6.5	7.1	4.42E-06	7.28E-06
8	Gran Sasso	CHBPT	6.4	7	5.39E-05	8.89E-05
9	Leonessa	TGR	5.5	6.2	1.88E-04	9.44E-04
10	Liri	TGR	5.5	6.8	4.81E-05	9.61E-04
11	Maiella	TGR	5.5	6.5	2.89E-04	2.89E-03
12	Marsicano	CHBPT	6.3	6.7	1.72E-04	2.83E-04
13	Middle Aternum Valley	CHBPT	6.4	6.8	9.44E-05	1.56E-04
14	Montereale	CHBPT	6	6.6	1.20E-04	1.98E-04
15	Mount Gorzano	TGR	5.5	6.6	1.20E-04	1.51E-03
16	Mount Vettore - Mount Bove	CHBPT	6.4	7	4.93E-12	8.13E-12
17	Nottoria Preci	TGR	5.5	6.6	9.20E-05	1.16E-03
18	Paganica	CHBPT	6.3	6.7	5.13E-12	8.46E-12
19	Pizzalto C. Miglia	CHBPT	6.1	6.7	7.04E-05	1.16E-04
20	Pizzoli-Pettino	CHBPT	6.3	6.7	1.32E-04	2.18E-04
21	Rieti	CHBPT	6	6.6	7.80E-05	1.29E-04
22	Salto Valley	CHBPT	6.3	6.7	1.19E-04	1.96E-04
23	Sella di Corno	TGR	5.5	6.5	1.11E-04	1.11E-03
24	Sora	CHBPT	6.2	6.6	3.12E-05	5.14E-05
25	Sulmona	CHBPT	6.3	6.7	3.12E-05	5.14E-05
26	Umbrea Valley N	TGR	5.5	6.3	3.67E-05	2.31E-04
27	Umbrea Valley S	TGR	5.5	6.2	5.37E-05	2.69E-04
28	Velino	CHBPT	5.8	6.4	2.40E-04	3.96E-04

smallest ranges of activity rates, ranging from 4.93 x 10^{-12} to 8.13 x 10^{-12} earthquakes/year. This means that the Maiella fault is the biggest contributor to the seismic hazard in terms of the earthquake occurrence while Mount Vettore — Mount Bove is the smallest contributor to the seismic hazard. However, it should be noted that this is not conclusive for the overall seismic hazard, since this applies to the earthquake occurrence only, and does not include other factors such

as magnitude, distance, and the predicted PGA. A total of 2800 distances were generated in this study by subdividing each seismic source into 100 equal parts, and the centroids of these areas were calculated using ArcGIS Pro. The resulting distances were grouped into 10 bins per source, and the probabilities of occurrence were calculated by dividing the frequency per bin divided by 100. Table 6 shows the range of source-to-site distances (in kilometers) of the 28 seismic sources to L'Aquila. The distance PDFs can be found in Appendix B to this paper.

Table 7 shows that the Paganica fault is the nearest seismic source which can affect L'Aquila, with distances ranging from 1.64 to 21.36 km, followed by the Pizzoli-Pettino fault with distances ranging from 4.61 to 29.36 km. In 2009, the Paganica fault caused catastrophic damage to L'Aquila due to the Mw 6.3 earthquake it produced. Hence, this fault can pose a threat to the city of L'Aquila anytime without much predictability on the fault's rupture. Table 7 also shows that the farthest fault is the Umbrea Valley Fault North segment which is located ranging from 98.23 to 126.71 km. Therefore, in terms of contribution to the overall seismic hazard, the Paganica and Umbrea Valley North faults are the highest and lowest contributors to the city of L'Aquila. Since there are fault sources that are located too far away from the city, only a maximum distance of 100 km was considered for these sources since we are only concerned with such sources which can significantly contribute to the overall seismic hazard.

It should be noted here that the frequencies of the distances that were considered for the probability computations were those obtained within a 100 km radius from L'Aquila, and their frequencies were divided by 100, and not by the number of total distances that fell within 100 km, since the probability of occurrence of a certain distance within the seismic source is the subject of the source-to-site uncertainty within the source. Also, these distances were the lengths of wave propagations required for the PGA Prediction.

The resulting probability of occurrence of the distance per magnitude occurrence is the resulting probability of exceedance per rupture scenario in (93).

12. Peak Ground Acceleration Prediction

As mentioned before in Subsection 5.1.1, two actual ground motions coming from L'Aquila and Central Italy events were used to determine the grid spacing to be used for this study. The soil types considered were site class B for the former and site class A for the latter, with the former transformed into site class A by dividing the amplification factors according to the National Earthquake Hazards Reduction Program (NEHRP) Seismic Provisions [49] applicable for short period responses.

Table 8 shows the details of the two ground motions used from the Engineering Strong Ground Motion [46]. For the L'Aquila earthquake, the PGA recorded at the seismogram with the epicenter at 4.9 km is $0.664g$ with site class B, which is multiplied by 0.8 to match the site class A as per the NEHRP Seismic Provisions. For the Central Italy earthquake, the PGA recorded at the seismogram

Table 7. Source-to-site distances obtained for the City of L'Aquila. The maximum distance is limited to 100 km

*TGR — Truncated Guttenburg-Richter, CHBPT — Characteristic Brown Passage Time

		Source-to-Site Distances (km)	
ID	**Source Name**	**Min**	**Max**
1	Barrea	88.14	105.67
2	Campo Felice Ovindoli	8.36	31.34
3	Carsoli	39.25	49.13
4	Cascia Cittareale	38.93	62.36
5	Cassino	97.25	123.75
6	Colfiorito	81.85	128.59
7	Fucino	25.32	59.05
8	GranSasso	8.32	41.12
9	Leonessa	46.32	63.19
10	Liri	40.03	68.07
11	Maiella	69.26	85.38
12	Marsicano	62.76	87.22
13	Middle Aternum Valley	18.83	48.49
14	Montereale	14.77	33.56
15	Mount Gorzano	12.57	42.25
16	Mount Vettore Mount Bove	45.25	79.64
17	Nottoria Preci	47.7	75.99
18	Paganica	1.64	21.36
19	Pizzalto C. Miglia	75.72	92.34
20	Pizzoli-Pettino	4.61	29.36
21	Rieti	47.8	66.17
22	Salto Valley	25.2	48.27
23	Sella di Corno	20.99	44.86
24	Sora	73.16	90.23
25	Sulmona	46.36	76.49
26	Umbrea Valley N	98.23	126.71
27	Umbrea Valley S	78.44	98.79
28	Velino	23.00	32.19

is $0.577g$ with the epicenter at 18.6 km. By trial and error, the appropriate grid spacings to be used are 24 and 19.8 m, say 20 m, for the sake of conservatism.

Using a uniform spacing of 20 m, the PGAs were estimated with different possible magnitude-distance pairs in each seismic source identified in this study. A total of 2013 simulations were performed across all seismic sources. Table 9 summarizes the PGA obtained in each seismic source.

Table 8. Attributes of the 2009 L'Aquila and 2016 Central Italy Earthquakes from the Engineering Strong Ground Motion [46]

Attributes	L'Aquila Event	Central Italy Event
Event ID	IT-2009-09	EMSC-20161030_0000029
Date	06042009	30102016
M_w	6.1	6.5
Station Code	4A.MI05	IT.ACC
Latitude	42.626	13.242
Longitude	42.28947	13.525526
PGA (g)	0.557	0.664
Soil Type	B	A

It follows from Table 9 that the minimum PGAs were observed in the Cassino and Umbrea Valley North segment faults with a value of $0.114g$, while the maximum was observed in the Paganica fault with a value of $2.160g$. These extreme values were expected to be in these seismic sources due to the combinations of the magnitude-distance for which they belong, and the model used to account for the recurrence of earthquakes in these sources. For Cassino and the Umbrea Valley North segment, the TGR model was used which considers a minimum magnitude of 5.5, and the distances of these faults from L'Aquila were 97.25 km and 98.23 km, respectively at the nearest, thus making the magnitude-distance pair of M_w 5.5, 100 km produce the minimum value in this study. For Paganica, the CHBPT model was used which utilized its maximum magnitude of 6.5 defined by this study plus one standard deviation of 0.2 while the nearest distance from the causative fault is 1.64 km, making the magnitude-distance pair produce the maximum value in this study.

12.1. Peak Ground Acceleration vs. Fault Length

The fault length affects the two parameters required for simulation of earthquakes, namely the maximum magnitude in each fault and the rupture time t_r. It is obvious from (83) that an increase in the fault length increases the maximum magnitude to be considered in a seismic source, and the moment magnitude is directly related to the seismic moment. The higher the fault length, the higher the seismic moment and so the higher the stress drop in a fault, which is directly related to the PGA. On the other hand, the rupture time, as defined in Subsection 3.2.1 of this paper, is directly proportional to the fault rupture length as well, which directly influences the variation in the stress drop in the fault as presented in the extended friction law model defined in this study. Table 10 shows the variation of some selected PGA values as a function of the fault length, considering (more or less) the same length of propagation (or distances) and the same magnitudes of occurrences.

In Table 10 it can be observed that the PGA does not vary that much across all the distances, and the variation is significant only up to the order of magnitude

Table 9. Predicted PGA in each seismic source

		Predicted PGA (in g's)	
ID	**Source Name**	**Min**	**Max**
1	Barrea	0.117	0.215
2	Campo Felice-Ovindoli	0.387	0.991
3	Carsoli	0.163	0.345
4	Cascia-Cittareale	0.143	0.373
5	Cassino	**0.114**	0.236
6	Colfiorito	0.115	0.244
7	Fucino	0.303	0.662
8	Gran Sasso	0.338	1.159
9	Leonessa	0.143	0.275
10	Liri	0.137	0.457
11	Maiella	0.123	0.280
12	Marsicano	0.213	0.336
13	Middle Aternum Valley	0.310	0.667
14	Montereale	0.280	0.651
15	Mount Gorzano	0.173	0.700
16	Mount Vettore-Mount Bove	0.242	0.497
17	Nottoria-Preci	0.122	0.342
18	Paganica	0.452	**2.160**
19	Pizzalto-Cinque Miglia	0.181	0.310
20	Pizzoli-Pettino	0.372	1.248
21	Rieti	0.199	0.362
22	Salto Valley	0.286	0.531
23	Sella di Corno	0.168	0.508
24	Sora	0.198	0.294
25	Sulmona	0.229	0.392
26	Umbrea Valley N	**0.114**	0.203
27	Umbrea Valley S	0.115	0.212
28	Velino	0.247	0.450

of 10^{-3} to 10^{-2}. As far as ocular observations are concerned, the values of PGA do not vary that much in relation to the fault length, and so regardless of the fault length, simulations of the fault rupture can be made to estimate the ground motion.

Given that the PGA does not vary that much in length of a fault rupture, one can simulate ground motions which can be used to determine the effect of site classes (soil type), epicentral and/or hypocentral distances, and grid spacing. These are not considered in this paper as they are beyond the scope of this study.

Table 10. Variation of PGA as a function of Fault Rupture Length. Each sub-table are grouped according to same magnitude of occurrence and more or less the same length of propagation. The fault length (L) is compared against the PGA given the distance and magintude.

L (km)	26.5	28.7	**L (km)**	21.5	23.7	**L (km)**	26.5	28.7
M/R	8.32	8.36	**M/R**	10.11	10.41	**M/R**	19.17	19.9
6.4	0.741	0.75	6.3	0.646	0.632	6.4	0.494	0.483
6.5	0.797	0.807	6.4	0.649	0.68	6.5	0.531	0.520
6.6	0.857	0.867	6.5	0.746	0.731	6.6	0.571	0.558
6.7	0.922	0.933	6.6	0.802	0.786	6.7	0.614	0.600
6.8	0.991	1.003	6.7	0.863	0.846	6.8	0.660	0.646

L (km)	21.5	23.7	**L (km)**	11.5	23.1	**L (km)**	11.5	23.1
M/R	21.11	21.362	**M/R**	23	23.64	**M/R**	26.06	26.29
6.3	0.434	0.452	5.8	0.291	0.288	5.8	26.06	26.29
6.4	0.467	0.485	5.9	0.313	0.31	5.9	0.274	0.273
6.5	0.502	0.522	6.0	0.336	0.333	6.0	0.294	0.293
6.6	0.540	0.561	6.1	0.362	0.358	6.1	0.316	0.315
6.7	0.581	0.603	6.2	0.389	0.385	6.2	0.375	0.364
			6.3	0.419	0.414	6.3	0.393	0.392
			6.4	0.450	0.445	6.4	0.423	0.421

13. Seismic Hazard Curves

Figure 22 shows the resulting seismic hazard curves for the city of L'Aquila which present the total hazard (topmost curve) and individual hazard curves contributed by each of the seismic sources identified in this study. This figure shows that Maiella, Mount Gorzano and Leonessa contributed the highest hazard rates in smaller values of PGA and Mount Vetorre — Mount Bove contributed the least. On the other hand, Campo Felice-Ovindoli, Pizzoli-Pettino, Fucino, Gran Sasso, and the Paganica Fault contributed the most hazard rates in higher values of PGA while other faults did not contribute to the hazard rates of higher PGA. Specifically, it was only the Paganica Fault that contributed to the hazard in L'Aquila in PGA values greater than $1.30g$. Higher hazard values for smaller values of PGA are evident to seismic sources which are modeled with the TGR recurrence model and those that are very far from L'Aquila. It has been mentioned before that Maiella has the highest rates, and hence contributes to the seismic hazard at small values of PGA. The Paganica Fault, the closest fault in L'Aquila, has very small hazard rates but produces the highest PGA values due to the small distance — high magnitude combinations.

The resulting hazard curve has an abrupt change in the slope at PGA equal to $0.70g$ as shown in Figure 22. This can be attributed to a decrease in the number

Table 11. Table 10 — continued

L (km)	26.5	28.7	**L (km)**	34	22.6	42.5
M/R	31.34	31.47	**M/R**	52.89	53.05	53.22
6.4	0.387	0.384	6.3	0.298	0.295	0.300
6.5	0.417	0.413	6.4	0.321	0.317	0.319
6.6	0.448	0.444	6.5	0.345	0.341	0.343
6.7	0.482	0.478	6.6	0.371	0.366	0.369
6.8	0.518	0.514				

L (km)	22.6	42.5	34
M/R	59.75	59.82	60.54
6.4	0.278	0.282	0.278
6.5	0.299	0.300	0.299
6.6	0.321	0.322	0.322
6.7	0.345	0.347	0.346

L (km)	17.4	24.6	28.6	45
M/R	100	100	100	100
5.5	0.127	0.115	0.114	0.115
5.6	0.129	0.121	0.121	0.124
5.7	0.136	0.131	0.131	0.133
5.8	0.147	0.140	0.140	0.143
5.9	0.155	0.151	0.151	0.154
6.0	0.162	0.162	0.162	0.165
6.1	0.174	0.174	0.174	0.178
6.2	0.187	0.187	0.187	0.191

L (km)	18	24	24	18	24	18
M/R	80.7	81.26	84.95	85.23	92.01	92.34
6.1	0.194	0.193	0.189	0.189	0.182	0.181
6.2	0.208	0.208	0.203	0.203	0.195	0.195

of the seismic sources that contribute only to the small value of PGA. In fact, only the five seismic sources mentioned above which contributed greatly to the seismic hazard corresponding to higher values of PGA, say above $0.70g$, comprise that portion of the seismic hazard curve where the slope changes abruptly. Lastly, the curve changed abruptly again at a PGA value of $1.30g$, for it is attributed solely due to the Paganica Fault.

Figure 23 shows a comparison of the hazard curve in this study with the work of Valentini et al. [24]. It follows from the figure that the hazard curve

produced in this study is higher than the hazard curve in Valentini et al. [24], which can be attributed to the higher values of PGA that are simulated by solving the elastodynamic equation. On the other hand, the hazard curve of Valentini et al. [24] is higher than that the hazard curve of this study, which can be attributed to the smaller number of seismic sources considered in this study. The hazard curve of Valentini et al. [24] considered both fault sources and distributed sources, and therefore this study can be further improved by considering the distributed sources as well. For the portion of the hazard curve which is higher than that of Valentini et al. [24], the grid spacing used in the simulation can be varied depending on the distance from the fault. Also, the fault parameters in relation to the PGA prediction can be calibrated using other soil types and other ground motion data available in the Engineering Strong Motion Database.

14. Application of PSHA to Seismic Design

This hazard curve can be used to determine the feasible ground motion properties that a future earthquake can produce in terms of its return period. With the given mean annual rate of exceedance, one can obtain the return period using its reciprocal. As mentioned before in Subsection 5.1.1, the seismic design of structures requires a minimum value of PGA with a probability of exceedance of 10% in 50 years of the exposure time, and this corresponds to a return period of 475 years or 0.00202 earthquakes per year. Also, for a higher hazard consideration, a PGA value having a probability of exceedance of 2% can be used, which has a return period of 2475 years or a hazard rate of 4.04E-04. Interpolating these values from the constructed hazard curve in Figure 5.1 enables an engineer to construct the elastic design spectrum. Figure 24 shows the PGA values corresponding to 10% and 2% probability of exceedances in 50 years' exposure time, and Figure 5.4 shows the elastic design spectra corresponding to the probability of exceedances.

15. Summary and Conclusion

A non-ergodic probabilistic seismic hazard analysis (PSHA) was carried out in the study area of the city of L'Aquila, Italy due to its proximity to several active faults in Central Italy and past seismicity leading to catastrophic damage in the city brought by the 2009 L'Aquila earthquake. This non-ergodic approach was taken by solving the Elastodynamic Equation coupled with the Hooke's Law, both of which form a system of Hyperbolic equations, which is another form of the Elastic Wave Equation.

A total of 28 seismic sources were identified in this study located within a 100 km radius from the city, and a map was produced to show all the seismic sources using ArcGIS. To characterize the variation in source-to-site distances, each seismic source was subdivided into 100 equal areas, and the centroids of each resulting areas were calculated using ArcGIS, after which the histograms with 10 bins each were created to be used for the probability of the exceedance calculations. Each of the seismic sources was characterized by its fault geometric

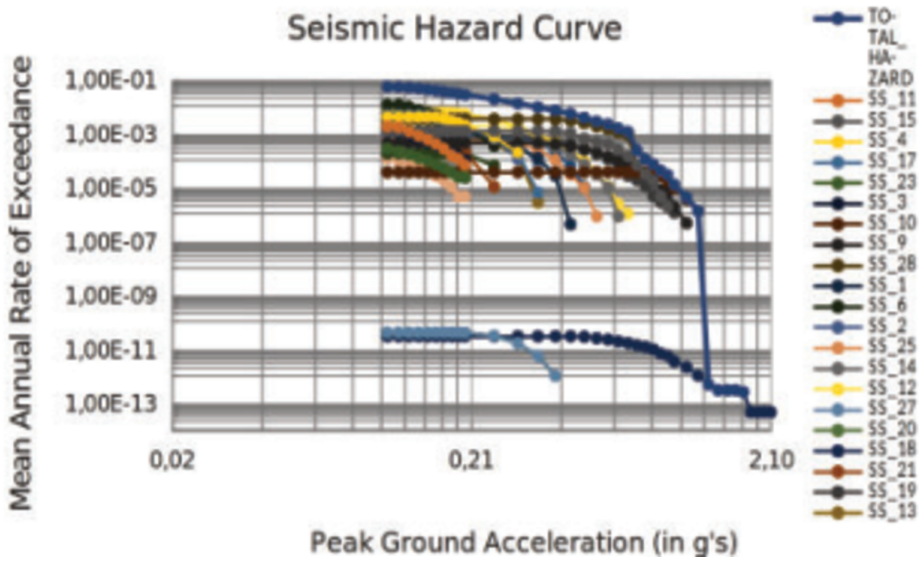

Figure 22. Seismic Hazard Curve for the City of L'Aquila, Italy

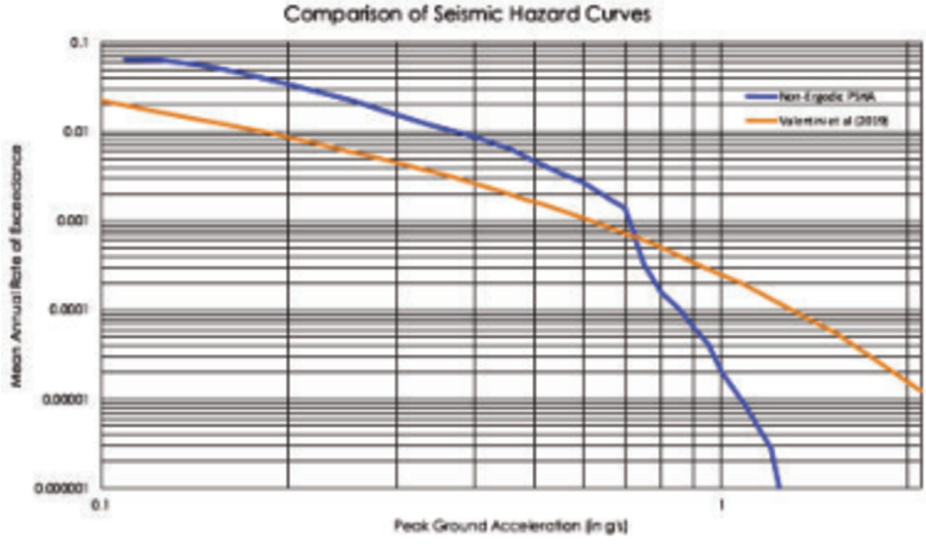

Figure 23. Comparison of the hazard curve in this study with the hazard curve of Valentini et al. [24]

properties such as length, dip, slip rates, seismogenic thickness, the observed magnitude of occurrence, and the last year of occurrence, all of which were obtained from Valentini et al. [25] and Valentini et al. [24]. To model the recurrence of earthquakes in each source, past seismicity in the form of the paleoseismic activity and historical earthquakes was extracted from Valentini et al. [24] as well, and the activity rates were calculated using the FiSH Code by Pace, Visini,

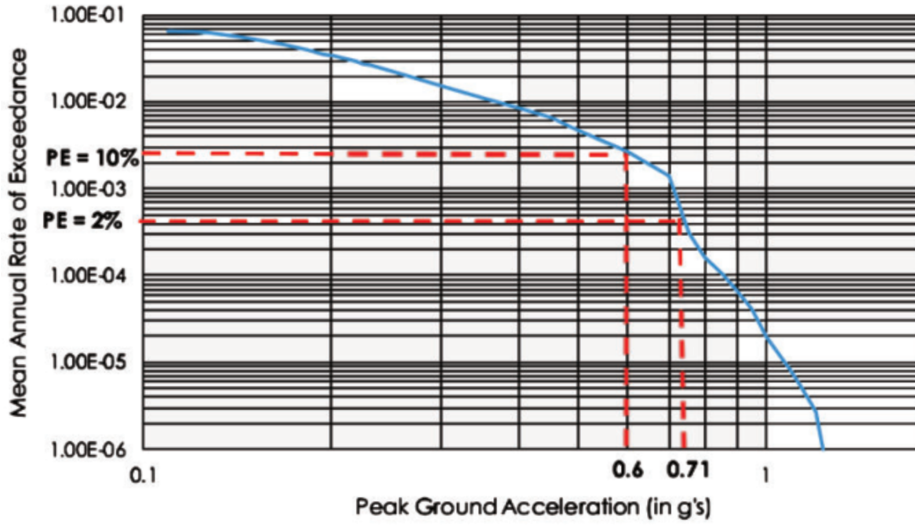

Figure 24. PGA values corresponding to 10% and 2% probability of exceedances

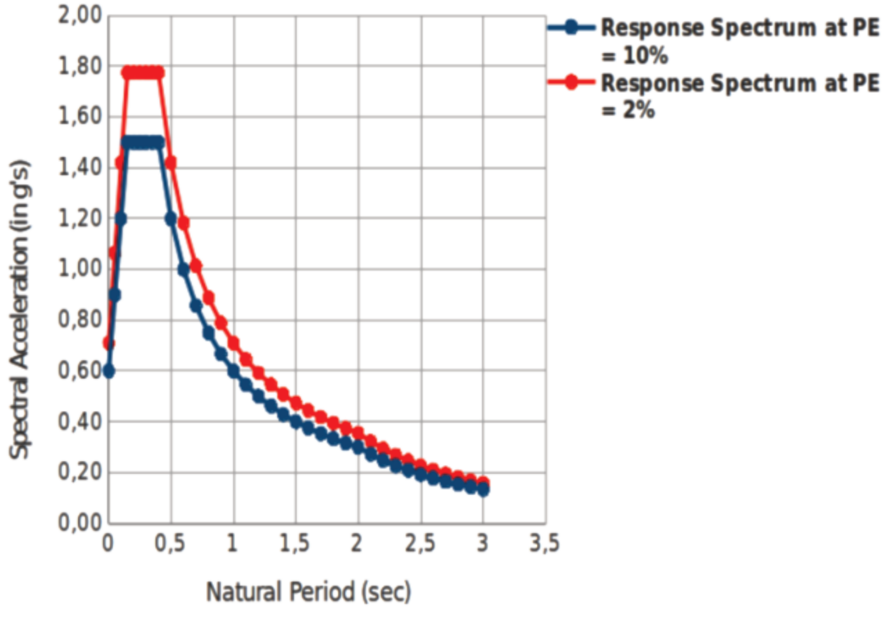

Figure 25. Elastic Design Spectrum corresponding to 10% and 2% probability of exceedances

and Peruzza [41]. The maximum magnitude was calculated in each fault by the criteria set forth in Subsection 5.1. Two recurrence models were employed in this study; the Truncated Guttenberg-Richter (TGR) and Characteristic Brownian Passage Time (CHBPT) models, as set forth by Subsection 5.1.1.

After the data had been extracted from Valentini et al. [25] and Valentini et al. [24], the seismic moments, fracture energy, stress drop were computed using a set of empirical equations from Causse et al. [31]. Then, a physics-based ground motion prediction by solving the Elastodynamic Equation and the Hooke's Law was employed by applying the extended friction law model as a boundary condition for pressure in each fault, and synthetic seismograms were produced in all the distances calculated in ArcGIS and the magnitude of occurrences in each fault source. The grid spacing was chosen by considering the actual ground motions obtained from the 2009 L'Aquila and 2016 Central Italy earthquakes. The earth is modeled as a 1-D model which is according to the PREM Model, for which the density and the S-wave velocity was obtained considering the seismogenic thickness of each fault. The peak ground accelerations (PGA) in each seismogram were obtained, and histograms of PGA were created in terms of frequency of distances to calculate the probability of exceedance of a PGA value given a reference PGA. Lastly, the hazard curve was calculated using the formulation by Tarbali et al. [19, 20]. The resulting hazard curve was compared to the hazard curve of Valentini et al. [24].

Based on the activity rates obtained, Maiella has the highest value which turns out to be one of the highest contributors to the overall seismic hazard considering the lower values of PGA, while Mount Vetorre — Mount Bevo has the lowest activity, followed by the Paganica Fault. In terms of proximity to the city of L'Aquila, Paganica is the nearest, while Umbrea Valley North Segment and Colfiorito are the farthest. The highest PGA values were obtained from Paganica due to its proximity to the fault and the high magnitude of occurrence, while the Umbrea Valley North Segment and Cassino produced the lowest PGA of all. Higher values of PGA resulted from the CHBPT recurrence model and proximity to the fault sources, while lower values of PGA resulted from the TGR recurrence model and longer lengths of wave propagations.

The PGA values did not vary too much considering the fault rupture length, which in turn is directly related to the rupture time, and therefore, a simulation of ground motions can be performed to determine the effect of site classes, epicentral or hypocentral distances, and grid spacing.

Maiella, Mount Gorzano, and Leonessa contributed the highest hazard rates in smaller values of PGA and Mount Vetore — Mount Bove contributed the least. On the other hand, the Campo Felice-Ovindoli, Pizzoli-Pettino, Fucino, Gran Sasso and Paganica Faults contributed the most hazard rates in higher values of PGA while other faults did not contribute to the hazard rates of higher PGA. The seismic hazard curve produced in this study is higher than that of Valentini et al. [24] for a PGA smaller than or equal to $0.70g$, while the opposite is true for PGA greater than $0.70g$. This can be attributed to the overestimation of PGA at larger distances, and thus can be resolved by varying the grid spacing given a certain length of propagation in order to decrease the hazard rate at lower values of PGA. On the other hand, to increase the hazard rates at higher PGA values,

it is recommended to include distributed sources in the seismic hazard analysis. Also, other parameters regarding the fault rupture can be calibrated using the actual ground motion data considering longer source-to-site distances.

As application to the seismic design, the PGA values corresponding to 10% and 2% probability of exceedance were obtained from the resulting hazard curve of this study, and the elastic design spectra considering these two probabilities of exceedances were constructed and can be readily used.

16. Recommendations

The researcher believes that the fault data and the past seismicity used in this study are robust, nonetheless, they still can be improved by updating the earthquake catalogue including the past seismicity in the case of new occurrences. Also, the available S-wave velocity and the rock density profile can be used to improve the estimation of the ground motion, instead of using constant values of S-wave velocity and density.

When it comes to the numerical simulation of earthquakes using the Finite Difference Method, different grid spacings must be employed by studying the appropriate grid spacing given a range of values of the length of propagation and the site class type, which depend on the shear wave velocity of the soil, since accelerometers were located on the surface of the soil and not on the bedrock. Also, the extended friction law can be improved by calibrating the initial dynamic stress value against the actual ground motion data. Another possibility is to incorporate the seismogenic thickness to consider the hypocentral distances instead of epicentral distances; this also opens a possibility of exploring the actual stresses in the fault as long as data regarding the unit weight and the presence of a water table and other factors affecting effective stresses can be obtained to improve the values used in the extended friction law. With the improvement of the seismic parameters to be used to simulate an earthquake, a 2D or even 3D Elastodynamic Equation can be used to predict the PGA on a site.

To improve the seismic hazard curve, distributed sources must be studied as well and incorporated into the seismic hazard to improve the hazard rates in PGA higher values. Also, a hybrid of hazard rates can be considered by contemplating a certain grid spacing for a certain distance, thus employing different grid spacings to avoid overestimation in the PGA.

As for other numerical methods to simulate earthquakes, the Finite Element Method is also a well-known method to solve the elastodynamic equation, which can be a better approximation than the Finite Differences. The use of Green Functions, a widely used method to produce synthetic seismograms, can also be utilized to estimate the PGA.

Acknowledgment

The main author would like to thank the University of the Philippines System through the Office of the Vice-President of Academic Affairs and the Uni-

versity of the Philippines Los Baños through the Office of the Vice-Chancellor of Academic Affairs and the Department of Civil Engineering for all the administrative and financial support received from them to make this study possible. Also, a special mention to INGV L'Aquila and Dr. Francesco Visini for the data used in this study.

Appendices

Appendix A. Derivation of Seismic Hazard Rate

In the PSHA Methodology, we can treat y as a reference ground motion parameter, say the PGA, which depends mainly on distance R M, which are assumed to be independent of each other. Since magnitude occurrences are treated as rupture scenarios, the conditional exceedance probability in (98) is treated as the relative proportion of distances whose PGA exceeds that of the reference PGA, given the magnitude of the occurrence. Hence, given the uncertainty in the magnitude, the probability of exceedance for a single seismic source is given by

$$P(Y > y \cap M) = \int P[Y > y|M] f_M(m)\, dm, \tag{98}$$

where

$$P[Y > y|M] = \frac{N\left[R_{Y>y}\right]}{N_R}$$

For brevity, we rewrite (98) as

$$P(Y > y) = \int P[Y > y|M] f_M(m)\, dm. \tag{99}$$

Given N seismic sources (assuming) independent of each other and collectively exhaustive, we apply the Total Probability Theorem for the entire study area:

$$P(Y > y) = \sum_{i=1}^{N} \int P[Y > y|M]_i f_{M_i}(m)\, dm, \tag{100}$$

Evaluating the integral in (100) numerically, one obtains the probability mass function of the magnitude random variable

$$P(Y > y) = \sum_{i=1}^{N} \sum_{j=1}^{N_M} P[Y > y|M]_i P\left(M = m_j\right)_i, \tag{101}$$

where N_M is the number of magnitude occurrences in a seismic source. The product of the activity rate and the probability of occurrence at a given magnitude is the hazard rate of the rupture scenario. For brevity, considering all kinds of rupture scenarios in the study area regardless of the seismic source a rupture scenario due to the assumption in (100), (102) becomes the expression in (6)

$$\lambda_{IM}(im) = \sum_{n=1}^{N_{rup}} P[Y > y|rup_n]\, \lambda_{Rup}(rup_n). \tag{102}$$

Appendix B. Distance Probability Mass Functions

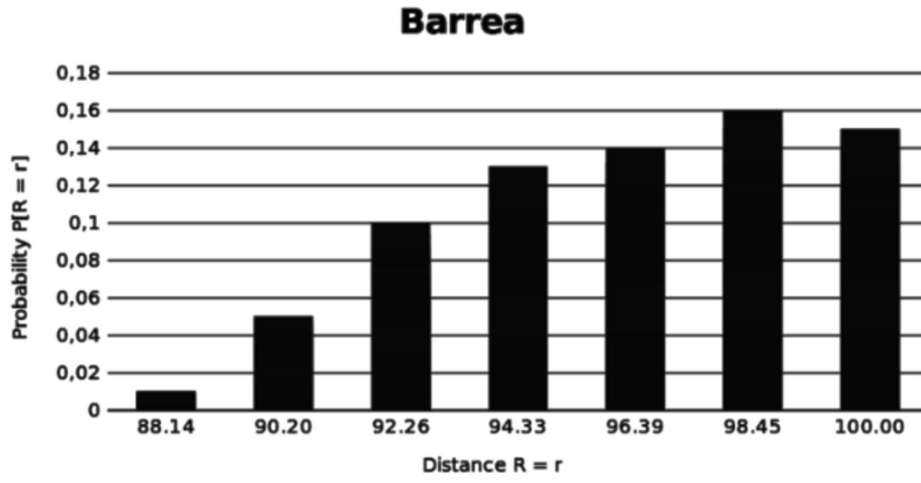

Figure 26. Distance Probability Mass Function for Barrea Fault

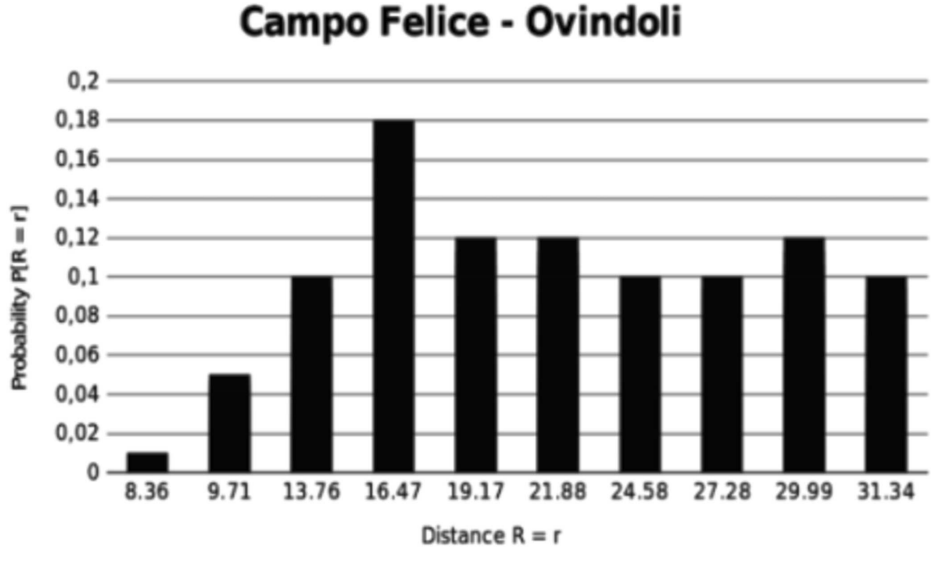

Figure 27. Distance Probability Mass Function for Campo Felice-Ovindoli Fault

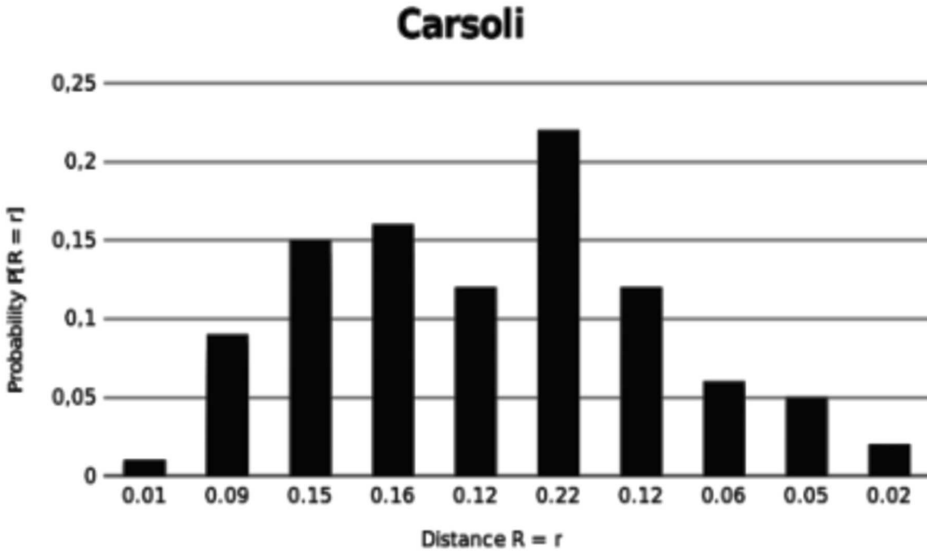

Figure 28. Distance Probability Mass Function for Carsoli Fault

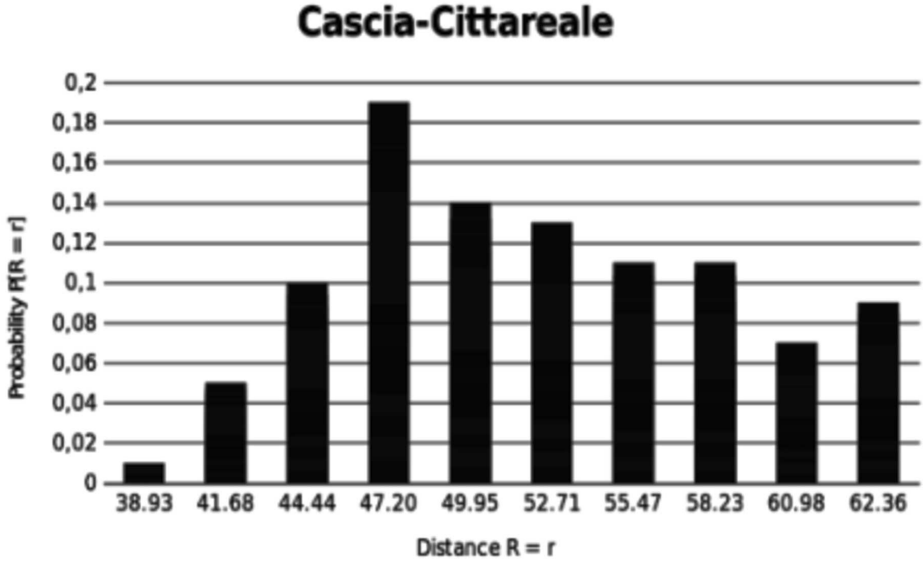

Figure 29. Distance Probability Mass Function for Cascia-Cittareale Fault

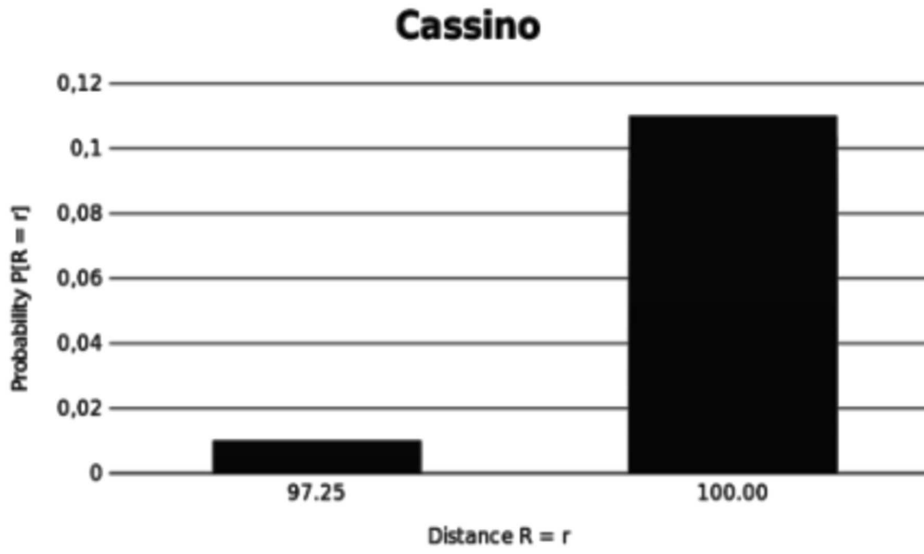

Figure 30. Distance Probability Mass Function for Cassino Fault

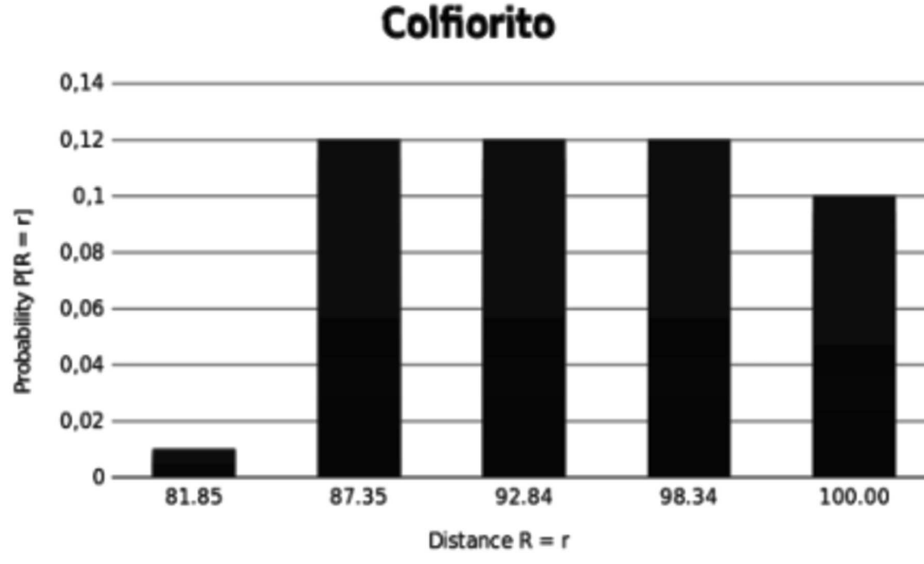

Figure 31. Distance Probability Mass Function for Colfiorito Fault

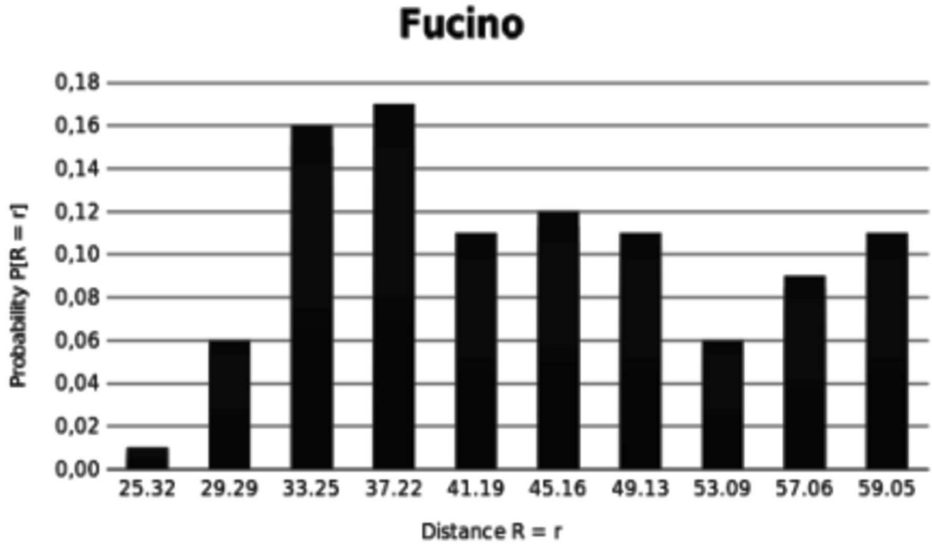

Figure 32. Distance Probability Mass Function for Fucino Fault

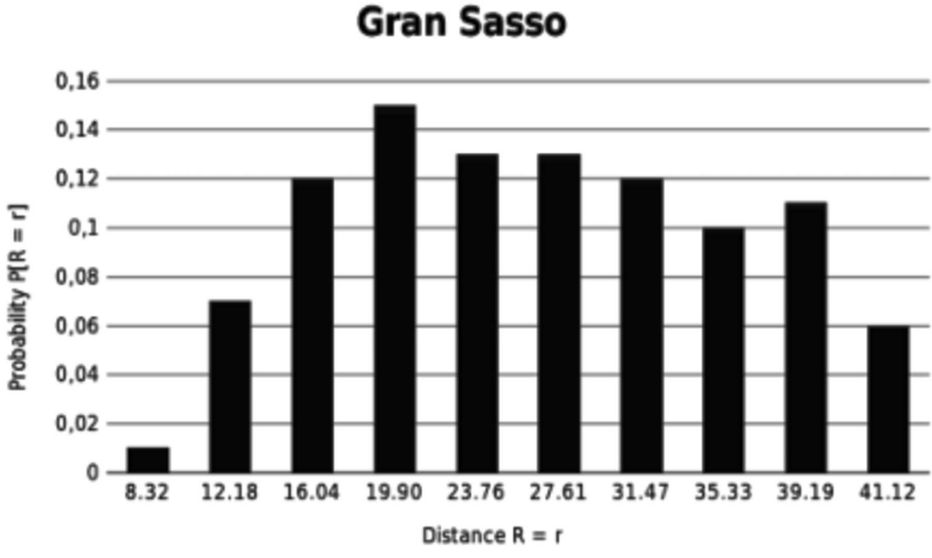

Figure 33. Distance Probability Mass Function for Gran Sasso Fault

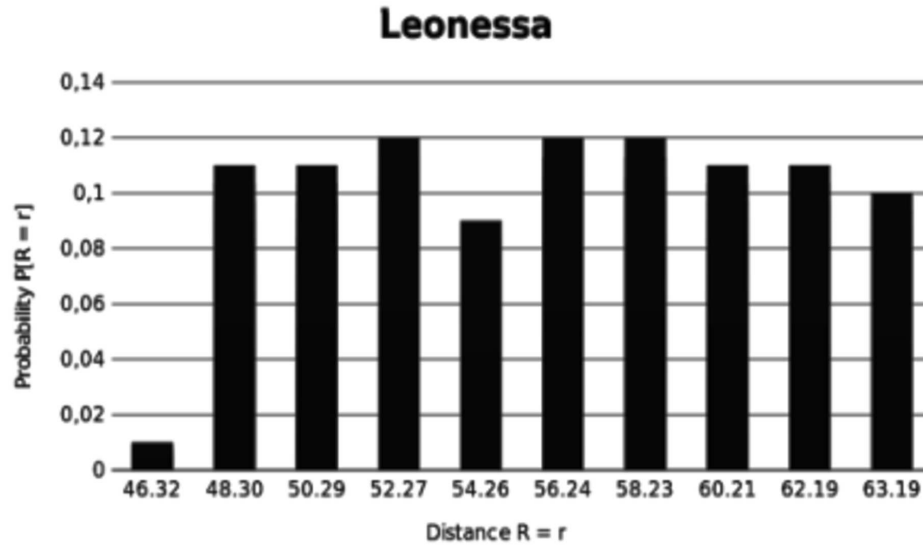

Figure 34. Distance Probability Mass Function for Leonessa Fault

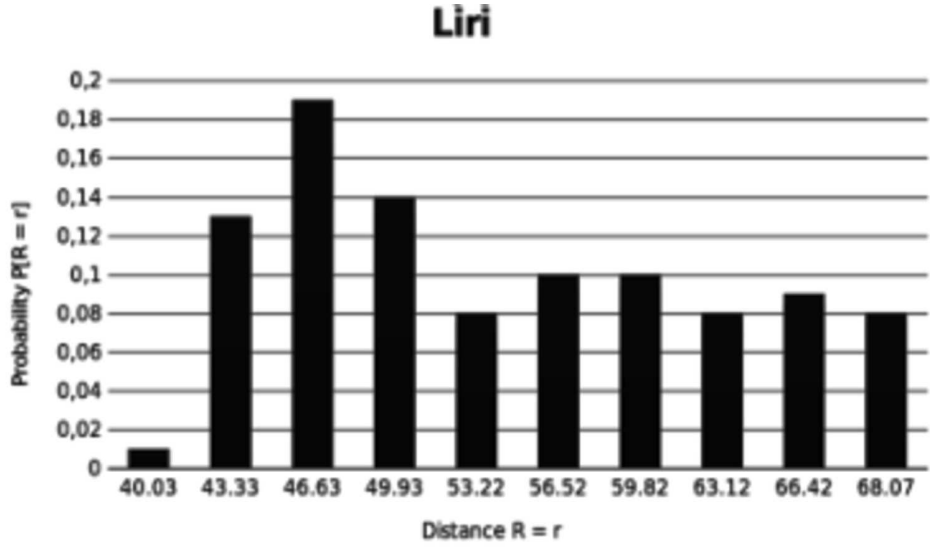

Figure 35. Distance Probability Mass Function for Liri Fault

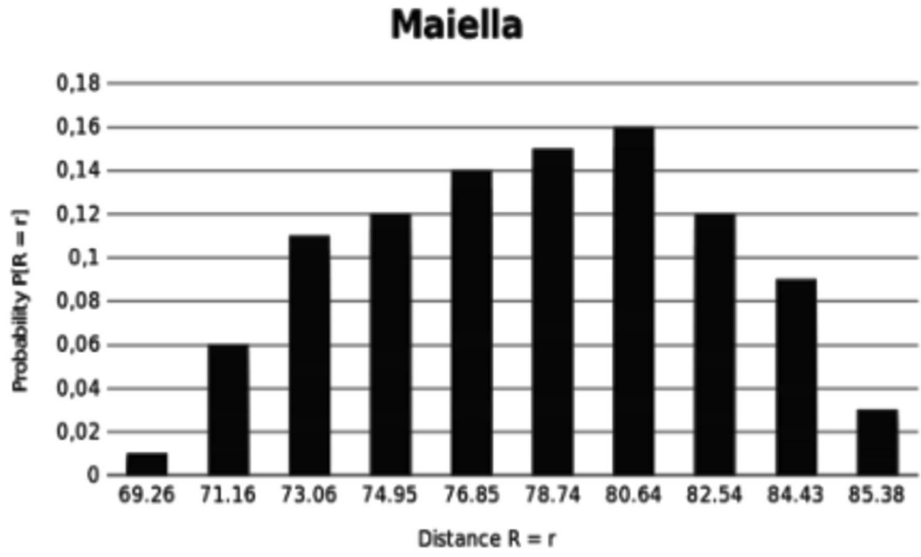

Figure 36. Distance Probability Mass Function for Maiella Fault

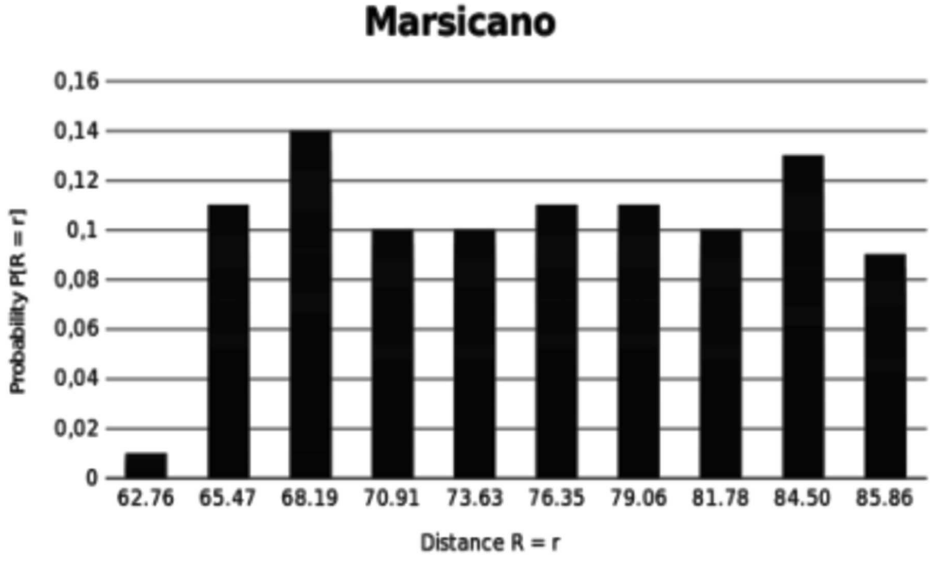

Figure 37. Distance Probability Mass Function for Marsicano Fault

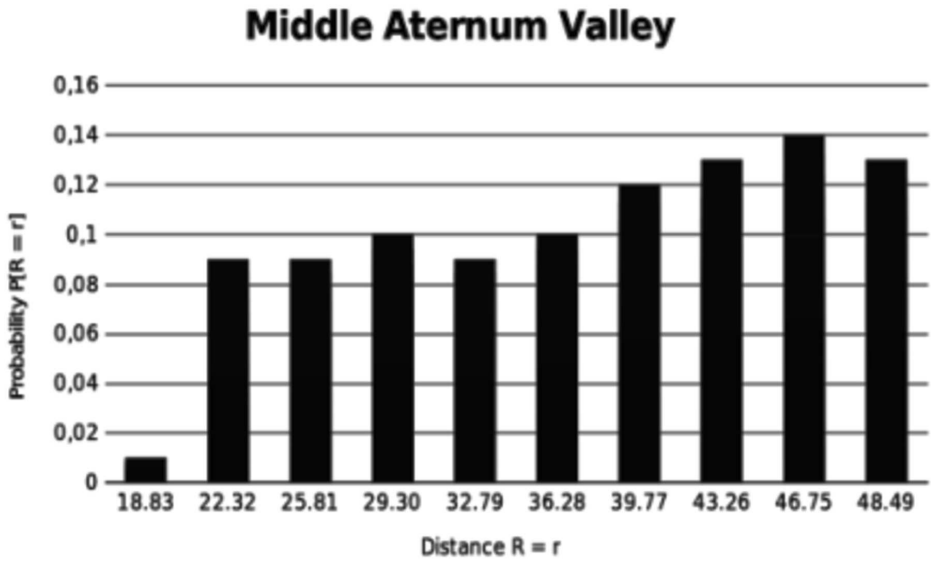

Figure 38. Distance Probability Mass Function for Middle Aternum Valley Fault

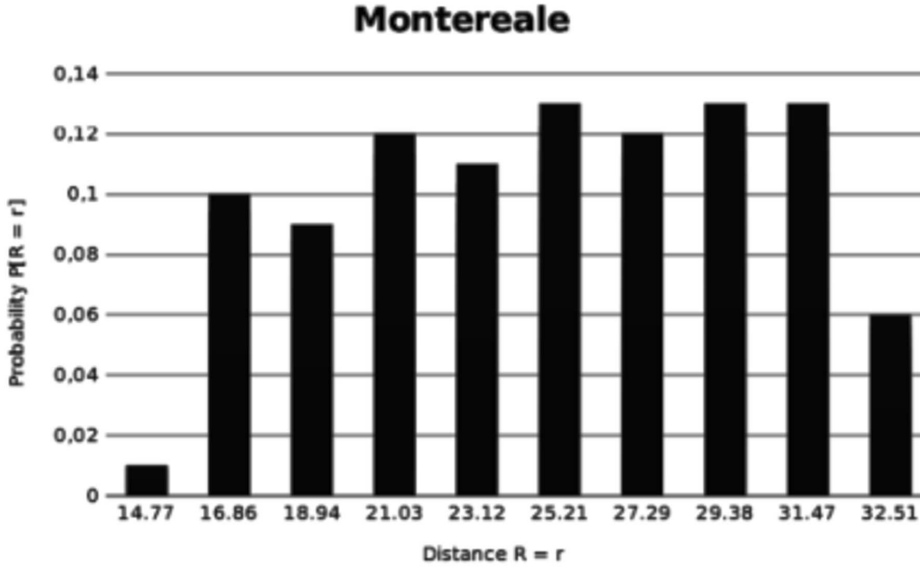

Figure 39. Distance Probability Mass Function for Montereale Fault

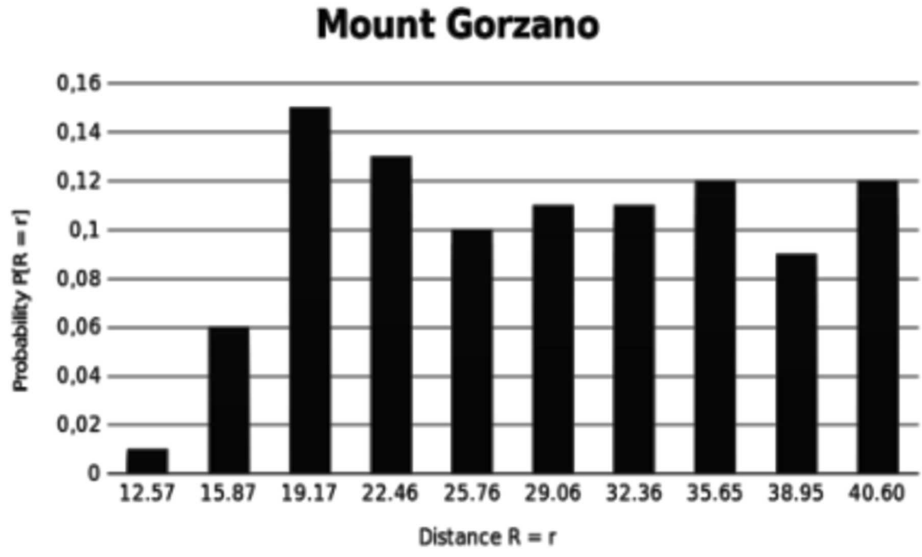

Figure 40. Distance Probability Mass Function for Mount Gorzano Fault

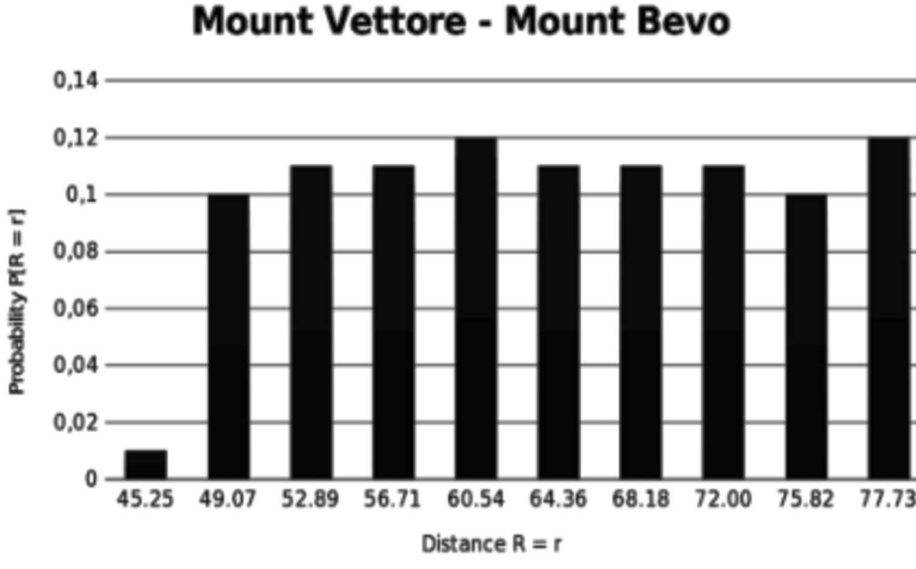

Figure 41. Distance Probability Mass Function for Mount Vettore — Mount Bevo

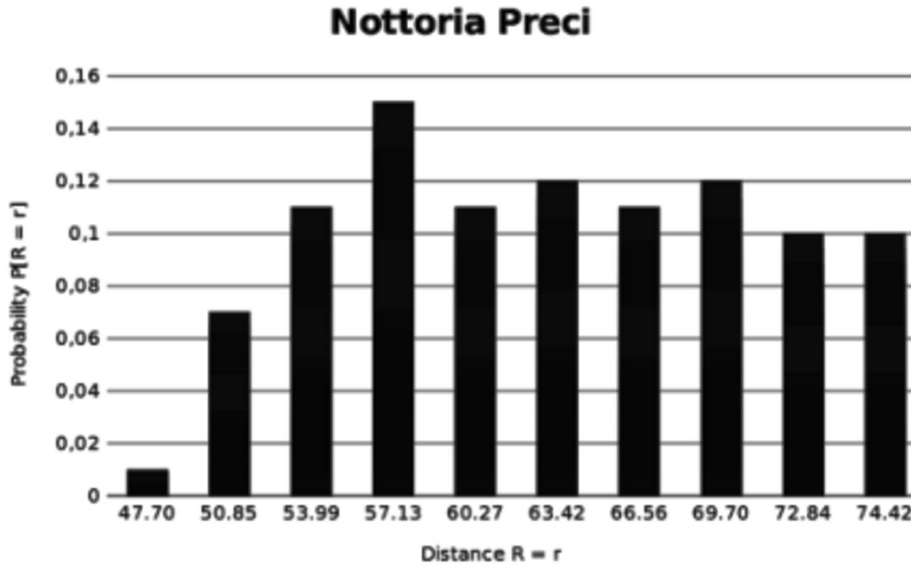

Figure 42. Distance Probability Mass Function for Nottoria Preci Fault

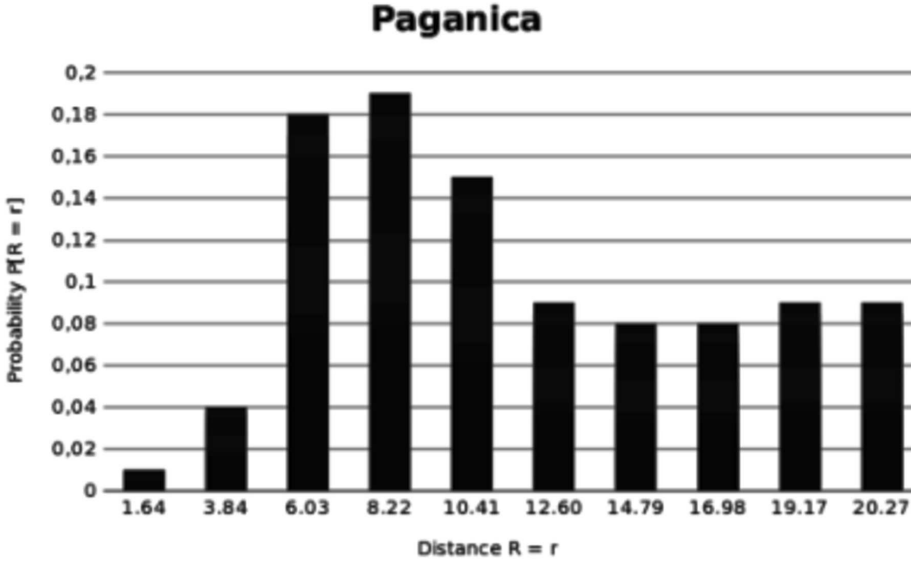

Figure 43. Distance Probability Mass Function for Paganica Fault

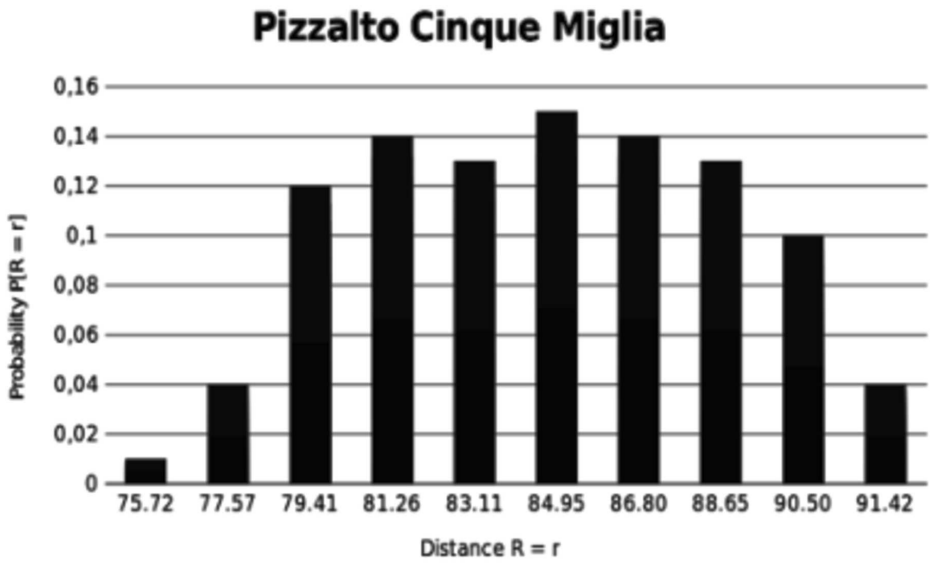

Figure 44. Distance Probability Mass Function for Pizzalto Cinque Miglia Fault

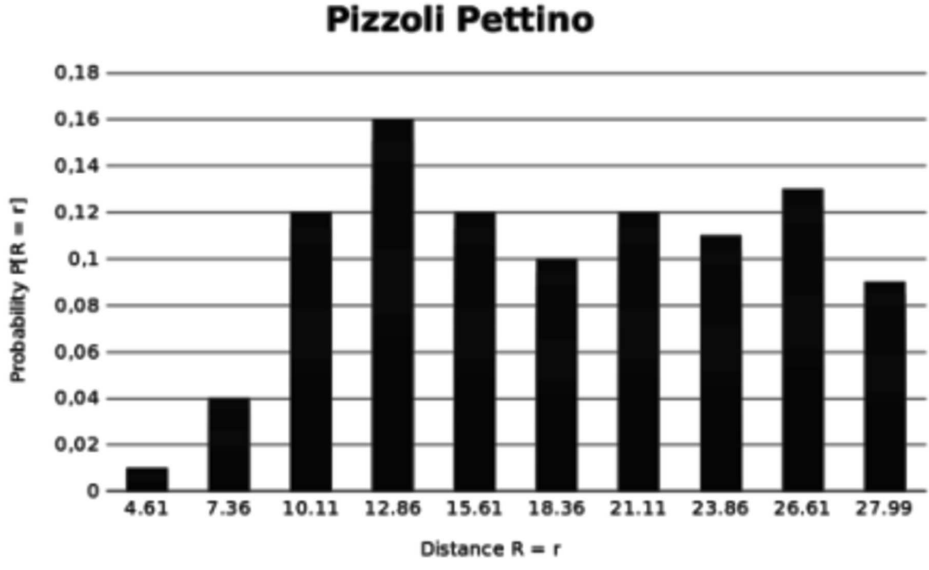

Figure 45. Distance Probability Mass Function for Pizzoli-Pettino Fault

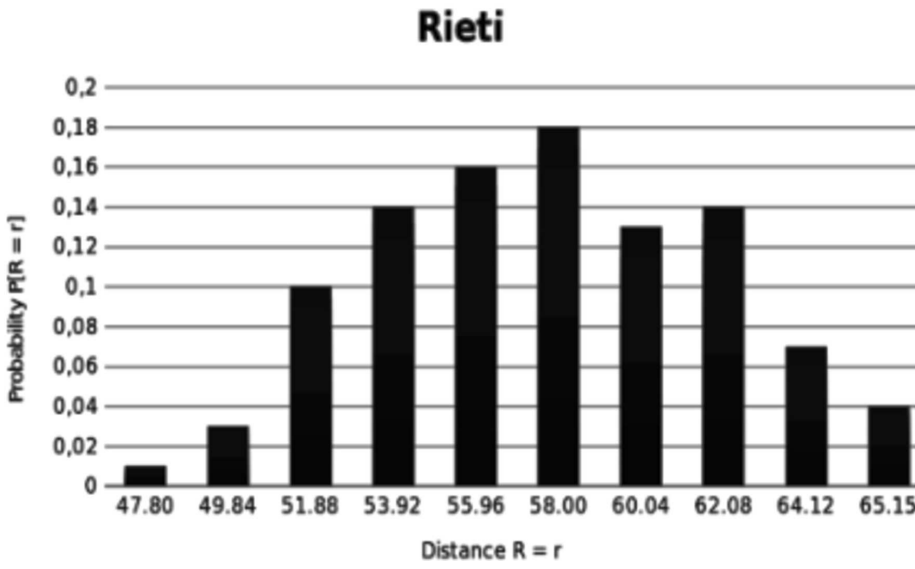

Figure 46. Distance Probability Mass Function for Rieti Fault

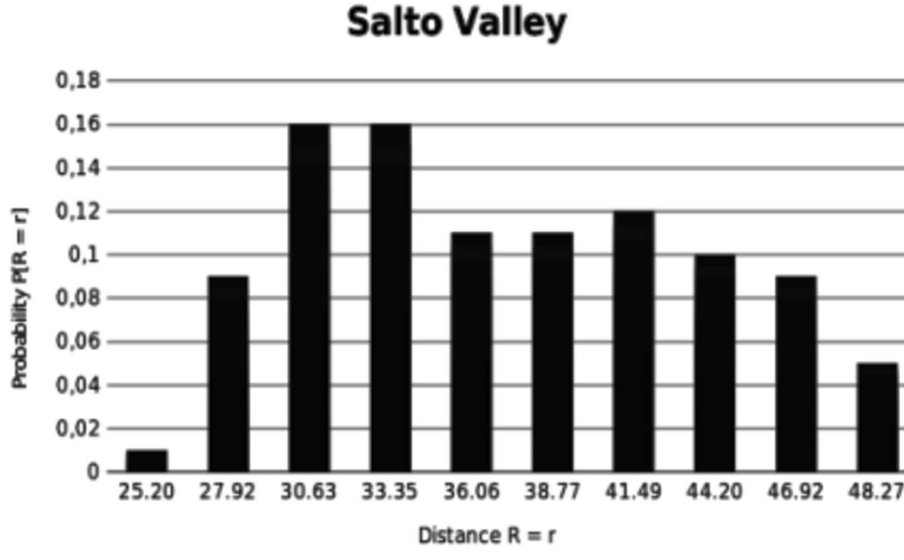

Figure 47. Distance Probability Mass Function for Salto Valley Fault

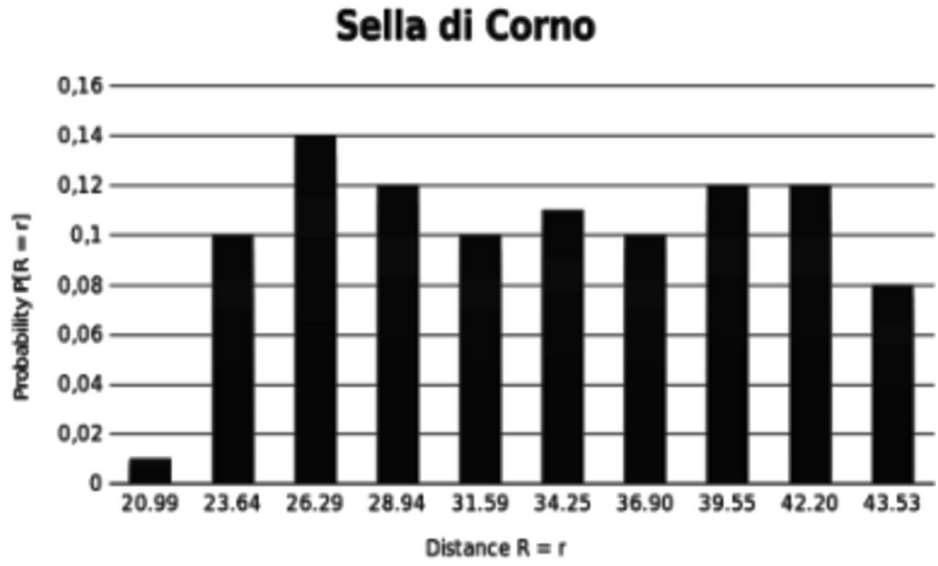

Figure 48. Distance Probability Mass Function for Sella di Corno Fault

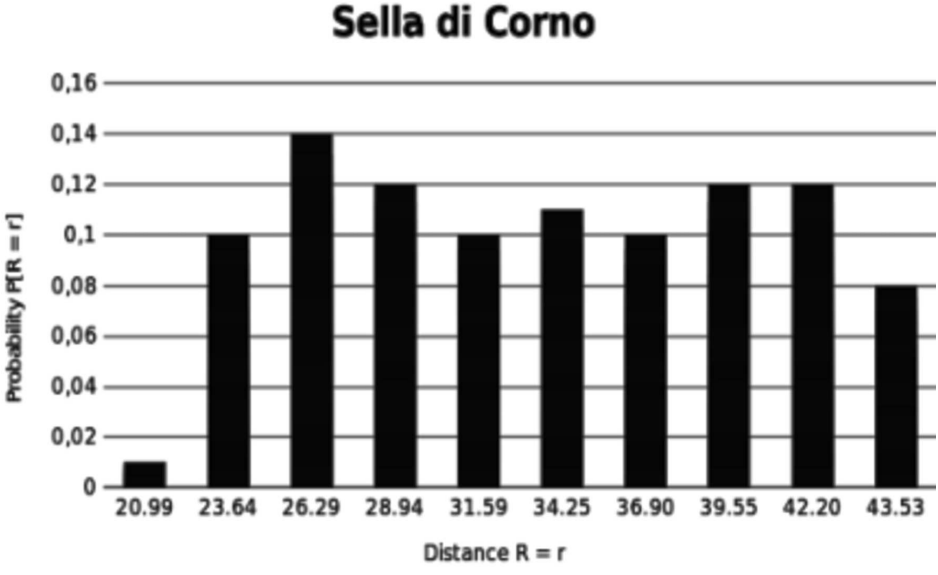

Figure 49. Distance Probability Mass Function for Sora Fault

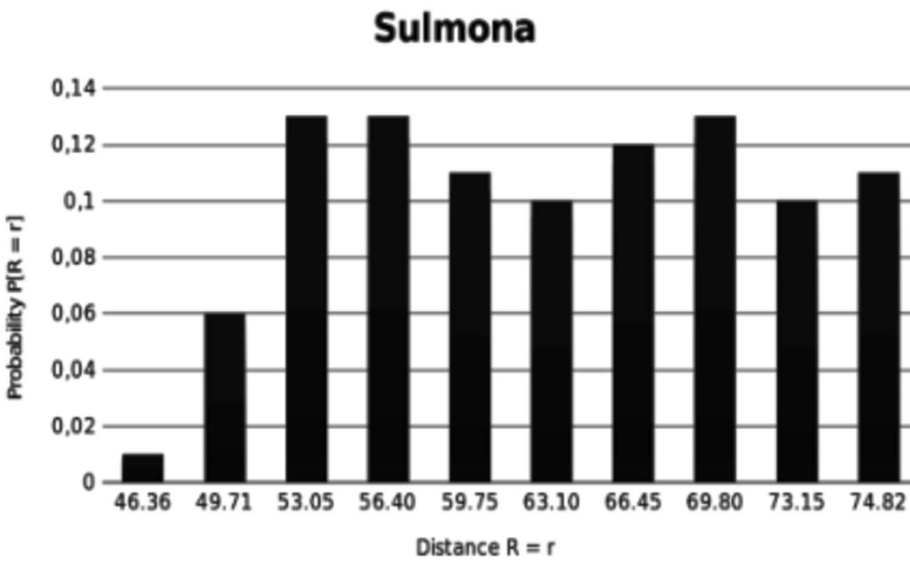

Figure 50. Distance Probability Mass Function for Sulmona Fault

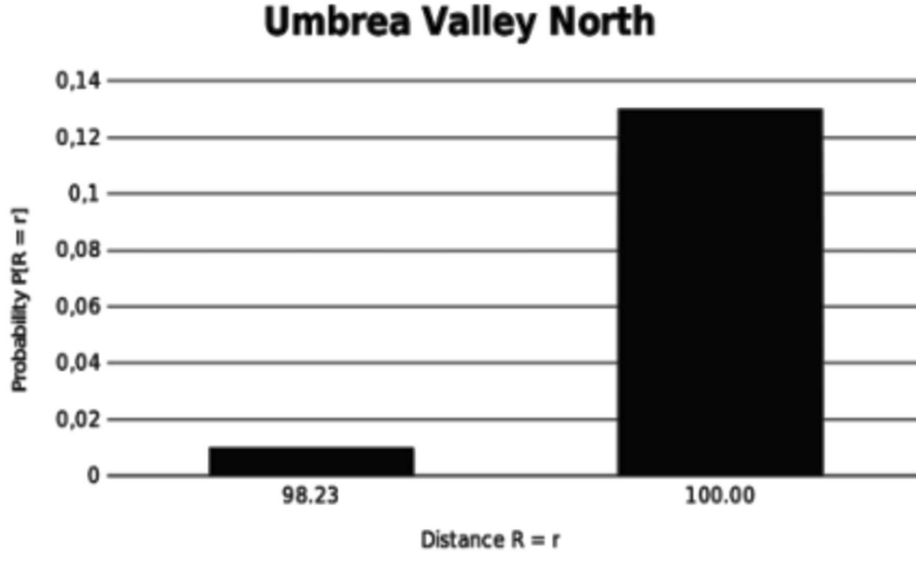

Figure 51. Distance Probability Mass Function for Umbrea Valley Fault North Segment

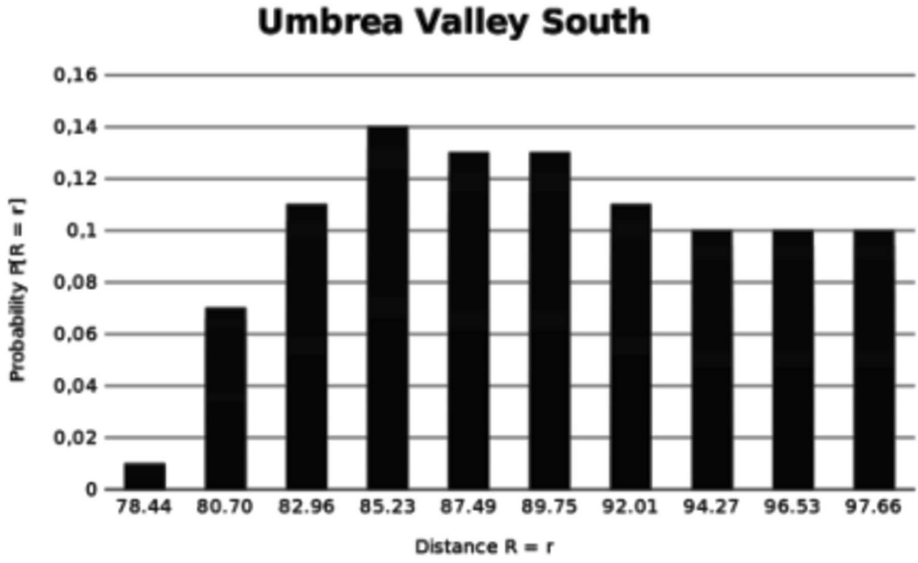

Figure 52. Distance Probability Mass Function for Umbrea Valley Fault South Segment

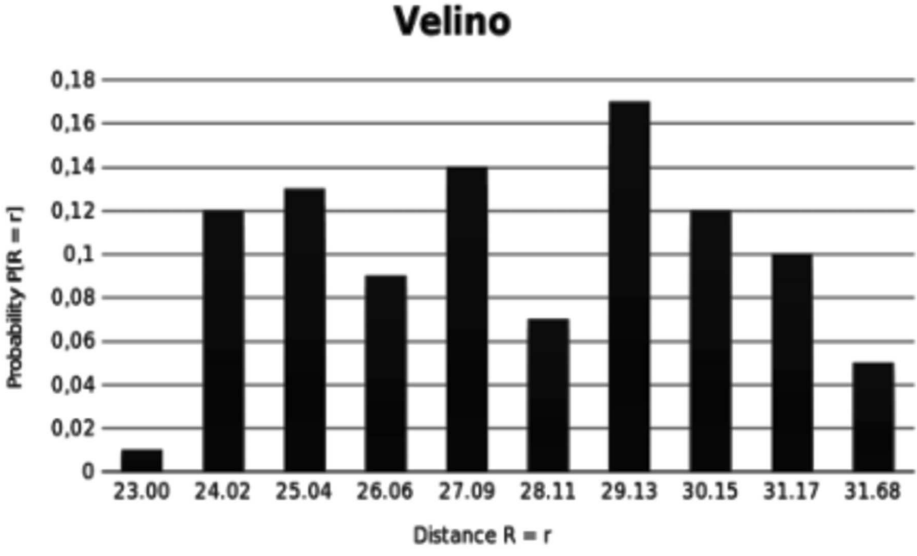

Figure 53. Distance Probability Mass Function for Velino Fault

Appendix C. MATLAB Script for Solving the One-Dimensional Elastodynamic Equation and Hooke's Law

```
% Author: Jedidiah Joel Aguirre 2019
%
% Finite-Difference seismic wave simulation
% Discretization of the first-order elastic wave equation
%
% Temporal second-order accuracy O(DT^2)
% Spatial second-order accuracy  O(DX^2)

%% Initialization
disp(' ');
disp(['Starting ', mfilename ]);
close all; clearvars;
    addpath functions

%% Parameters

%Boundary Condition Parameters
tau_one=0; %Dynamic Stress in the fault (in MPa)
tau_zero=tau_one+4.4; %Maximum Static Stress (in MPa)
t1 = .295; % characteristic time from friction law
%Crust Parameters
beta = 3200; %S-wave speed in m/sec
rho = 2600; %density of rocks in kg/m^3
mu = rho*beta^2/1e6; %lame constant

%Fault Rupture Parameters
L = 11; %fault length in km
vr = 0.9*beta; %rupture velocity in m/sec
tr = round(0.5*L*1000/vr,2); %rupture time

%Discretization Parameters and Vector Assignments
L_p = 100+.2; %prop length in km
T = round(1000*L_p/beta,2); %time of arrival in the site
tf = T+10;  % duration of seismogram
dx = 200;   % meters in spacing
dt = 0.005; %time interval for typical seismograms
x = 0:dx:L_p*1000; % x vector
J = numel(x); % no. of grids
t = 0:dt:tf+dt; % time vector
nt = numel(t);% no. of time steps

% Preallocate space
p = zeros(nt,J);    % pressure matrix
v = zeros(nt,J); % velocity matrix

%Initial conditions
for i=2:J
    p(1,i)=0;  %zero pressure
    v(1,i)=0;  %zero velocity
end

%Boundary conditions
for i = 1:nt
    v(i,1) = 0; %zero velocity
    [p(i,1)] = tau(dt*i,tr,t1,tau_one,tau_zero); %friction law at the boundary
end
```

```
%update velocity and pressure
for n=2:nt;
    for kx = 1:J-1
         % Calculating spatial derivative
            p_x=(p(n-1,kx+1)-p(n-1,kx))/dx;

            % Update velocity
            v(n-1,1)=0;
            v(n,kx)=v(n-1,kx)+(dt/rho)*p_x*1e6;
    end

    % Update pressure
    for kx=2:J;

            % Calculating spatial derivative
            vx_x=(v(n,kx)-v(n,kx-1))/dx;

            % Update pressure
            p(n,kx)=p(n-1,kx)+mu*dt*(vx_x);

    end
end


a = diff(v(:,J-1))./diff(t')/9.81;
acc_max = max(max(a),abs(min(a)));
disp(['PGA = ',num2str(acc_max),'g'])
```

References

[1] Kramer S L 1996 *Geotechnical earthquake engineering*, Prentice-Hall Inc, New Jersey 1

[2] Kramer S L and Scawthorn C 2000 *Geotechnical earthquake considerations*, *Bridge Engineering Handbook*, Wai-Fah Chen and Lian Duan. Boca Raton: CRC Press, **132**

[3] Monaco P, Totani G, Barla G, Cavallaro A, Costanzo A, D'Onofrio A, Evangelista L, Foti S, Grasso S, Lanzo G, Madiai C, Maraschini M, Marchetti S, Maugeri M, Pagliaroli A, Pallara O, Penna A, Saccenti A, De, Magistris F S, Scasserra S, Silvestri F, Simonelli A L, Simoni G, Tommasi P, Vannucchi G, and Verrucci L 2009 *Geotechnical aspects of the L'Aquila Earthquake*, *Earthquake Geotechnical Engineering Satellite Conference XVIIth International Conference on Soil Mechanics & Geotechnical Engineering, Alexandria, Egypt*

[4] Papanikolaou I D, Lekkas E L, Roberts G P, McGuire B, Fountoulis I G, Parcharidis I, and Foumelis M 2010 *The 2009 L'Aquila earthquake; findings and implications Event Science Report 02, AON Benfield UCL Hazard Research Centre*, *Event Science Report 02*, AON Benfield UCL Hazard Research Centre

[5] Coburn A and Spence R 2002 *Earthquake protection 2nd Edition*, John Wiley & Sons, Ltd., England 73

[6] Hutchings, L and Viegas G 2012 *Application of Empirical Green's Functions in earthquake source, wave propagation and strong ground motion studies*, *Earthquake Research and Analysis - New Frontiers in Seismology Sebastiano D'Amico (Ed)*

[7] Bizzarri A 2011 *On the deterministic description of earthquakes*, *Reviews of Geophysics* **49** 1

[8] Paolucci R, Infantino M, Mazzieri I, Özcebe A G, Smerzini C, and Stupazzini M 2017 *3D physics-based numerical simulations: advantages and current limitations of a new frontier to earthquake ground motion prediction The Istanbul case study*, *MOX Technical Report 68/2017*, Dipartimento di Matematica Politecnico di Milano, Via Bonardi 9 - 20133 Milano Italy

[9] McGuire R K 2001 *Deterministic vs probabilistic earthquake hazard and risks*, *Soil Dynamics & Earthquake Engineering* **21** 377
[10] Cornell C A 1968 *Engineering seismic risk analysis*, *Bulletin of the Seismological Society of America* **58** 1583
[11] McGuire R K 2007 *Probabilistic seismic hazard analysis: Early history*, *Earthquake Engineering and Structural Dynamics* **37** 329
[12] Anderson J G and Brune J N 1999 *Probabilistic seismic hazard analysis without the ergodic assumption*, *Seismological Research Letters* **70** 19
[13] Landwehr N, Kuehn N M, Scheffer T and Abrahamson N 2016 *A Non-Ergodic Ground-Motion Model for California with Spatially Varying Coefficients*, *Bulletin of the Seismological Society of America* **106** (6) 2574
[14] Bazurro P and Cornell A C 1999 *Disaggregation of seismic hazard*, *Bulletin of Seismological Society of America* **89** 501
[15] McGuire R K 1995 *Probabilistic seismic hazard analysis and design earthquakes: closing the loop*, *Bulletin of the Seismological Society of America* **85** 1275
[16] Kotha S R, Bindi D and Cotton F 2017 *Towards a non-ergodic probabilistic seismic hazard assessment In Europe and Middle East*, *16th World Conference on Earthquake, 16WCEE 2017: Santiago, Chile*
[17] Aki K. and Richards P G 2002 *Quantitative Seismology (2nd Edition)*, University Science Books, Sausalito, California, U.S.A.
[18] Hutchings L, Ioannidou E, Foxall W, Voulgaris N, Savy J, Kalogeras I, Scognamiglio L, and Stavrakakis G 2007 *A physically based strong ground-motion prediction methodology; application to PSHA and the 1999 Mw = 6.0 Athens earthquake*, *Geophysics Journal International* **168** 659
[19] Tarbali K, Bradley B, Huang J, Polak V, Lagrava D, Motha J, and Bae S 2018 *CYBERSHAKE NZ V179: New Zealand simulation-based probabilistic seismic hazard analysis*, *16th European Conference on Earthquake Thessaloniki Engineering*
[20] Tarbali K, Bradley B, Huang J, Lee R, Lagrava D, Bae S, Polack V, Motha J, and Zhu M 2019 *CYBERSHAKE NZ V185: New Zealand simulation-based probabilistic seismic hazard analysis*, *2019 Pacific Conference on Earthquake Engineering - New Zealand Society for Earthquake Engineering*
[21] Field E H, Jordan T H and Cornell C A 2003 *OpenSHA: a developing community modeling environment for seismic hazard analysis*, *Seism. Res. Lett.* **74** (4) 406
[22] Solomos G, Pinto A, and Dimova S 2008 *A Review of The Seismic Hazard Zonation in National Building Codes in the Context of Eurocode 8*, *European Commission, Varese Italy*, Joint Research Center JRC Technical Report
[23] Wald D J V, Quitoriano, Heaton T H, and Kanamori H 1999 *Relationships between peak ground acceleration, peak ground velocity and modified Mercalli intensity in California*, *Earthquake Spectra* **15** 557
[24] Valentini A, Pace B, Boncio P, Visini F, Pagliaroli A, and Pergalani F 2019 *Definition of seismic input from fault-based PSHA: Remarks after the 2016 Central Italy earthquake sequence*, *AGU 100: Advancing Earth and Space Science*
[25] Valentini A, Visini F, and Pace B 2017 *Integrating faults and past earthquakes into a probabilistic seismic hazard model for peninsular Italy*, *Natural Hazards and Earth System Sciences* **17** (11) 2017
[26] Molas G L, Yamazaki F, and Tomatsu Y 1994 *Seismic hazard analysis in the Philippines using earthquake recurrence data*, *Earthquake Engineering*, Tenth World Conference Balkema, Rotterdam 6031
[27] McGuire R K *Computations of seismic hazard*, *Annali di Geofisica* **36** 181
[28] Scordilis E M 2006 *Empirical global relations converting M_s and m_b to moment magnitude*, *Journal of Seismology* **10** 225

[29] Kanamori H 1977 *The energy release in great earthquakes*, *Journal of Geophysical Research* **82** 2981

[30] Hanks T C and Kanamori H 1979 *A moment magnitude scale*, *Journal of Geophysics Research* **84** 2348

[31] Causse M, Dalguer L A and Mai P M 2013 *Variability of dynamic source parameters inferred from kinematic models of past earthquakes*, *Geophysical Journal International* **196** (3) 607

[32] Shearer P 2009 *Introduction to Seismology 2nd ed*, *Cambridge University Press, New York*

[33] Virieux J 1984 *SH-wave propagation in heterogeneous media: Velocity-stress finite-difference method*, *Geophysics* **49** (11) 1933

[34] Schuster G T 2017 *Seismic Inversion*, Society of Exploration Geophysicists 166

[35] Evans L C 1997 *Partial Differential Equations. Graduate Studies in Mathematics Vol. 19*, American Mathematical Society

[36] Salsa S 2008 *Springer-Verlag, Italy, Milano*, Partial differential equations in action: From modelling to theory

[37] Zachmanoglou E C, and Thoe D W 1986 *Introduction to Partial Differential Equations with Applications*, *Dover Publications, Inc, New York*

[38] Li J and Chen Y T 2008 *Computational Partial Differential Equations Using MATLAB*, CRC Press, Taylor & Francis Group, Boca Raton

[39] Kanamori H and Brodsky E M 2004 *The physics of earthquakes*, *Rep. Prog. Phys* **67** 1429

[40] Mozco P, Kristek J, and Halada L 2004 *The finite-difference method for seismologists - An introduction*, *Comenius University, Bratislava*

[41] Pace B, Visini F, and Peruzza L 2016 *FiSH: MATLAB tools to turn fault data into seismic-hazard models*, *Seismological Research Letters* **872A** 374

[42] Wells D, and Coppersmith K 1994 *New empirical relationships among magnitude, rupture length, rupture width, rupture area and surface displacement*, *Bulletin of the Seismological Society of America* **90** 73

[43] Peruzza L and Pace B 2002 *Sensitivity analysis for seismic source characteristics to probabilistic seismic hazard assessment in central Apennines (Abruzzo area)*, *B. Geofis. Teor. Appl.* **11** 79

[44] Field E H, Jackson D D and Dolan J F 1999 *A mutually consistent seismic-hazard source model for southern California*, *Bulletin of Seismologocial Society of America* **89** 559

[45] Matthews M V, Ellesworth W L, and Reasenberg P A 2002 *A Brownian model for recurrent earthquakes*, *Bulletin of the Seismological Society of America* **92** (6) 2233

[46] Luzi L, Lanzano G, Felicetta C, D'Amico M C, Russo E, Sgobba S, Pacor, F and ORFEUS Working Group 5 2020 *Engineering Strong Motion Database (ESM) (Version 2.0)*, Istituto Nazionale di Geofisica e Vulcanologia (INGV)

[47] Paz M, and Leigh W 2004 *Structural dynamics: Theory and computation, 5th ed*, Kluwer Academic Publishers Group, Massachusetts

[48] Chopra A K 2001 *Dynamics of structures: Theory and applications to earthquake engineering*, Prentice Hall Inc., New Jersey

[49] Imbsen, R A 2007 *Proposed AASHTO guide specifications for LRFD seismic bridge design: Subcommittee for seismic effects on bridges*, Imbsen Consulting

[50] Ang A H-S and Tang W H 1975 *Probability Concepts in Engineering Planning and Design. Volume I, Basic Principles*, John Wiley & Sons, Inc., USA.

[51] Bhat H S, Dmowska R, King G C P, Klinger Y and Rice J R 2007 *Off-fault damage patterns due to supershear ruptures with application to the 2001 Mw 8.1 Kokoxili (Kunlun) Tibet earthquake*, *J. Geophys. Res.* **112**

[52] Bindi D, Pacor F, Luzi L, Puglia R, Massa M, Ameri G, and Paolucci R 2011 *Ground motion prediction equations derived from the Italian strong motion database*, *Bulletin of Earthquake Engineering* **9** (6) 1899

[53] Kreyzig E 2011 *Advanced Engineering Mathematics, 10th Edition*, John Willy & Sons, Inc. USA

[54] Ray M 2011 *L'Aquila Earthquake of 2009*, Retrieved from https://www.britannica.com/event/LAquila-earthquake-of-2009 on August 29, 2019